Ab Initio Molecular Dynamics Studies of Structural, Dynamical and Spectroscopic Aspects of Waterborne Selenium and Arsenic Species

by

Sangkha Borah

A thesis submitted
in Partial Fulfillment of the Requirements
for the Degree of

DOCTOR OF PHILOSOPHY.

Department of Physics
Indian Institute of Technology Guwahati
Guwahati 781039, India.

April 2018

Ab Initio Molecular Dynamics Studies of Structural, Dynamical and Spectroscopic Aspects of Waterborne Selenium and Arsenic Species

by

Sangkha Borah

Roll No. 136121015

A thesis submitted
in Partial Fulfillment of the Requirements
for the Degree of

DOCTOR OF PHILOSOPHY.

Supervisor

Prof. Padma Kumar Padmanabhan

Department of Physics
Indian Institute of Technology Guwahati
Guwahati 781039, India.

April 2018

CERTIFICATE

It is certified that the work contained in the thesis entitled "*Ab Initio Molecular Dynamics Studies of Structural, Dynamical and Spectroscopic Aspects of Waterborne Selenium and Arsenic Species*" by Mr. Sangkha Borah, a student of the Department of Physics, IIT Guwahati was carried out under my supervision and has not been submitted elsewhere for award of any degree.

Prof. Padma Kumar Padmanabhan,
Department of Physics, IIT Guwahati,
Guwahati-781039, Assam, India.
DATE: .....

ACKNOWLEDGMENTS

Firstly, I would like to express my sincere gratitude towards my Ph.D. advisor, Prof. Padma Kumar Padmanabhan for his consistent support, patience, motivation during my Ph.D. years. His deep understanding of the field has helped me understand the field better. His faith on me has always inspired me to work hard.

I would also like to thank my doctoral committee members, Dr. C. Y. Kadolkar, Prof. P. K. Giri, and Dr. M. Sarma, for their insightful comments and encouragement, and also for the thoughtful questions which stimulated me to concentrate more on the conceptual background.

My sincere thanks also goes to Prof. S. Ghosh, Prof. P. Poulose and Prof. S. Basu, the current and previous Heads of the Department of Physics for providing the facilities needed for my research, and all other faculty members of the department who supported me in several ways during my stay here. I would also like to thank the technical persons, stuff and office members, who provided me help whenever needed. Without their precious support it would not have been possible to conduct my research.

I would like to acknowledge the Center for Advanced Computing (CDAC) Pune and Param Ishan IIT Guwahati for generous allowance of CPU hours for carrying out the works presented in the thesis. I would also like to acknowledge the use of our departmental cluster facilities (DST grant nos. SR/FST/PSII-020/2009, SR/S1/PC-24/2011).

I thank my fellow lab-mates for the stimulating discussions and for all the fun we have had in the last five years.

I would like to thank wholeheartedly all my family members, my parents and my siblings for always supporting me. Their trust on me has always kept me moving on.

Last but not the least, I would like to thank my best friend, my wife, Bijita for always being there for me. Her support, encouragement, patience and unwavering love are my strengths.

ABSTRACT

Water contamination is a global issue in most parts of the world. The present thesis deals with the microscopic nature of interaction of two major water contaminants, namely selenium (Se) and arsenic (As), restricting largely to their relevant inorganic forms, owing to their higher solubility in water, employing *ab initio* molecular dynamics simulation. Various microscopic properties including molecular structure, hydrogen bonding, vibrational spectra, etc. are examined in detail. The thesis is organized as follows. A review of the state-of-the-art research activities on solvation studies of *ab initio* molecular dynamics, bio-geochemistry of selenium and arsenic species as well as the motivation for the present work is outlined in Chapter 1. Chapter 2 of the thesis summarizes the theoretical techniques employed in the work. Chapters 3 and 4 of the thesis present *ab initio* molecular dynamics studies on various inorganic Se–VI and Se–IV species in water. In chapters 5 and 6 inorganic As–III and As–V species are examined. Chapter 7 gives the conclusion of the thesis.

Table of Contents

CHAPTER 1

INTRODUCTION

Water contamination is one of the major threats to humanity especially in developing countries [1–4]. Water contaminants generally include both organic and inorganic compounds [5]. Organic contaminants include volatile chemicals, fuels, manure, pesticides, industrial solvents, etc. [6–8], while the major inorganic contaminants are barium, cadmium, copper, chromium, arsenic, antimony, fluoride, selenium, lead, etc [9–12]. Depending on the geography, the sources as well as severity of the contamination varies. In general, the surface as well as ground water contaminants, by and large can be traced to anthropogenic activities, such as agricultural run-off waters, drainage from industries, nuclear waste-disposal, etc., or to natural geochemical processes including volcanic activity, dissolution from mineral deposits, etc [8, 10, 13, 14]. Presently, researchers from various fields of expertise, such as chemists, biologists, environmentalists, geologists, etc., are actively pursuing research on various strategies for efficient water remediation processes. In the following the bio-geochemistry of two of the major water contaminants, namely selenium and arsenic, are briefly outlined.

1.1 Selenium

Selenium ($_{34}$Se, Period-4, Group-16) is an element in the oxygen family, lying between the non-metal sulfur (S) and metalloid tellurium (Te) in the modern periodic table. Therefore, it shows properties that are intermediate between these two elements, and

often like metalloid [15]. Selenium plays a *dual* role in human and animal lives; it is an essential micronutrient, but causes adverse health effects in mild excess [16]. It is one of the essential components of selenoproteins needed for various biological activities, such as in production of hormones and enzymes in the cells, fertility and reproduction, DNA synthesis, cells protection against oxidative damages, catalysis of intermediate metabolism, protein folding, etc [16–26]. Moreover, it is used in vitamins and mineral supplements, to prepare drugs and as a nutritional supplements for livestocks. In trace amounts selenium is reported to provide a protective role against the toxicity induced by heavy metals, such as mercury, arsenic, etc [24]. Selenium compounds are also useful in several industrial and commercial applications, such as in glass-making, in photocells and semiconductor devices, plastics, in anti-dandruff shampoos, photographic devices, gun bluing, etc. When exposure level is high and prolonged, it can be bio-accumulated inside the human body, mostly in the liver and kidneys, but also in the blood, lungs, heart, nails, hair, etc., depending on the type of the selenium species exposed to. This causes various symptoms, such as fatigue, irritability, hair loss, sloughing of nails, etc., and may lead to both acute and chronic health disorders such as gastrological disorders, neurological damage, lever cirrhosis, pulmonary edema, etc [17–22]. The

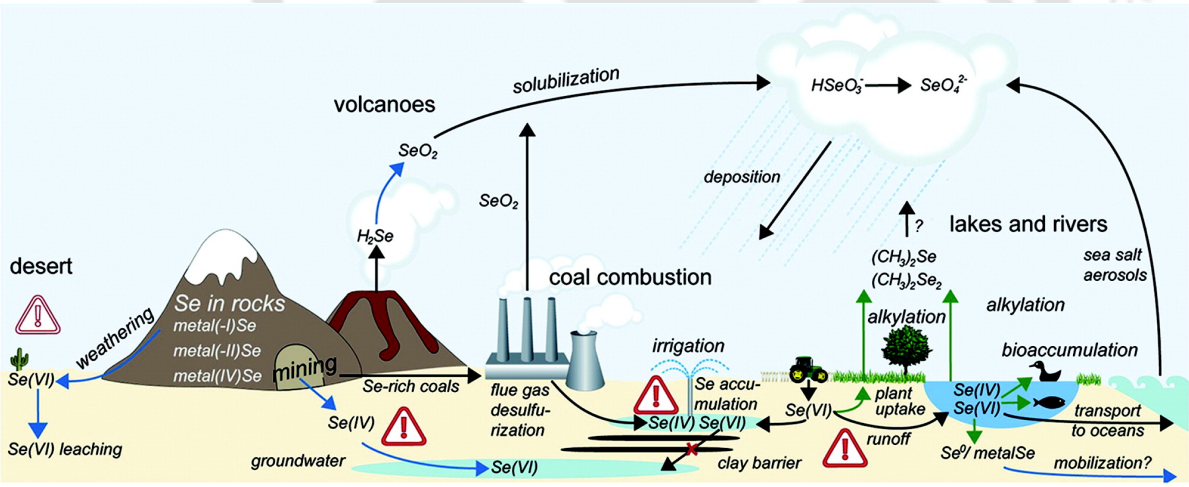

Figure 1.1: A basic bio-geochemical cycle of selenium. Reprinted with permission from [27], Copyright ©2011 American Chemical Society.

basic bio-geochemical cycle of selenium is shown in Fig (1.1). It occurs naturally in the Earth's crust, in rocks, sand, coal, limestone, etc. Selenium is rarely found in its elemental form (Se(0)) or as pure ore compounds. However, it occurs in quite handsome amounts along with sulfides and oxides of metals, such as copper, silver, nickel, lead,

etc. Selenium gets redistributed from these geological reservoirs into aquatic medium through various natural and anthropogenic processes [17, 28]. Natural processes include volcanic eruption, weathering processes, wildfire, dissolution from nuclear waste, etc., while typical anthropogenic activities involve mining, fossil fuel combustion, oil refining, agricultural irrigation, etc [28]. Combustion of fossil fuels releases selenium into the environment, mostly in the form of selenium dioxide (SeO_2). Further, refining of crude oils and irrigation activities of seleniferous soils lead to release of selenium in large amounts into the ecosystem.

Selenium has the electronic configuration of $[Ar]\,3d^{10}\,4s^2\,4p^4$ and hence typically exists in four oxidation states, viz., Se(VI), Se(IV), Se(0), and Se(−II). Of these the selenium oxyanions, selenate (SeO_4^{2-}) and selenite (SeO_3^{2-}), are particularly interesting in the present context, for their high solubility in water, and speciation under different pH conditions. The elemental selenium (Se(0)) and selenides (Se^{2-}) are sparingly soluble in water, and commonly occurs in the less oxidizing environments. Selenic acid, H_2SeO_4, the parent form of Se(VI) species in aqueous environment, is a strong acid with dissociation constants of $pK_{a1} = -3.0$ and $pK_{a2} = 1.70$ [29]. Selenous acid (or selenious acid), H_2SeO_3, the parent form of Se−IV species, is a much weaker acid compared to H_2SeO_4, with dissociation constants of $pK_{a1} = 2.62$ and $pK_{a2} = 8.32$ [29]. Selenite and selenate are normally stable in natural waters. However, these can be oxidized/reduced on mineral surfaces prompting their removal from water. They could also be removed from the water through reduction to Se(0) through chemical binding to organic matters. Characterization of the various selenium species present within waters is thus important for devising appropriate water treatment method.

1.2 Arsenic

Arsenic ($_{33}$As; Period-4, Group-15) is a metalloid that is quite ubiquitous on the Earth's crust. Compounds of arsenic has been traditionally used in various industrial, agriculture and medical purposes, such as in making alloys (e.g., lead alloys used in car batteries and ammunition), semiconductor and optoelectronic devices, production of pesticides, herbicides and insecticides, and in medicines. However, arsenic is notoriously poisonous to multicellular lives. Its adverse health effects on human includes neurological disorders, cardiovascular diseases and cancer. Arsenic contamination of ground and surface water is presently one of the major environmental concerns across the globe. The World Health

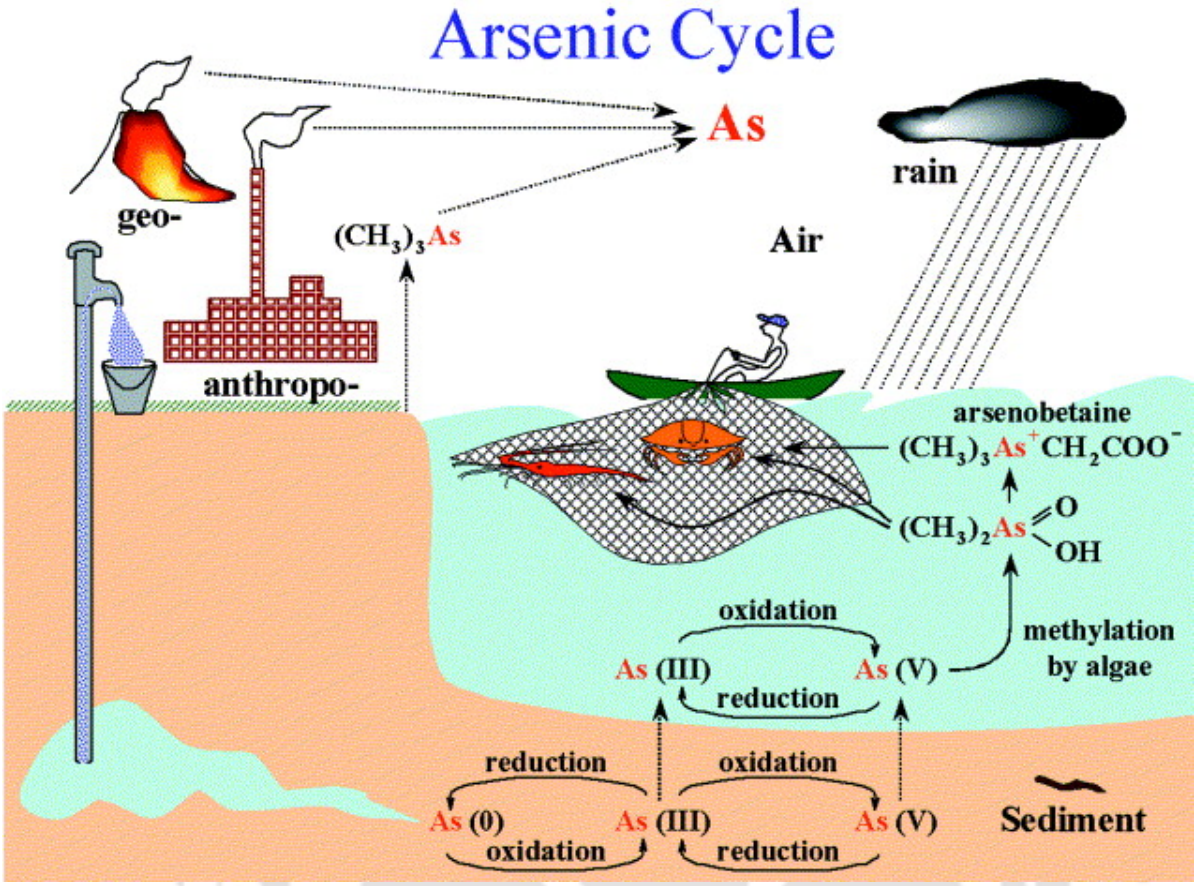

Figure 1.2: A basic bio-geochemical cycle of arsenic. Reprinted with permission from [30], Copyright: ©2002 Federation of European Microbiological Societies. Published by Elsevier B.V. All rights reserved.

Organization (WHO) and the U.S. Environmental Protection Agency (USEPA) have classified arsenic as a carcinogen of category I.

The global bio-geochemical cycle of arsenic is shown schematically in Fig. 1.2. Arsenic has the electronic configuration of $[\mathrm{Ar}]\,3\mathrm{d}^{10}\,4\mathrm{s}^2\,4\mathrm{p}^3$, and thus, mostly exists in the valence states of III and V. It occurs on the Earth's crust, most commonly, as oxides and sulfides (e.g., As_4S_4, As_2O_3, etc.) or combined with other metals, such as iron (e.g., FeAsS). However, occasionally it is also found in the elemental form (As(0)) in some rocks. Arsenic is often found in mining of gold (Au) and coals. It is also found during volcanic eruptions combined with other elements. Various agricultural activities using arsenic containing pesticides, herbicides, insecticides, wood preservative, etc. also contribute to the release of arsenic into the environment. Various microbial activities and methylation processes contribute to volatilization of arsenic. Natural weathering processes, irrigation

activities, etc. leads to redistribution of arsenic from soil and air to natural waters.

In aquatic conditions, arsenic is generally present in two oxidation states – As (V) (arsenate, H_3AsO_4), and As (III) (arsenite, H_3AsO_3). In aerobic conditions, the former is dominant; so is the case with water at the surface of lakes and rivers. In anaerobic conditions, such as in groundwaters and at the bottom of very deep lakes, As (III) is found to be the dominant species due to reduction from As (V) to As(III). Organic arsenic species, such as mono-methylarsonic acid (MMA), di-methylarsinic acid (DMA), are sparingly soluble in water and are also much less toxic compared to its inorganic forms, such as arsenites and arsenates. There are other non-toxic arsenic forms as well, such as arsenobetaine ($C_5H_{11}AsO_2$), arsenocholine ($C_5H_{14}AsO^+$), arsenosugars, etc., that are typically found in marine environment. Additionally, the presence of some uncharacterized arsenic species is reported in certain aquifers [31].

1.3 Water

Accounting for about 70% of the surface of Earth and about 65% of human and animal body, water is the most ubiquitous liquid on the planet, while also holds the distinction as the “universal solvent”. Water in its pure form as well as dissolving other species, are of great importance to numerous physico-chemical, geochemical and biological processes of nature. Undoubtedly, water is the most interesting liquid on our planet, not only because of its relevance but also due to the fact that it exhibits many unique and extraordinary physical as well as chemical properties.

Water (H_2O) is a tiny molecule with two hydrogen atoms covalently bonded to the central oxygen atom. The electron clouds of the two lone pairs of the oxygen atom spread out almost tetrahedrally giving water a bent structure. Owing to the large positive charge on the nucleus (8+), the H atoms are attracted strongly by the electronegative O atom of H_2O giving them partial positive charges, while acquiring partial negative charge on itself. This prompts the negative ‘O’ atoms to interact appreciably with the positive ‘H’ atoms of other molecules resulting in the formation of Hydrogen bonds (H-bonds) both with themselves as well as with other solvents (see Fig. 1.3). Due to the bent structure of water molecule, the negative and positive charge centers do not coincide with each other giving water a net dipole moment. In gas phases, water molecule has a dipole moment of ≈ 1.86 D [32] and ≈ 3 D in the liquid phases [33].

Water exists in three different phases- solid (ice), liquid (water) and gas (vapor). In

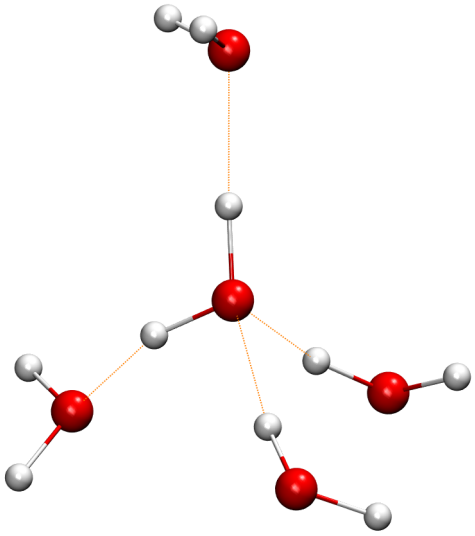

Figure 1.3: The H-bonds network formed by a water molecule. Generated from CPMD simulation of waters at 315 K.

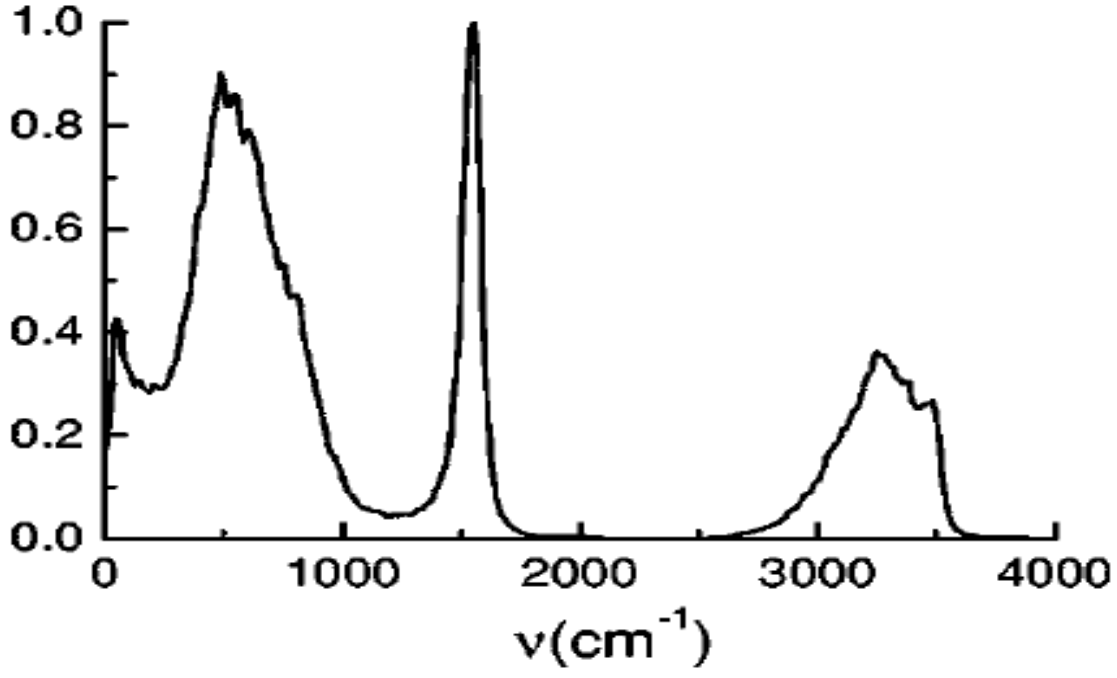

Figure 1.4: A typical water spectrum calculated from Fourier transform of the velocity autocorrelation function. Reprinted with permission from [34]. Copyright ©2001 American Institute of Physics.

ice form, each water molecule is involved in forming 4 tetrahedrally oriented H-bonds (H – O – H angle is ≈ 109.5°), which get changed in gaseous and liquid phases. Accurate *ab initio* calculations gives the mean O – H bond length 0.958 Å and H – O – H angle 104.49° [35] gas phases, against the experimental values of 0.957 Å and 104.47° respectively [36]. In liquid phases, these values are considerably changed with *ab initio* calculations predicting an O – H bond length of ~ 0.98 Å and H – O – H angle of 105.5° [33] with close agreements to experimental results [37–39]. In liquid phase, water forms H-bonds which weakens the strengths of the covalent bonds and reduces the repulsion between the electron orbitals. Classical models [40] employ O – H lengths of between 0.957 – 1.00 Å and H – O – H angles between 104.52 – 109.5°.

Water has a complex absorption spectrum[41–43]. In gas phase, the modes of vibration involve combination of symmetric stretching (ν_1), asymmetric stretching (ν_2) and bending (ν_3) of the covalent bonds with absorption intensity $I_{\nu_1} : I_{\nu_2} : I_{\nu_3}$ = 0.07 : 1.47 : 1.00 [43–45], in addition to the three modes of libration- wagging, twisting and rocking, which are nothing but rigid body rotations of the water molecule about the x, y and z axes. The bending and stretching modes are respectively found at about 1595, 3657 and 3756 cm^{-1} in gas phases. Vibrational modes in liquid states are however more complex, the stretching modes are red-shifted by about 250 cm^{-1} as compared to gas phase values. A typical water spectra in liquid form is shown in Fig 1.4. Here, the peak around 2500 – 3600 cm^{-1} is due to O – H stretching modes of vibration. The peak at about 1500 cm^{-1} is assigned to the H – O – H bending mode. On the other hand, the modes in the range of about 0 – 1000 cm^{-1} can be assigned to the librational motions of water molecules. In liquid state, rotations of the individual water molecule tend to be restricted by the H-bonds giving the librations with broder peaks.

1.4 Solvation Phenomena

Solvation is a kinetic process that involves continuous reorganization of the solvent as well as the solute molecules in order to minimize the free energy. The interactions between the solvent and solute molecules can be of different types such as hydrogen bonding, ion-ion, ion-dipole interaction, or van der Waals forces (induced dipoles). The type of interaction determines the behavior of the solute in the solvent environment, which, in turn, determines various physical, structural, dynamical and spectroscopic properties of it, and also influence the properties of the solvents. Solvation is important

for various physical, chemical, geological processes, and also for biological activities that occur within the cell. For example, protein folding occurs because of the favorable interactions with its surrounding water molecules and hydrogen bonding effects. In addition to these, solvation affects the electronic as well as vibrational properties, diffusivity and reactivity of molecules.

It has been known since long that water molecules form inter-molecular H-bonds. These are believed to be responsible for many of the remarkable properties of water, such as its high boiling point, high surface tension, anomalous density variation with temperature, etc [46]. They also form H-bonds with other solvated solute molecules. The shell of water molecules interacting directly to the solute forming H-bonds is known as first hydration shell. Those water molecules that interact directly to the first hydrogen shell are referred to form the second hydration shell, and so on. Often, depending on the nature of the solute a few hydration shells, distinguishable from the structure of the bulk water, are realizable. If the solute-water interactions are stronger than those between the water molecules, the solute is referred to as H-bond maker, and if weaker then referred to as H-bond breaker. It shall also be noted that the hydrogen bond network is highly dynamic, with H-bonds being continuously broken and formed.

For long the study of solvation phenomena, that involves various manifestations of the solute-solvent interactions, such as the modification of the structure of the solvent, the dynamics of the solute as well as that of the solvent, etc., have been a very active area of research owing to their importance in chemical, geological, physical and biological processes. The natural H-bond network of liquid water is locally disrupted by the introduction of a foreign species, such as an ion or other molecules. Although, this is energetically unfavorable, the loss is often compensated by the formation of solute-solvent H-bonds, thus resulting in a negative total free energy of solvation. The solute-water interaction depends on the strength as well as the number of the H-bonds formed upon solvation, which in turn, depends on various aspects such as the charge, size and shape of the solute.

It is perceptible that higher the charge of the solute the stronger is the H-bonds between the solute and water. However, the effect of the size and molecular structure of the solute on the strength and number of H-bonds formed is not straightforward. A larger solute disrupts the local water network to a larger extent, weakening the H-bonds of bulk waters (unfavorable), and results in a larger solvation shell. However, if it has more polar sites somewhat evenly distributed across its structure, then larger number of

solute-water H-bonds would be formed which would make up for the disrupted water-water H-bonds, thus resulting in a favorable situation. Thus, the net effect is highly dependent on the type of the solvated ion and its geometry.

Probing microscopic properties of species in aqueous phases through laboratory experiments is often challenging. In this context, computational approaches, such as molecular dynamics (MD) are very promising. MD simulations, particularly the *ab initio* MD (discussed in detail in the next chapter) which employs *on-the-fly* calculation of atomic interactions, have contributed significantly to our understanding of the solvation phenomena. Below a concise review on the state of the art *ab initio* molecular dynamics (AIMD) studies of water, in pure form as well as dissolving variety of foreign species is presented. [47–56]

1.5 AIMD studies of Solvation

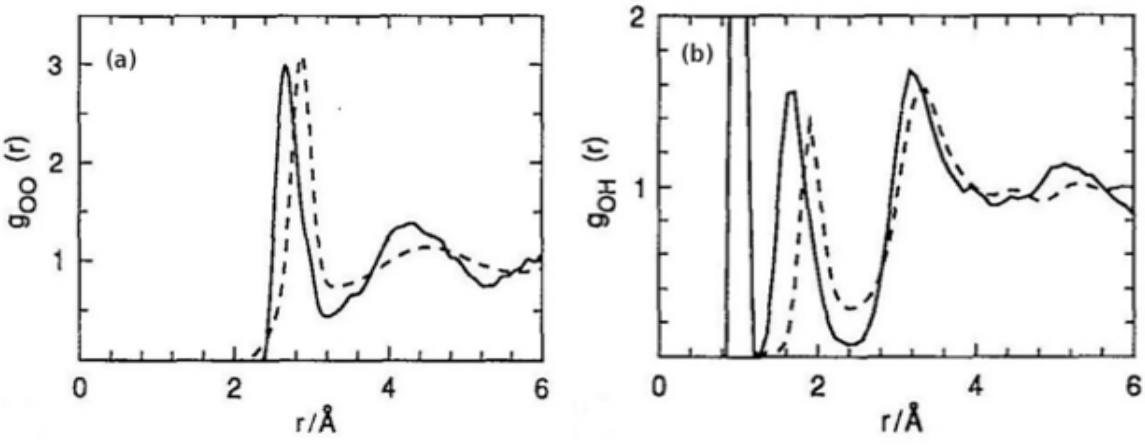

Figure 1.5: Radial distribution function, RDF for (a) O−O and (b) O−H atom pairs in liquid water, computed from CPMD simulation of 32 D_2O molecules for 1.5 ps at room temperature, employing Becke-Perdew generalized gradient corrected functional Vanderbilt ultrasoft pseudo-potentials (solid lines), as compared to those obtained from experiments (dotted lines). (Reprinted with permission from [57]. Copyright ©1993, American Institute of Physics.)

Numerous studies have been published over the last few decades that have provided unprecedented insights into the microscopic aspects of the solvation, such as the characterization of various structural, dynamical and spectroscopic properties, particularly related to that of H-bonding, proton transport etc. Although long strides have been made, it shall be noted that the most accurate description of liquid water in a cost effective way,

is still not achieved, and consequently, lots of developmental works, both theoretical and algorithmic, are going on. One of the earliest AIMD studies, conducted by Laasonen and co-workers [57] on liquid water has shown the radial distribution functions (RDF, $g(r)$) in modest agreement with experimental results (see Fig. 1.5).

Spontaneous ionization of liquid water leading to the proton (H_3O^+) and hydroxide (OH^-) ion and their dynamics are fundamental aspects of solution phase chemistry. Their presence in water induces a perturbation in the structure of the surrounding waters, and also various dynamical properties such as the H-bond dynamics, structural and orientational relaxation, etc. The first AIMD simulations of the excess proton in water were conducted by Tuckerman et al [58, 59] on a system comprising of 32 water molecules. They showed that a hydronium ion (H_3O^+) exists in two limiting states of a H-bond network - (a) the Zundel ($H_5O_2{}^+$) state and, (b) the Eigen ($H_9O_4{}^+$) state. Both of these cations are present in water, with the latter being the dominant state in liquid water. The Zundel cation is the intermediate state that gets formed as the proton is about to transfer from one water molecule to the next. The more stable $H_9O_4{}^+$-state consists of a H_3O^+-ion that donates three H-bonds to three surrounding water molecules, the excess proton being localized on the central water molecule. In a $H_5O_2{}^+$-state, on the other hand, the excess proton is localized between the two water molecules. Fig. 1.6 shows the important steps in a successful proton transfer. In this process, a water molecule (Fig. 1.6(a)) donates a weak H-bond to the H_3O^+ ion. In the second step, this water molecule loses the other H-bonds donated to it, and the weak H-bond donated to the current hydronium becomes strong, which destabilizes its ability to host the proton (Fig. 1.6(b)). Meanwhile the $O-O$ distance between the current and future hydroniums decreases by ~ 0.15 Å and transfer of the proton takes place in the next step (Fig. 1.6(c)). This mechanism of proton transfer is known as the Grotthuss mechanism [60], qualitative picture introduced by Grotthuss about 200 years before that study [61]. While pure AIMD simulations indicated that the barrier for proton transfer is approximately 0.5 kcal/mol, inclusion of nuclear quantum effects makes the process essentially barrier-less, although the mechanism of proton transfer remains the same [63].

Historically, it was thought that the transport mechanism of hydroxide (OH^-) ion could be inferred from that of hydronium (H_3O^+) ion by the so called “mirror image" concept, where it was suggested that the proton hole (OH^-) moves by successive shifts of hydrogen atoms, similar to protons [61]. But it was found from experiments [64] that the diffusivity/conductivity of OH^- is much slower than H_3O^+ which could not be explained

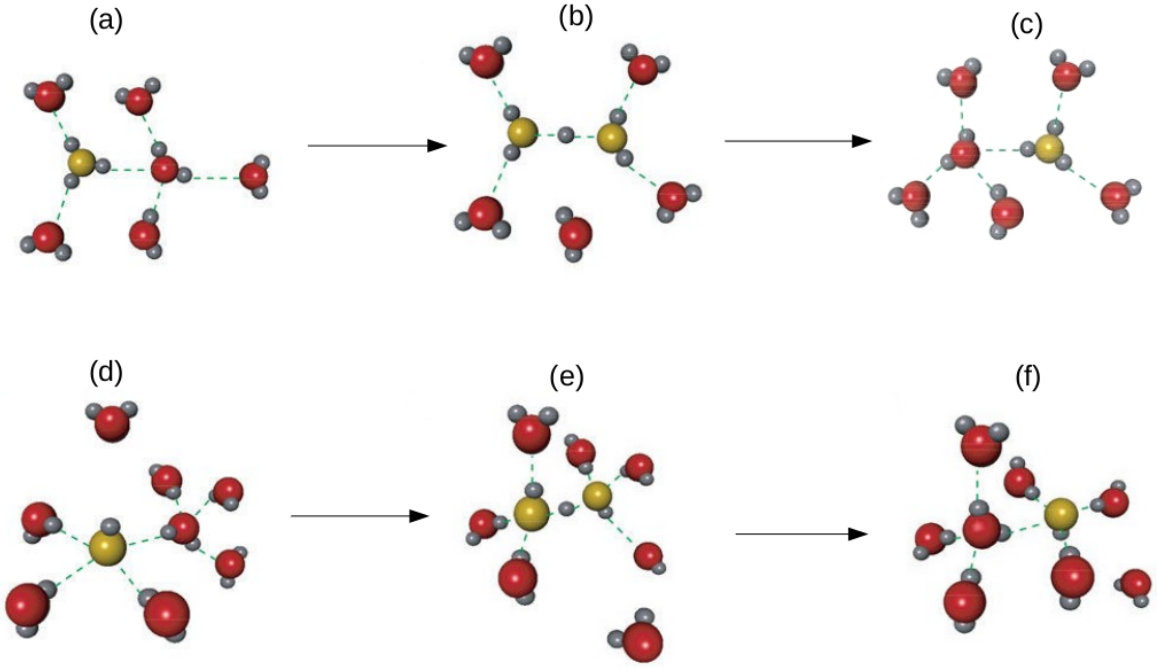

Figure 1.6: The main steps in a successful proton ($a-c$) and hydroxide ion ($d-f$) transfer. The mechanistic details are described in the text. Reprinted with permission from [62]. Copyright ©2002 Nature Publishing Group.

by the above mechanism. AIMD simulations have provided the right answer for that, thereby disclosing the dissimilarities in conductivity of the two ions [51].

AIMD simulation studies carried out by Tuckerman et al. [58, 59] on OH^- have showed that OH^- in water accepts four strong H-bonds, forming nearly a square planar arrangement of $H_9O_5^-$ (see Fig. 1.6(d)). It is also found to donate a weaker H-bond, thus highly perturbing the surrounding waters, which are H-bonded with tetrahedrally coordinated water molecules (see Fig. 1.3). They have confirmed it by the calculation of density of states (DOS) for OH^-, that shows some new features as compared to water [59]. These are attributed to the presence of $H_9O_5^-$ (Fig. 1.6(d)) and $H_7O_4^-$ (Fig. 1.6(e)), the latter being the intermediate formed during the transfer of OH^-, shown in Fig. 1.6. Recent electron spectroscopy experiments have confirmed these structures of OH^- anion [65]. During a successful OH^- transfer event (see Fig. (1.6(d - f)), one of the H-bonds accepted by OH^- in $H_9O_5^-$ complex breaks, leaving the OH^- ion accepting three H-bonds in a tetrahedral arrangement of $H_7O_4^-$ complex. The H-bond donated by it becomes stronger, and a transient Zundel anion ($H_3O_2^-$) is formed through which the migration of OH^- defect takes place. Subsequently, the new OH^- reforms $H_9O_5^-$ species

that are relatively stable and immobile. While pure AIMD simulations indicated that the barrier for OH^- transfer is approximately 1.28 kcal/mol, inclusion of nuclear quantum effects reduces it to approximately 0.34 kcal/mol, although the mechanism of transfer remains the same [62, 63].

The success of AIMD to the studies of water and its constituent ions has motivated the researchers to apply these techniques to get insights into the complex phenomena of solvation of various inorganic, organic and biological species in aqueous environment. For example, it has been applied to various mono-atomic alkaline [34, 66–73], earth alkaline [26, 74, 74–83] and halide ions [71–73, 82, 84–88], organic and organo-metallic systems, ions at interfaces, and even some selected biological systems [89]. The halogen ions,

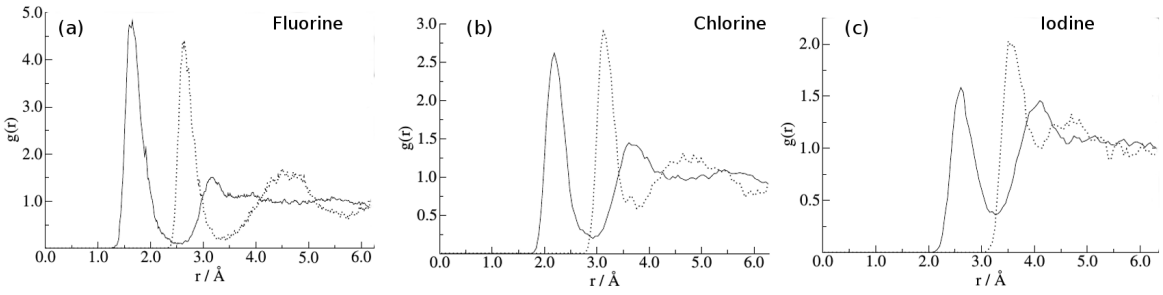

Figure 1.7: Oxygen (solid lines) and Hydrogen (dotted lines) RDFs w.r.t. F^- (a), Cl^- (b) and I^- (c) computed from CPMD simulations. Reprinted with permission from [90–92]. Copyright ©2003 American Institute of Physics.

F^-, Cl^-, Br^- and I^- have been studied in order to extract the systematic behaviors of different physical and chemical properties (such as the relative strength of the H-bonds, ionic radii, etc), as these ions have similar charges and valence electron configurations, but vary in masses and sizes [71]. Most often these are categorized as structure maker or structure breaker species in water, based on the overall influence that the ions have on the bulk waters. Heuft and Meijer [90–92] have systematically studied the solvation F^-, Cl^- and I^- and compared different structural, dynamical and spectroscopic aspects of these ions and the solvent waters. Their results showed that the interaction of I^- with water is much weaker than those of F^- and Cl^-, resulting a weaker hydration shell. Their works on HCl showed the effect on concentration on structural and dynamical properties.[93, 94] Parrinello et. al [95] have also explored the microscopic structure of as well as different static and dynamic properties of HF solvation in water at different thermodynamic conditions.

Similar to the halogens, group-I ions, such as Li^+ [34, 66, 67], Na^+ [66, 68, 96, 97], K^+ [66, 96] etc. have been extensively studied. Such systems are still being explored by different research groups by employing relatively improved methodologies [98–100]. One of the earliest studies by Lyubartsev et. al. [34] on Li^+ in water has shown remarkable resemblance of AIMD data with available neutron scattering and spectroscopic data. They also investigated the spectral features water dissolving Li^+ that showed reasonable agreement with results of IR and Raman experiments 1.4. Ramaniah et al. [69] showed from AIMD simulations that unlike the cases of Li^+, Na^+, Be^{2+} [34, 66, 66–68, 76, 96, 97] etc., which have well-defined structures, the first solvation shell of K^+ is very flexible and exhibits faster exchanges of water molecules with the second shell.

Certain other cations of greater environmental or biological importance, such as Mg^{2+}[78, 79], Be^{2+}[76], Ca^{2+}[74, 75, 78, 101–103], Fe^{2+}[104, 105], Fe^{3+}[104–106], Cu^{2+}[107] etc., have also been investigated extensively. Such studies not only provided the microscopic insights into their dynamic solvation structures, but also proved to be helpful in resolving many experimental discrepancies. For example, various experimental studies employing X-ray diffraction measurements suggested that the coordination number of Ca^{2+} varied between $6-8$, while, in contrast, neutron diffraction studies found it to be in the range of $6-10$. Lightstone et al.[75], from AIMD simulations, showed that the first solvation shell of Ca^{2+} is rather flexible unlike other divalent cations allowing the coordination number to vary from $6-8$. Ikeda et al.[77] characterized the structural variations of the first coordination shells of Ca^{2+} and Mg^{2+} by employing the metal-water oxygen coordination number as a reaction coordinate. In particular, they estimated the free-energy profile for Mg^{2+} and Ca^{2+}. The study revealed that the global minimum for the former is stable with a sixfold coordination in the octahedral arrangement; while the latter showed several shallow local minima, suggesting that the hydration structure of Ca^{2+} is highly variable, in agreement with experiments [75]. Similarly, Pasquarello et al. [108], from a combined study involving neutron diffraction experiments and AIMD simulations, demonstrated the five-fold coordination nature of the Cu^{2+} ions in water. This study have challenged the commonly held view of the classical sixfold coordination structure generally assumed for such metallic elements. Swaddle et al. [109] obtained similar results for trivalent aluminium ions (Al^{3+}) as well.

By virtue of the rapid growth in computational resources as well as developments of highly scalable algorithms and theoretical approaches, the AIMD methodologies have now being further applied to more chemically complex species in water. Different

metal oxide complexes have also been explored recently [110–112]. The properties of such systems depend strongly on pH of the solution [113]. Techniques for efficient computation of NMR parameters from *ab initio* methodologies have been developed that are able to provide direct comparison of theory with experiments, and have been widely applied for many systems of interest [111, 114–116]. The work of Bühr et. al. showed that the isotope effect and temperature dependence in NMR spectra for ^{59}Fe complexes [111, 116].

There also have been a number of applications devoted to the structural characterization of organic molecules in water. For example, AIMD studies have been performed on CO_2 [117–120], H_2CO_3 [117, 121], $CaCO_3$ [122, 123] and different hydrocarbons [124–127]. AIMD has also been applied to supercritical CO_2 [120, 128], and different ionic liquids [129]. *Ab initio* metadynamics (an enhanced sampling method) has been applied to explore different reaction mechanisms taking place in solutions [130–132]. Such techniques have also been employed for determining pK_a values for acids [133–136].

Besides these, studies involving aqueous systems near interfaces have attracted a lot of attention, being a topic of fundamental interest for biochemistry, engineering, geology and other areas [55, 137]. There have been several AIMD studies dedicated to air-water interfaces, being one of the most hydrophobic interfaces, characterized by water molecules with dangling bonds [138–141]. Thus, the small cations are expected to be repelled from the surface. However, various experimental as well as simulation studies have shown that hydronium (H_3O^+) cations are instead preferentially adsorbed at the air-water interfaces, thereby making the surface of water acidic [142–144]. On the other hand, hydroxyl ions have been found to have lower affinity to the interface [144]. Such studies have also been applied for applications involving the simulation of water and ions near inorganic solid surfaces, such as that of rutile, geothite, alumina, silica, etc [55, 145, 146].

Moreover, hybrid QMMM methods, combining quantum mechanical (QM) and classical molecular mechanics (MM) simulation techniques have been developed. In these methods, the reactive sites are treated quantum mechanically employing *ab initio* simulation methods, while the surrounding solvent environments are simulated employing classical MD, thus utilizes the best of the two techniques [147–153]. These techniques have been widely applied for metal-based enzymes, ligand-target interactions, charge-transfer processes in DNA, and other similar problems, see the article [154] and references therein.

1.6 Focus of the thesis

The inorganic forms of selenium and arsenic are, in general more soluble in water, thus accounts for the major water contaminants. These are also, in general, more toxic than their organic compounds. Fig. 1.8 shows the non-deprotonated forms of Se–VI, Se–IV, As–V and As–III species using ball and stick model.

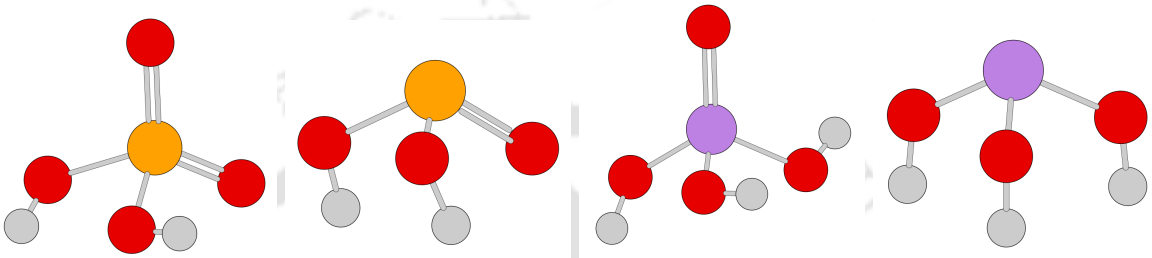

(a) H_2SeO_4 (b) H_2SeO_3 (c) H_3AsO_4 (d) H_3AsO_3

Figure 1.8: The ball-stick representation of the non-deprotonated forms of (a) Se–VI species (selenic acid), (b) Se–IV species (selenous acid), (c) As–V species (arsenic acid), and (d) As–III species (arsenous acid).

The focus of thesis is to investigate the microscopic dynamics of these waterborne species employing AIMD simulations. Chapter III and IV of the thesis present *ab initio* molecular dynamics studies on various inorganic Se–VI and Se–IV species in water, in chapters five and six inorganic As–III and As–V species are examined. Various microscopic properties including molecular structure, H-bonding, vibrational spectra, etc. are examined in detail. Chapter II provides a discussion of the methodology employed in these studies.

BIBLIOGRAPHY

[1] Jim Wright, Stephen Gundry, and Ronan Conroy. Household drinking water in developing countries: a systematic review of microbiological contamination between source and point-of-use. *Trop. Med. Int. Health*, 9(1):106–117, 2004.

[2] Warren Viessman, Mark J Hammer, Elizabeth M Perez, and Paul A Chadik. *Water supply and pollution control*. Pearson Prentice Hall New Jersey, 2009.

[3] Philip B Bedient, Hanadi S Rifai, Charles J Newell, et al. *Ground water contamination: transport and remediation*. Prentice-Hall International, Inc., 1994.

[4] Lorna Fewtrell and Jamie Bartram. *Water Quality: Guidelines, Standards & Health*. IWA publishing, 2001.

[5] Pradyot Patnaik. *Handbook of Inorganic Chemicals*. McGraw-Hill, 1st edition, 2002.

[6] DJ Lapworth, Nicole Baran, ME Stuart, and RS Ward. Emerging organic contaminants in groundwater: a review of sources, fate and occurrence. *Environ. Pollut.*, 163:287–303, 2012.

[7] CE Hamilton. Organic contaminants of water. *ASTM Stand News*, 4:34–35, 1976.

[8] John-Karl Böhlke. Groundwater recharge and agricultural contamination. *Hydrogeol J.*, 10(1):153–179, 2002.

[9] M A Hashim, Soumyadeep Mukhopadhyay, Jaya Narayan Sahu, and Bhaskar Sengupta. Remediation technologies for heavy metal contaminated groundwater. *J. Environ. Manage.*, 92(10):2355–2388, 2011.

[10] J Nouri, AH Mahvi, GR Jahed, and AA Babaei. Regional distribution pattern of groundwater heavy metals resulting from agricultural activities. *Environ. Geol.*, 55(6):1337–1343, 2008.

[11] MA Momodu, CA Anyakora, et al. Heavy metal contamination of groundwater: the surulere case study. *Res. J. Environ. Earth Sci.*, 2(1):39–43, 2010.

[12] Lars Järup. Hazards of heavy metal contamination. *Br. Med. Bull.*, 68(1):167–182, 2003.

[13] WF Ritter. Pesticide contamination of ground water in the united states-a review. *J. Environ. Sci. Health. Part B*, 25(1):1–29, 1990.

[14] George William Page. Comparison of groundwater and surface water for patterns and levels of contamination by toxic substances. *Environ. Sci. Technol.;(United States)*, 15(12), 1981.

[15] René E. Vernon. Which elements are metalloids? *J. Chem. Educ.*, 90(12):1703–1707, 2013.

[16] Suguru Kurokawa and Marla J Berry. Selenium. Role of the essential metalloid in health. *Met. Ions Life Sci.*, 13:499–534, 2013.

[17] Peter M Chapman, William J Adams, Marjorie Brooks, Charles G Delos, Samuel N Luoma, William A Maher, Harry M Ohlendorf, Theresa S Presser, and Patrick Shaw. *Ecological assessment of selenium*

in the aquatic environment. CRC Press, 2010.

[18] A Dennis Lemly and Gregory James Smith. Aquatic cycling of selenium: implications for fish and wildlife. Technical report, National Fisheries Contaminant Research Center, Columbia, MO (USA), 1988.

[19] Youcef Mehdi, Jean-Luc Hornick, Louis Istasse, and Isabelle Dufrasne. Selenium in the environment, metabolism and involvement in body functions. *Molecules*, 18(3):3292–3311, 2013.

[20] Marco Roman, Petru Jitaru, and Carlo Barbante. Selenium biochemistry and its role for human health. *Metallomics*, 6(1):25–54, 2014.

[21] Charles G Wilber. Toxicology of selenium: a review. *Clin. Toxicol.*, 17(2):171–230, 1980.

[22] Kurt J Maier, Christopher G Foe, and Allen W Knight. Comparative toxicity of selenate, selenite, seleno-dl-methionine and seleno-dl-cystine to daphnia magna. *Environ. Toxicol. Chem.*, 12(4):755–763, 1993.

[23] Fiona M Fordyce. Selenium deficiency and toxicity in the environment. In *Essentials of medical geology*, pages 375–416. Springer, 2013.

[24] Emilien Pelletier. Mercury-selenium interactions in aquatic organisms: a review. *Mar. Environ. Res.*, 18(2):111–132, 1986.

[25] Steven J Hamilton. Review of selenium toxicity in the aquatic food chain. *Sci. Total Environ.*, 326(1):1–31, 2004.

[26] Mor M Naor, Keith Van Nostrand, and Christoph Dellago. Car–parrinello molecular dynamics simulation of the calcium ion in liquid water. *Chem. Phys. Lett.*, 369(1):159–164, 2003.

[27] LHE Winkel, CA Johnson, M Lenz, T Grundl, OX Leupin, M Amini, and L Charlet. Environmental selenium research: From microscopic processes to global understanding. *Environ. Sci. Technol.*, 46(2):571–579, 2012.

[28] CH2M HILL. *Review of available technologies for the removal of selenium from water*. 2010.

[29] Lars Eklund. Hydration of oxo anions. Master's thesis, Department of Chemistry and Biotechnology, Uppsala, 2014.

[30] Rita Mukhopadhyay, Barry P Rosen, Le T Phung, and Simon Silver. Microbial arsenic: from geocycles to genes and enzymes. *FEMS Microbiol. Rev.*, 26(3):311–325, 2002.

[31] C Watt, XC Le, Y Cai, OC Braids, et al. *Arsenic speciation in natural waters*. American Chemical Society, 2002.

[32] Shepard A Clough, Yardley Beers, Gerald P Klein, and Laurence S Rothman. Dipole moment of water from stark measurements of h2o, hdo, and d2o. *J. Chem. Phys.*, 59(5):2254–2259, 1973.

[33] Pier Luigi Silvestrelli and Michele Parrinello. Structural, electronic, and bonding properties of liquid water from first principles. *J. Chem. Phys.*, 111(8):3572–3580, 1999.

[34] AP Lyubartsev, Kari Laasonen, and A Laaksonen. Hydration of li+ ion. an ab initio molecular dynamics simulation. *J. Chem. Phys.*, 114(7):3120–3126, 2001.

[35] Attila G Császár, Gábor Czakó, Tibor Furtenbacher, Jonathan Tennyson, Viktor Szalay, Sergei V Shirin, Nikolai F Zobov, and Oleg L Polyansky. On equilibrium structures of the water molecule. *J. Chem. Phys*, 122(21):214305, 2005.

[36] JB Hasted. Liquid water: Dielectric properties. In *The Physics and Physical Chemistry of Water*,

pages 255–309. Springer, 1972.

[37] AK Soper and CJ Benmore. Quantum differences between heavy and light water. *Phys. Rev. Lett.*, 101(6):065502, 2008.

[38] Kaoru Kashimoto, Jaesung Yoon, Binyang Hou, Chiu-hao Chen, Binhua Lin, Makoto Aratono, Takanori Takiue, and Mark L Schlossman. Structure and depletion at fluorocarbon and hydrocarbon/water liquid/liquid interfaces. *Phys. Rev. Lett.*, 101(7):076102, 2008.

[39] K Ichikawa, Y Kameda, T Yamaguchi, H Wakita, and M Misawa. Neutron-diffraction investigation of the intramolecular structure of a water molecule in the liquid phase at high temperatures. *Mol. Phys.*, 73(1):79–86, 1991.

[40] Anders Wallqvist and Raymond D Mountain. Molecular models of water: Derivation and description. *Rev. Comput. Chem.*, 13:183–247, 2007.

[41] Philip W Rosenkranz. Water vapor microwave continuum absorption: A comparison of measurements and models. *Radio Sci.*, 33(4):919–928, 1998.

[42] JK Messer, Frank C De Lucia, and Paul Helminger. The pure rotational spectrum of water vapor—a millimeter, submillimeter, and far infrared analysis. *J. Infrared Millim. Terahertz*, 4(4):505–539, 1983.

[43] Jonathan Tennyson, Peter F Bernath, Linda R Brown, Alain Campargue, Michel R Carleer, Attila G Császár, Robert R Gamache, Joseph T Hodges, Alain Jenouvrier, Olga V Naumenko, et al. Iupac critical evaluation of the rotational–vibrational spectra of water vapor. part i—energy levels and transition wavenumbers for h217o and h218o. *J. Quant. Spectrosc. Radiat. Transfer*, 110(9-10):573–596, 2009.

[44] David Eisenberg, David S Eisenberg, and Walter Kauzmann. *The structure and properties of water*. Oxford University Press, 2005.

[45] Linus Pauling. The structure of water. In *Hydrogen Bonding*, pages 1–6. Elsevier, 1959.

[46] GE Walrafen, MR Fisher, MS Hokmabadi, and W-H Yang. Temperature dependence of the low-and high-frequency raman scattering from liquid water. *The Journal of chemical physics*, 85(12):6970–6982, 1986.

[47] Ali A Hassanali, Jérôme Cuny, Vincenzo Verdolino, and Michele Parrinello. Aqueous solutions: state of the art in ab initio molecular dynamics. *Philos. Trans. R. Soc.*, 372(2011):20120482–20120482, 2014.

[48] Dominik Marx and Jürg Hutter. *Ab initio molecular dynamics: basic theory and advanced methods*. Cambridge University Press, 2009.

[49] Noam Agmon, Huib J. Bakker, R. Kramer Campen, Richard H. Henchman, Peter Pohl, Sylvie Roke, Martin Thämer, and Ali Hassanali. Protons and Hydroxide Ions in Aqueous Systems. *Chem. Rev.*, 116(13):7642–7672, 2016.

[50] Barbara Kirchner, Philipp J di Dio, and Jürg Hutter. Real-World Predictions from Ab Initio Molecular Dynamics Simulations. In Barbara Kirchner and Jadran Vrabec, editors, *Multiscale Mol. Methods Appl. Chem.*, pages 109–153. Springer Berlin Heidelberg, Berlin, Heidelberg, 2012.

[51] Mark E. Tuckerman, Amalendu Chandra, and Dominik Marx. Structure and dynamics of OH - (aq). *Acc. Chem. Res.*, 39(2):151–158, 2006.

[52] M E Tuckerman. Ab initio molecular dynamics: basic concepts, current trends and novel applications. *J. Phys. Condens. Matter.*, 14(50):R1297–R1355, 2002.

[53] Mauro Ferrario, Giovanni Ciccotti, and Kurt Binder. *Computer simulations in condensed matter: from materials to chemical biology*, volume 1. Springer, 2007.

[54] Michael P Allen and Dominic J Tildesley. *Computer simulation of liquids*. Oxford university press, 2017.

[55] Christopher J Mundy and I-Feng W Kuo. First-principles approaches to the structure and reactivity of atmospherically relevant aqueous interfaces. *Chem. Rev.*, 106(4):1282–1304, 2006.

[56] John S. Tse. Ab Initio Molecular Dynamics with Density Functional Theory. *Annu. Rev. Phys. Chem.*, 53(1):249–290, 2002.

[57] Kari Laasonen, M Sprik, M Parrinello, and R Car. "ab initio"liquid water. *J. Chem. Phys.*, 99(11):9080–9089, 1993.

[58] Mark Tuckerman, Kari Laasonen, Michiel Sprik, and Michele Parrinello. Ab initio molecular dynamics simulation of the solvation and transport of h3o+ and oh-ions in water. *J. Phys. Chem.*, 99(16):5749–5752, 1995.

[59] Mark Tuckerman, Kari Laasonen, Michiel Sprik, and Michele Parrinello. Ab initio molecular dynamics simulation of the solvation and transport of hydronium and hydroxyl ions in water. *J. Chem. Phys.*, 103(1):150–161, 1995.

[60] CJT De Grotthuss. *Mémoire sur la décomposition de l'eau: et des corps qu'elle tient en dissolution à l'aide de l'électricité galvanique*. 1805.

[61] Dominik Marx. Proton transfer 200 years after Von Grotthuss: Insights from ab initio simulations. *ChemPhysChem*, 7(9):1849–1870, 2006.

[62] Mark E Tuckerman, Dominik Marx, and Michele Parrinello. The nature and transport mechanism of hydrated hydroxide ions in aqueous solution. *Nature*, 417(6892):925–929, 2002.

[63] Dominik Marx, Mark E Tuckerman, Jürg Hutter, and Michele Parrinello. The nature of the hydrated excess proton in water. *Nature*, 397(6720):601–604, 1999.

[64] M Eigen and L De Maeyer. Self-dissociation and protonic charge transport in water and. In *Proc. R. Soc. Lond. A*, volume 247, pages 505–533. The Royal Society, 1958.

[65] Emad F Aziz, Niklas Ottosson, Manfred Faubel, Ingolf V Hertel, and Bernd Winter. Interaction between liquid water and hydroxide revealed by core-hole de-excitation. *Nature*, 455(7209):89, 2008.

[66] Anan Tongraar, Klaus R Liedl, and Bernd M Rode. Born- oppenheimer ab initio qm/mm dynamics simulations of na+ and k+ in water: From structure making to structure breaking effects. *J. Phys. Chem. A*, 102(50):10340–10347, 1998.

[67] A V Egorov, A V Komolkin, V I Chizhik, P V Yushmanov, A P Lyubartsev, and Aatto Laaksonen. Temperature and concentration effects on Li+-ion hydration. A molecular dynamics simulation study. *J. Phys. Chem. B*, 107(14):3234–3242, 2003.

[68] Jody A. White, Eric Schwegler, Giulia Galli, and François Gygi. The solvation of Na+ in water: First-principles simulations. *J. Chem. Phys.*, 113(11):4668–4673, sep 2000.

[69] Lavanya M Ramaniah, Marco Bernasconi, and Michele Parrinello. Ab initio molecular-dynamics simulation of k+ solvation in water. *J. Chem. Phys.*, 111(4):1587–1591, 1999.

[70] Yi Liu, Haigang Lu, Yanbo Wu, Tuoping Hu, and Qiaoling Li. Hydration and coordination of simulation K+ solvation in water from ab initio molecular-dynamics. *J. Chem. Phys.*, 132(124503):1–4, 2010.

[71] Christian Krekeler, Berk Hess, Luigi Delle Site, and The Halide ions. Density functional study of ion hydration for the alkali metal ions (Li+, Na+, K+) and the halide ions (F-, Br-, Cl-). *J. Chem. Phys.*, 125(10):54305–14501, 2006.

[72] Sergei Izvekov and Michael R Philpott. Ab initio molecular dynamics simulation of LiBr association in water. *J. Chem. Phys.*, 113(23):10676–10684, 2000.

[73] Diedrich A Schmidt, Roberto Scipioni, and Mauro Boero. Water solvation properties: An experimental and theoretical investigation of salt solutions at finite dilution. *J. Phys. Chem. A*, 113(27):7725–7729, 2009.

[74] I Bako, J Hutter, and G Palinkas. Car–parrinello molecular dynamics simulation of the hydrated calcium ion. *J. Chem. Phys.*, 117(21):9838–9843, 2002.

[75] Felice C Lightstone, Eric Schwegler, Markus Allesch, François Gygi, and Giulia Galli. A first-principles molecular dynamics study of calcium in water. *ChemPhysChem*, 6(9):1745–1749, 2005.

[76] Dominik Marx, Michiel Sprik, and Michele Parrinello. Ab initio molecular dynamics of ion solvation. the case of be2+ in water. *Chem. Phys. Lett.*, 273(5):360–366, 1997.

[77] Takashi Ikeda, Mauro Boero, and Kiyoyuki Terakura. Hydration properties of magnesium and calcium ions from constrained first principles molecular dynamics. *J. Chem. Phys.*, 127(7):074503, 2007.

[78] Cristian Faralli, Marco Pagliai, Gianni Cardini, and Vincenzo Schettino. Ab initio molecular dynamics study of Mg2+ and Ca2+ ions in liquid methanol. *J. Chem. Theory Comput.*, 4(1):156–163, 2008.

[79] Felice C Lightstone, Eric Schwegler, Randolph Q Hood, François Gygi, and Giulia Galli. A first principles molecular dynamics simulation of the hydrated magnesium ion. *Chem. Phys. Lett.*, 343(5):549–555, 2001.

[80] Josef Kapitán, Martin Dračínský, Jakub Kaminský, Ladislav Benda, and Petr Bouř. Theoretical modeling of magnesium Ion imprints in the Raman scattering of water. *J. Phys. Chem. B*, 114(10):3574–3582, 2010.

[81] Waheed A Adeagbo, Nikos L Doltsinis, Michael Burchard, Walter V Maresch, and Thomas Fockenberg. Ca2+ solvation as a function of p, t, and ph from ab initio simulation. *J. Chem. Phys.*, 137(12):124502, 2012.

[82] Teodora Todorova, Philippe H. Hunenberger, and Jurg Hutter. Car-parrinello molecular dynamics simulations of CaCl2 aqueous solutions. *J. Chem. Theory Comput.*, 4(5):779–789, 2008.

[83] Devis Di Tommaso and Nora H de Leeuw. Structure and dynamics of the hydrated magnesium ion and of the solvated magnesium carbonates: insights from first principles simulations. *Phys. Chem. Chem. Phys.*, 12(4):894–901, 2010.

[84] Kari Laasonen and Michael L. Klein. Ab Initio Molecular Dynamics Study of Hydrochloric Acid in Water. *J. Am. Chem. Soc.*, 116(25):11620–11621, 1994.

[85] L Petit, R Vuilleumier, P Maldivi, and C Adamo. Ab Initio Molecular Dynamics Study of a Highly

Concentrated LiCl Aqueous Solution. *J. Chem. Theory Comput.*, 4(7):1040–1048, 2008.

[86] Simone Raugei and Michael L Klein. Dynamics of water molecules in the Br- solvation shell: An ab initio molecular dynamics study. *J. Am. Chem. Soc.*, 123(38):9484–9485, 2001.

[87] M F Kropman. Dynamics of Water Molecules in Aqueous Solvation Shells. *Science (80-.).*, 291(5511):2118–2120, 2001.

[88] Karl Laasonen and Michael L. Klein. Ab initio molecular dynamics study of dilute hydrofluoric acid. *Mol. Phys.*, 88(1):135–142, 19996.

[89] Dominik Marx and Jurg Hutter. *Modern methods and algorithms of quantum chemistry*. John von Neumann Institute for Computing (NIC), 2000.

[90] JM Heuft and EJ Meijer. Density functional theory based molecular-dynamics study of aqueous chloride solvation. *J. Chem. Phys.*, 119(22):11788–11791, 2003.

[91] JM Heuft and EJ Meijer. Density functional theory based molecular-dynamics study of aqueous fluoride solvation. *J. Chem. Phys.*, 122(9):094501, 2005.

[92] JM Heuft and EJ Meijer. Density functional theory based molecular-dynamics study of aqueous iodide solvation. *J. Chem. Phys.*, 123(9):094506, 2005.

[93] JM Heuft and EJ Meijer. A density functional theory based study of the microscopic structure and dynamics of aqueous hcl solutions. *Phys. Chem. Chem. Phy.*, 8(26):3116–3123, 2006.

[94] J. M. Heuft. *An ab Initio Study of Ion Solvation in Water*. PhD thesis, 2006.

[95] Markus Kreitmeir, Helmut Bertagnolli, Jens Jørgen Mortensen, and Michele Parrinello. Ab initio molecular dynamics simulation of hydrogen fluoride at several thermodynamic states. *J. Chem. Phys.*, 118(8):3639–3645, 2003.

[96] Anan Tongraar and Bernd Michael Rode. Dynamical properties of water molecules in the hydration shells of na+ and k+: ab initio qm/mm molecular dynamics simulations. *Chem. Phys. Lett.*, 385(5):378–383, 2004.

[97] Christopher N Rowley and Benoıt Roux. The solvation structure of na+ and k+ in liquid water determined from high level ab initio molecular dynamics simulations. *J. Chem. Theory Comput.*, 8(10):3526–3535, 2012.

[98] Arindam Bankura, Vincenzo Carnevale, and Michael L Klein. Hydration structure of na+ and k+ from ab initio molecular dynamics based on modern density functional theory. *Mol. Phys.*, 112(9-10):1448–1456, 2014.

[99] Arindam Bankura, Vincenzo Carnevale, and Michael L Klein. Hydration structure of salt solutions from ab initio molecular dynamics. *J. Chem. Phys.*, 138(1):014501, 2013.

[100] M Galib, MD Baer, LB Skinner, CJ Mundy, T Huthwelker, GK Schenter, CJ Benmore, N Govind, and John L Fulton. Revisiting the hydration structure of aqueous na+. *J. Chem. Phys.*, 146(8):084504, 2017.

[101] Stuart Bogatko, Emilie Cauët, Eric Bylaska, Gregory Schenter, John Fulton, and John Weare. The aqueous ca2+ system, in comparison with zn2+, fe3+, and al3+: an ab initio molecular dynamics study. *Chem. Eur. J.*, 19(9):3047–3060, 2013.

[102] Anan Tongraar, Klaus R Liedl, and Bernd M Rode. Solvation of ca2+ in water studied by born-oppenheimer ab initio qm/mm dynamics. *J. Phys. Chem. A*, 101(35):6299–6309, 1997.

[103] Christian F Schwenk, Hannes H Loeffler, and Bernd M Rode. Molecular dynamics simulations of ca2+ in water: comparison of a classical simulation including three-body corrections and born–oppenheimer ab initio and density functional theory quantum mechanical/molecular mechanics simulations. *J. Chem. Phys.*, 115(23):10808–10813, 2001.

[104] Sami Amira, Daniel Spångberg, Michael Probst, and Kersti Hermansson. Molecular dynamics simulation of fe2+ (aq) and fe3+ (aq). *J. Phys. Chem. B*, 108(1):496–502, 2004.

[105] E Guàrdia and JA Padró. Molecular dynamics simulation of ferrous and ferric ions in water. *Chem.Phys.*, 144(3):353–362, 1990.

[106] Sami Amira, Daniel Spångberg, Viktor Zelin, Michael Probst, and Kersti Hermansson. Car- parrinello molecular dynamics simulation of fe3+ (aq). *J. Phys. Chem. B*, 109(29):14235–14242, 2005.

[107] Sami Amira, Daniel Spångberg, and Kersti Hermansson. Distorted five-fold coordination of cu 2+(aq) from a car–parrinello molecular dynamics simulation. *Phys. Chem. Chem. Phys.*, 7(15):2874–2880, 2005.

[108] Alfredo Pasquarello, Ingrid Petri, Philip S Salmon, Olivier Parisel, Roberto Car, Éva Tóth, D Hugh Powell, Henry E Fischer, Lothar Helm, and André E Merbach. First solvation shell of the cu (ii) aqua ion: evidence for fivefold coordination. *Science*, 291(5505):856–859, 2001.

[109] Thomas W Swaddle, Jörgen Rosenqvist, Ping Yu, Eric Bylaska, Brian L Phillips, and William H Casey. Kinetic evidence for five-coordination in aloh (aq) 2+ ion. *Science*, 308(5727):1450–1453, 2005.

[110] Aymeric Sadoc, Sabri Messaoudi, Eric Furet, Régis Gautier, Eric Le Fur, Laurent Le Pollès, and Jean-Yves Pivan. Structure and stability of vo2+ in aqueous solution: A car- parrinello and static ab initio study. *Inorg. Chem.*, 46(12):4835–4843, 2007.

[111] Michael Bühl, Frank T Mauschick, Frank Terstegen, and Bernd Wrackmeyer. Remarkably large geometry dependence of 57fe nmr chemical shifts. *Angew. Chem. Int. Ed.*, 41(13):2312–2315, 2002.

[112] Michael Bühl and Ingmar Grenthe. Binding modes of oxalate in uo2 (oxalate) in aqueous solution studied with first-principles molecular dynamics simulations. implications for the chelate effect. *Dalton Trans.*, 40(42):11192–11199, 2011.

[113] Laia Vila-Nadal, Elizabeth F Wilson, Haralampos N Miras, Antonio RodrÌguez-Fortea, Leroy Cronin, and Josep M Poblet. Combined theoretical and mass spectrometry study of the formation-fragmentation of small polyoxomolybdates. *Inorg. Chem.*, 50(16):7811–7819, 2011.

[114] Michael Bühl and Michele Parrinello. Medium effects on 51v nmr chemical shifts: a density functional study. *Chem. Eur. J.*, 7(20):4487–4494, 2001.

[115] Michael Bühl, Sonja Grigoleit, Hendrik Kabrede, and Frank T Mauschick. Simulation of 59co nmr chemical shifts in aqueous solution. *Chem. Eur. J.*, 12(2):477–488, 2006.

[116] Michael Bühl. Structure, dynamics, and magnetic shieldings of permanganate ion in aqueous solution. a density functional study. *J. Phys. Chem. A*, 106(44):10505–10509, 2002.

[117] Kevin Leung, Ida MB Nielsen, and Ira Kurtz. Ab initio molecular dynamics study of carbon dioxide and bicarbonate hydration and the nucleophilic attack of hydroxide on co2. *J. Phys. Chem. B*, 111(17):4453–4459, 2007.

[118] Zhenhao Duan and Zhigang Zhang. Equation of state of the h2o, co2, and h2o–co2 systems up to

10 gpa and 2573.15 k: Molecular dynamics simulations with ab initio potential surface. *Geochim. Cosmochim. Acta*, 70(9):2311–2324, 2006.

[119] Bo Han, Yubao Sun, Maohong Fan, and Hansong Cheng. On the co2 capture in water-free monoethanolamine solution: an ab initio molecular dynamics study. *J. Phys. Chem. B*, 117(19):5971–5977, 2013.

[120] Moumita Saharay and Sundaram Balasubramanian. Ab initio molecular-dynamics study of supercritical carbon dioxide. *J. Chem. Phys.*, 120(20):9694–9702, 2004.

[121] P Padma Kumar, Andrey G Kalinichev, and R James Kirkpatrick. Hydrogen-bonding structure and dynamics of aqueous carbonate species from car- parrinello molecular dynamics simulations. *J. Phys. Chem. B*, 113(3):794–802, 2008.

[122] Fabien Bruneval, Davide Donadio, and Michele Parrinello. Molecular dynamics study of the solvation of calcium carbonate in water. *J. Phys. Chem. B*, 111(42):12219–12227, 2007.

[123] Viwat Vchirawongkwin, Chinapong Kritayakornupong, Anan Tongraar, and Bernd M Rode. Symmetry breaking and hydration structure of carbonate and nitrate in aqueous solutions: a study by ab initio quantum mechanical charge field molecular dynamics. *J. Phys. Chem. B*, 115(43):12527–12536, 2011.

[124] Hiroto Tachikawa and Andrew J Orr-Ewing. Ab initio molecular dynamics study on the electron capture processes of protonated methane (ch5+). *J. Phys. Chem. A*, 112(46):11575–11581, 2008.

[125] Masaki Hiratsuka, Ryo Ohmura, Amadeu K Sum, and Kenji Yasuoka. Vibrational modes of methane in the structure h clathrate hydrate from ab initio molecular dynamics simulation. *J. Chem. Phys.*, 137(14):144306, 2012.

[126] Kevin Leung and Susan B Rempe. Ab initio molecular dynamics study of formate ion hydration. *J. Am. Chem. Soc.*, 126(1):344–351, 2004.

[127] Kevin Leung and Susan B Rempe. Ab initio molecular dynamics study of glycine intramolecular proton transfer in water. *J. Chem. Phys.*, 122(18):184506, 2005.

[128] Moumita Saharay and Sundaram Balasubramanian. Electron donor- acceptor interactions in ethanol- co2 mixtures: An ab initio molecular dynamics study of supercritical carbon dioxide. *J. Phys. Chem. B*, 110(8):3782–3790, 2006.

[129] Barbara Kirchner. Ionic liquids from theoretical investigations. In *Ionic liquids*, pages 213–262. Springer, 2008.

[130] András Stirling. Hco3–formation from co2 at high ph: Ab initio molecular dynamics study. *J. Phys. Chem. B*, 115(49):14683–14687, 2011.

[131] András Stirling and Imre Pápai. H2co3 forms via hco3- in water. *J. Phys. Chem. B*, 114(50):16854–16859, 2010.

[132] Mirza Galib and Gabriel Hanna. The role of hydrogen bonding in the decomposition of h2co3 in water: Mechanistic insights from ab initio metadynamics studies of aqueous clusters. *J. Phys. Chem. B*, 118(22):5983–5993, 2014.

[133] Anil Kumar Tummanapelli and Sukumaran Vasudevan. Dissociation constants of weak acids from ab initio molecular dynamics using metadynamics: Influence of the inductive effect and hydrogen bonding on p k a values. *J. Phys. Chem. B*, 118(47):13651–13657, 2014.

[134] Anil Kumar Tummanapelli and Sukumaran Vasudevan. Ab initio md simulations of the brønsted acidity of glutathione in aqueous solutions: Predicting p k a shifts of the cysteine residue. *J. Phys. Chem. B*, 119(49):15353–15358, 2015.

[135] Anil Kumar Tummanapelli and Sukumaran Vasudevan. Ab initio molecular dynamics simulations of amino acids in aqueous solutions: Estimating p k a values from metadynamics sampling. *J. Phys. Chem. B*, 119(37):12249–12255, 2015.

[136] Anil Kumar Tummanapelli and Sukumaran Vasudevan. Estimating successive pka values of polyprotic acids from ab initio molecular dynamics using metadynamics: the dissociation of phthalic acid and its isomers. *Phys. Chem. Chem. Phys.*, 17(9):6383–6388, 2015.

[137] Pavel Jungwirth and Douglas J Tobias. Specific ion effects at the air/water interface. *Chem. Rev.*, 106(4):1259–1281, 2006.

[138] I-Feng W Kuo and Christopher J Mundy. An ab initio molecular dynamics study of the aqueous liquid-vapor interface. *Science*, 303(5658):658–660, 2004.

[139] Pavel Jungwirth and Douglas J Tobias. Chloride anion on aqueous clusters, at the air- water interface, and in liquid water: Solvent effects on cl-polarizability. *J. Chem. Phys. A*, 106(2):379–383, 2002.

[140] Pedro Salvador, Joseph E Curtis, Douglas J Tobias, and Pavel Jungwirth. Polarizability of the nitrate anion and its solvation at the air/water interface. *Phys. Chem. Chem. Phys.*, 5(17):3752–3757, 2003.

[141] Thomas D Kühne, Tod A Pascal, Efthimios Kaxiras, and Yousung Jung. New insights into the structure of the vapor/water interface from large-scale first-principles simulations. *J. Phys. Chem. Lett.*, 2(2):105–113, 2010.

[142] Matt K Petersen, Srinivasan S Iyengar, Tyler JF Day, and Gregory A Voth. The hydrated proton at the water liquid/vapor interface. *J. Phys. Chem. B*, 108(39):14804–14806, 2004.

[143] Poul B Petersen and Richard J Saykally. Evidence for an enhanced hydronium concentration at the liquid water surface. *J. Phys. Chem. B*, 109(16):7976–7980, 2005.

[144] Victoria Buch, Anne Milet, Robert Vácha, Pavel Jungwirth, and J Paul Devlin. Water surface is acidic. *Proc. Natl. Acad. Sci. U.S.A.*, 104(18):7342–7347, 2007.

[145] Tsun-Mei Chang and Liem X Dang. Recent advances in molecular simulations of ion solvation at liquid interfaces. *Chem. Rev.*, 106(4):1305–1322, 2006.

[146] Francisco Zaera. Probing liquid/solid interfaces at the molecular level. *Chem. Rev.*, 112(5):2920–2986, 2012.

[147] Xianghong Qian, Mark R Nimlos, Mark Davis, David K Johnson, and Michael E Himmel. Ab initio molecular dynamics simulations of β-d-glucose and β-d-xylose degradation mechanisms in acidic aqueous solution. *Carbohydr. Res.*, 340(14):2319–2327, 2005.

[148] Xianghong Qian and Xingfei Wei. Glucose isomerization to fructose from ab initio molecular dynamics simulations. *J. Chem. Phys. B*, 116(35):10898–10904, 2012.

[149] Vinit Choudhary, Samir H Mushrif, Christopher Ho, Andrzej Anderko, Vladimiros Nikolakis, Nebojsa S Marinkovic, Anatoly I Frenkel, Stanley I Sandler, and Dionisios G Vlachos. Insights into the interplay of lewis and brønsted acid catalysts in glucose and fructose conversion to 5-(hydroxymethyl)

furfural and levulinic acid in aqueous media. *J. Am. Chem. Soc.*, 135(10):3997–4006, 2013.

[150] Xianghong Qian. Mechanisms and energetics for brønsted acid-catalyzed glucose condensation, dehydration and isomerization reactions. *Top. Catal.*, 55(3-4):218–226, 2012.

[151] Hans Martin Senn and Walter Thiel. Qm/mm methods for biological systems. In *Atomistic approaches in modern biology*, pages 173–290. Springer, 2006.

[152] Ute F Röhrig, Irmgard Frank, Jürg Hutter, Alessandro Laio, Joost VandeVondele, and Ursula Rothlisberger. Qm/mm car-parrinello molecular dynamics study of the solvent effects on the ground state and on the first excited singlet state of acetone in water. *ChemPhysChem*, 4(11):1177–1182, 2003.

[153] Xevi Biarnes, Albert Ardevol, Javier Iglesias-Fernandez, Antoni Planas, and Carme Rovira. Catalytic itinerary in 1, 3-1, 4-β-glucanase unraveled by qm/mm metadynamics. charge is not yet fully developed at the oxocarbenium ion-like transition state. *J. Am. Chem. Soc.*, 133(50):20301–20309, 2011.

[154] Matteo Dal Peraro, Paolo Ruggerone, Simone Raugei, Francesco Luigi Gervasio, and Paolo Carloni. Investigating biological systems using first principles car–parrinello molecular dynamics simulations. *Curr Opin Struct Biol.*, 17(2):149–156, 2007.

CHAPTER 2

THEORETICAL BACKGROUNDS

2.1 Introduction

The rapid enhancement in the computational resources over the last three decades, as well as developments of smart and efficient algorithms have enhanced the scope and reliability of computational studies in research [1–4]. Computational techniques involves numerical solution of a model of the experimental system or a process of specific interest [2]. Such studies are particularly useful when the actual mechanism of the process of interest is unknown or when experiments are hard to be performed [2, 3, 5]. Many a times computational studies are employed to predict the outcome of an experiment among numerous possibilities. Computational studies also help in bridging the gap between theory and laboratory experiments, highlighting the critical areas where the theoretical model need refinement or in aid of better interpretation of certain experimental results [2]. Such approaches are now routinely applied in different branches of science [2, 5].

Molecular dynamics (MD) and Monte Carlo (MC) simulations are two popular atomistic computational techniques, that find applications in various areas of physics, physical chemistry, materials science, bio-physics, etc [2, 3, 6]. While the former provides real time evolution of a physical system by *iteratively* solving the Newton's equation of motion, the latter computes the thermodynamic properties through *stochastic* sampling of the phase-space. However, both these methods share the same core, evaluating the interatomic interaction forces from the atomic coordinates, that essentially lead to the same

thermodynamic average of a quantity, under ergodic hypothesis [2, 3, 7]. The results presented in this thesis are based on extensive MD simulations, details of which are discussed below.

2.2 Molecular Dynamics

Molecular dynamics (MD) technique is one of the most popular computer simulation methods that evolved since the pioneering works by Alder and Wainwright in 1950s [6, 8–10], on the phase-transitions of hard sphere system. The study was extended to a realistic physical system, that of liquid argon, in 1964 by Rahman [11]. Rahman's work demonstrated the applicability of the technique as well as its complementarity with experiments. This prompted the simulation of the more challenging system such as liquid water, by Rahman and Stillinger in 1974 [12, 13]. The field has witnessed tremendous developments since then. Immensely assisted by the unprecedented growth in silicon technology, the technique quickly evolved in to a valuable tool, and is now routinely applied in many areas of science.

MD is a numerical technique for solving the classical many body problem for a collection of atoms, ions or molecules, for which analytical solution is not possible. As mentioned above MD simulation involves solving the Newton's equation of motion *iteratively* based on known/computed inter-atomic interactions. There are mainly two varieties of it, based on the way inter-atomic forces are calculated - (a) classical molecular dynamics, that is based on predefined inter-atomic forces or potentials, and (b) *ab initio* molecular dynamics (AIMD), which computes the forces on the fly employing the first principle-based solution of the electronic structure of the system [2, 3, 14–18]. However, in both the cases, the heavy nuclei are propagated classically, using Newton's equations of motion.

2.2.1 Classical MD

Classical MD simulation employs *predefined* inter-atomic or inter-molecular potentials to propagate the coordinates and velocities of atoms/molecules of the system using Newton's laws motion [2, 3, 18],

$$M_I \frac{d^2\vec{R}_I}{dt^2} = \vec{F}_I\left(\vec{R}\right) = -\vec{\nabla}V\left(\vec{R}\right), \tag{2.1}$$

where M_I and $\vec{R}_I$ stand for mass and coordinate of the I^{th} atom. Force ($\vec{F}_I$) on it is computed from the negative gradient of interaction potential $V(\vec{R})$, as a function of the coordinates of all the atoms of the system, $\vec{R} = \{\vec{R}_I\}$. The basic algorithm of MD is shown in Fig.2.1. One has to provide the initial positions and velocities of the atoms as

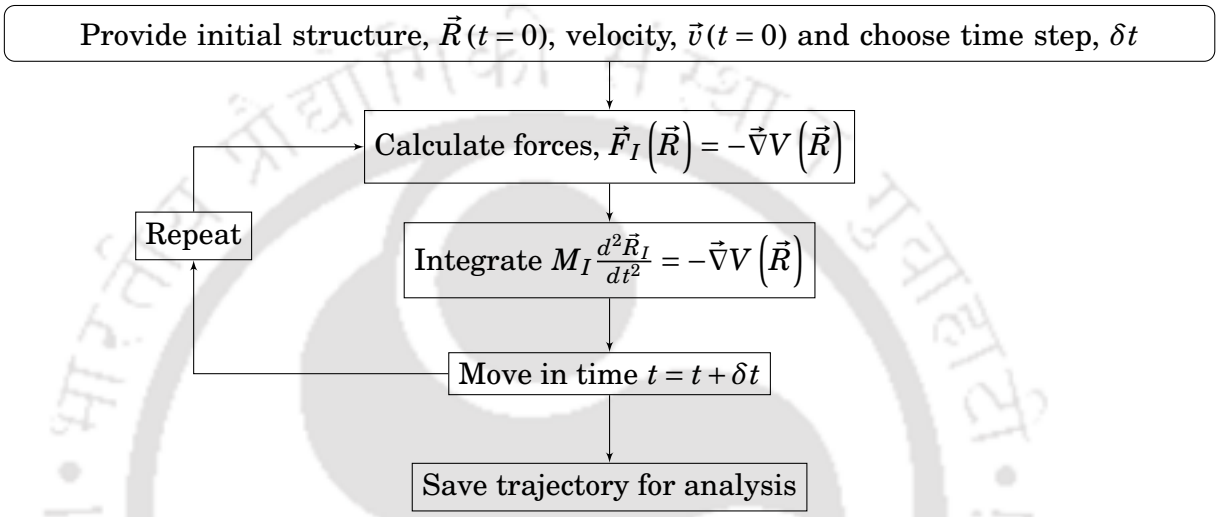

Figure 2.1: A basic algorithm of Molecular Dynamics (MD) simulation technique.

inputs in order to solve the second order differential equation (Eq. (2.1)) by integration. The initial coordinates may be taken from experimental data, where available. On the other hand, the initial velocities can be generated from a Maxwellian distribution for the target temperature. Then at every MD step the forces on atoms are computed (from the predefined interaction potential) that are integrated numerically to compute the coordinates and velocities, and move forward in time in terms of short intervals, δt, which is typically of the order of femto-seconds.

There are different numerical integration schemes for solving second order ordinary differential equations such as Euler method, Runge-Kutta (RK) methods, etc., but these do not yield stable MD runs, as these methods are non-sympletic in nature (do not conserve the phase space volume) [10, 15, 19]. Besides being sympletic, a good MD integrator should possess two main properties – long-time energy conservation and and short time reversibility. Often the method of choice is the velocity Verlet algorithm [2, 10, 19, 20]. This algorithm has the advantage of using coordinates and velocities at

the same instant t,

$$\vec{R}(t+\delta t) = \vec{R}(t) + \vec{v}(t)\delta t + \frac{1}{2}\frac{\vec{F}(t)}{M}\delta t^2 \tag{2.2a}$$

$$\vec{v}(t+\delta t) = \vec{v}(t) + \frac{\delta t}{2M}\left(\vec{F}(t+\delta t) + \vec{F}(t)\right), \tag{2.2b}$$

where Eq. (2.2a) can be obtained as the Taylor expansion of $\vec{R}(t+\delta t)$. Eq. (2.2b) can be derived from the Taylor expansion of $\vec{v}(t+\delta t)$ and $\dot{\vec{v}}(t+\delta t)$.

Although classical MD approach is often very useful in the study of physical properties of matter, it suffers from certain shortcomings due to poor transferability of interaction parameters across systems and phases, preclusion of many-body interactions, etc., and fails to describe chemical changes in matter [10, 15, 21, 22]. For example, processes involving bond making/breaking phenomena can not be studied using classical MD. For studying such *complex* systems with *itinerant* electrons, *ab initio* Molecular Dynamics (AIMD) is used, where the forces are calculated *on-the-fly* from accurate electronic structure calculations [14, 16, 17, 21–24]. This is briefly discussed below, closely following the excellent book on this subject matter, by Marx and Hütter [23].

2.2.2 Ab Initio Molecular Dynamics

Ab initio molecular dynamics (AIMD) is an advanced MD technique in which the finite temperature trajectories are generated with forces obtained directly from accurate *on the fly* electronic structure calculations and no *empirical* parameter is required. Studies during the last three decades have demonstrated the utility of the method in capturing the chemical as well as physical properties of matter [15, 19, 21, 22]. Although the AIMD technique is computationally very expensive, thereby limiting the length and time scales of simulations, it still finds numerous applications across various domains of science such as in, materials science, bio-physics, nano clusters, catalysis, matter at extreme conditions, etc [2, 15, 25–34].

The goal of quantum many body physics is to obtain approximate solutions to the time-dependent Schrödinger equation (TDSE) [35, 36], given by,

$$i\hbar\frac{\partial}{\partial t}\Psi\left(\{\vec{r}_i\},\vec{R};t\right) = H\Psi\left(\{\vec{r}_i\},\vec{R};t\right) \tag{2.3}$$

where the many body Hamiltonian operator is given by,

$$H = T_N + T_e + V_{ee} + V_{Ne} + V_{NN} \tag{2.4a}$$

$$= -\frac{1}{2}\sum_I \frac{1}{M_I}\vec{\nabla}_I^2 - \frac{1}{2}\sum_i \vec{\nabla}_i^2 + \sum_{i<j}\frac{1}{|\vec{r}_i - \vec{r}_j|} - \sum_{I,i}\frac{Z_I}{|\vec{R}_I - \vec{r}_i|} + \sum_{I<J}\frac{Z_I Z_J}{|\vec{R}_I - \vec{R}_J|} \tag{2.4b}$$

$$= -\sum_I \frac{\vec{\nabla}_I^2}{2M_I} + H_e(\{\vec{r}_i\},\vec{R}) \tag{2.4c}$$

for the electronic ($\vec{r}_i$) and nuclear ($\vec{R}$) degrees of freedom (DOF) in atomic units. M_I and Z_I are the mass and atomic number of the I^{th} nucleus respectively. $H_e(\{\vec{r}_i\},\vec{R})$ is the electronic part of the $H(\{\vec{r}_i\},\vec{R})$. $\Psi\left(\{\vec{r}_i\},\vec{R};t\right)$ is the total wavefunction obtained from solving time dependent Schrödinger Eq. (2.3).

Applying the so called *Born-Oppenheimer approximation* [23, 36, 37], which states that the electrons remains in the instantaneous equilibrium positions of the heavy nuclei, the T_N term in Eq. (2.4) can be neglected in comparison to T_e and hence, the many body problem becomes a complete electronic structure problem with Hamiltonian $H_e(\{\vec{r}_i\};\{\vec{R}_I\})$. This approximation essentially allows for a product ansatz [23, 38, 39] of the total wave function consisting of the nuclear and electronic wave functions,

$$\Psi\left(\{\vec{r}_i\},\vec{R};t\right) = \psi\left(\{\vec{r}_i\};\vec{R}\right) \times \xi\left(\vec{R};t\right). \tag{2.5}$$

As the electrons remains in instantaneous equilibrium with the heavy nuclei $H_e\left(\{\vec{r}_i\};\vec{R}\right)$ can be written as parametrically dependent on nuclei positions, and restrict ourselves solving the time-independent, many-body Schrödinger equation for the ground state electronic sub-system,

$$H_e\left(\{\vec{r}_i\};\vec{R}\right)\psi_0(\{\vec{r}_i\}) = \epsilon_0\left(\vec{R}\right)\psi_0(\{\vec{r}_i\}), \tag{2.6}$$

where $\epsilon_0\left(\vec{R}\right)$ are the ground state eigen values. Once the electronic structure problem is solved the forces on the ions can be computed by using

$$\vec{F}_I = -\nabla_I \langle\psi_0|H_e|\psi_0\rangle, \tag{2.7}$$

which is integrated to propagate the atoms, as explained above.

Ehrenfest Molecular Dynamics

This method is based on numerical computation of Ehrenfest force, $-\vec{\nabla}_I \langle H_e \rangle$ for each configuration $\vec{R}_I(t)$, the time-dependent Schrödinger equation for the electrons [10, 40]:

$$M_I \ddot{\vec{R}}_I = -\vec{\nabla}_I \langle \psi_0 | H_e | \psi_0 \rangle \tag{2.8a}$$

$$i\hbar \frac{\partial \psi_0}{\partial t} = H_e \psi_0 \tag{2.8b}$$

This approach includes the non-adiabatic transitions between different electronic states rigorously. Being computationally very expensive, this method finds its applications in studying systems with a few degrees of freedom. More recently, this approach has been applied in time dependent density functional theory (TDDFT) to study systems at excited states, as an alternative to Hartree-Fock approach [15].

Born-Oppenheimer Molecular Dynamics

Born-Oppenheimer Molecular Dynamics (BOMD), in contrast to Ehrenfest-MD, is based on computation of the time-independent Schrödinger equation of electrons for each nuclear configuration $\vec{R}_I$, and the time evolution is dictated by its parametric dependence on the classical dynamics of the nuclei [41–44],

$$M_I \ddot{\vec{R}}_I(t) = -\vec{\nabla}_I \min_{\psi_0} \{ \langle \psi_0 | H_e | \psi_0 \rangle \} \tag{2.9a}$$

$$H_e \psi_0 = \epsilon_0 \psi_0 \tag{2.9b}$$

Unlike in Ehrenfest-MD, the minimum of $\langle H_e \rangle$ has to be achieved in every MD step. Eq. (2.9b) is computed using electronic structure methods, such as the density functional theory (DFT). DFT casts the many body electron problem to an effective one particle Hamiltonian, with total wave functions $\Psi_0 = \det\{\phi_i\}$, where ϕ_is are one electron wavefunction that satisfies the orthonormality condition, $\langle \phi_i | \phi_j \rangle = \delta_{ij}$. The dynamics of BOMD is described by the following Lagrangian,

$$\mathscr{L}_{\mathrm{BO}} = \frac{1}{2} M_I \dot{\vec{R}}_I^2 - \langle \psi_0 | H_e | \psi_0 \rangle + \sum_{i,j} \Lambda_{ij} \left(\langle \phi_i | \phi_j \rangle - \delta_{ij} \right), \tag{2.10}$$

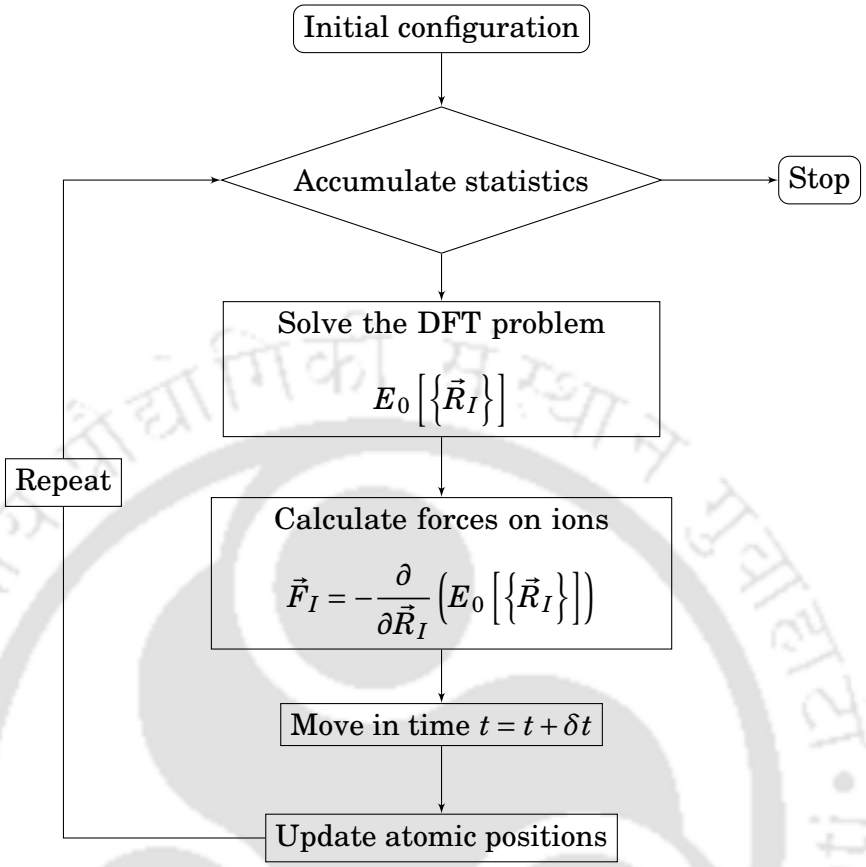

Figure 2.2: Basic Born-Oppenheimer molecular dynamics algorithm.

where Λ_{ij} are the Lagrange multipliers to maintain the orthonormality constraints. Now, using Euler-Lagrange equations,

$$\frac{d}{dt}\left(\frac{\partial \mathscr{L}}{\partial \dot{\vec{R}}_I}\right) = \frac{\partial \mathscr{L}}{\partial \vec{R}_I} \tag{2.11a}$$

$$\frac{d}{dt}\left(\frac{\partial \mathscr{L}}{\delta \dot{\phi}_i^*}\right) = \frac{\delta \mathscr{L}}{\delta \phi_i^*} \tag{2.11b}$$

we get,

$$M_I \ddot{\vec{R}}_I(t) = -\vec{\nabla}_I \min_{\{\phi_i\}} \left\{\langle \psi_0 | H_e | \psi_0 \rangle\right\} \tag{2.12a}$$

$$H_e \phi_i = \sum_j \Lambda_{ij} \phi_j = \epsilon_i \phi_i \tag{2.12b}$$

Although BOMD is much lighter compared to Ehrenfest-MD from the point of view of computational overhead, it still remains quite expensive to be successfully applied for most real world problems. Early applications of BOMD have been performed with

semi-empirical approximations and then later with HF approaches. However, recent implementations of BOMD with DFT have been found to carry great success enabling dynamics to be simulated in a tractable manner for small systems. The main hurdle so far is the time needed for computing electronic structure at each MD step. However, in 1985, Roberto Car and Michele Parrinello [14] proposed a scheme to sidestep the impediments of solving the electronic structures at every MD step, which revolutionized the field of *ab initio* MD simulations.

Car-Parrinello Molecular Dynamics

Fundamental idea of Car-Parrinello Molecular Dynamics (CPMD) [14, 23] is to exploit the adiabatic time scale separation between the electron (fast) and the nucleus (slow) degrees of freedom. In CPMD, the whole system is mapped into a two-component pure classical system, at the expense of the explicit time dependence of the fast electrons. Car and Parrinello introduced the following Lagrangian to account for the electron-nuclei system [14],

$$\mathscr{L}_{\mathrm{CP}} = \frac{1}{2}M_I\dot{\vec{R}}_I^2 + \sum_i \mu\left\langle\dot{\phi}_i|\dot{\phi}_i\right\rangle - \langle\psi_0|H_e^{\mathrm{KS}}|\psi_0\rangle + \sum_{i,j}\Lambda_{ij}\left(\langle\phi_i|\phi_j\rangle - \delta_{ij}\right), \tag{2.13}$$

where the additional term added to $\mathscr{L}_{CP}$, compared to Eq. (2.10), is the *fictitious* kinetic energy term for the electron orbitals $\{\phi\}$. μ is known as the *fictitious mass* of the electrons or inertial parameter assigned to $\{\phi\}$. Applying Euler-Lagrange equation [45], Eqs. (2.11a)-(2.11b), we get two equations of motion, one for the nuclei and other for the electrons,

$$M_I\ddot{\vec{R}}_I(t) = -\vec{\nabla}_I\left\langle\psi_0|H_e^{\mathrm{KS}}|\psi_0\right\rangle \tag{2.14a}$$

$$\mu\ddot{\phi}_i(t) = -H_e^{\mathrm{KS}}\phi_i + \sum_j \Lambda_{ij}\phi_j, \tag{2.14b}$$

where H_e^{KS} is the Kohn-Sham electronic Hamiltonian discussed later.

Since, kinetic energy is the predictor for temperature of the system, the two kinetic energy terms lead to two different instantaneous temperatures for nuclei and electronic subsystems respectively, where the latter $T_{\mathrm{fict.}} \propto \sum_i \mu\langle\dot{\phi}_i|\dot{\phi}_i\rangle$ is known as the *fictitious temperature* of the orbitals. The electrons should be maintained at a *low electronic temperature* or kept *cold* such that the electronic subsystem remains *close* to the exact BO surface, $\min_{\{\phi_i\}}\langle\phi|H_e|\phi\rangle$, following the slow nuclear motion adiabatically, during the

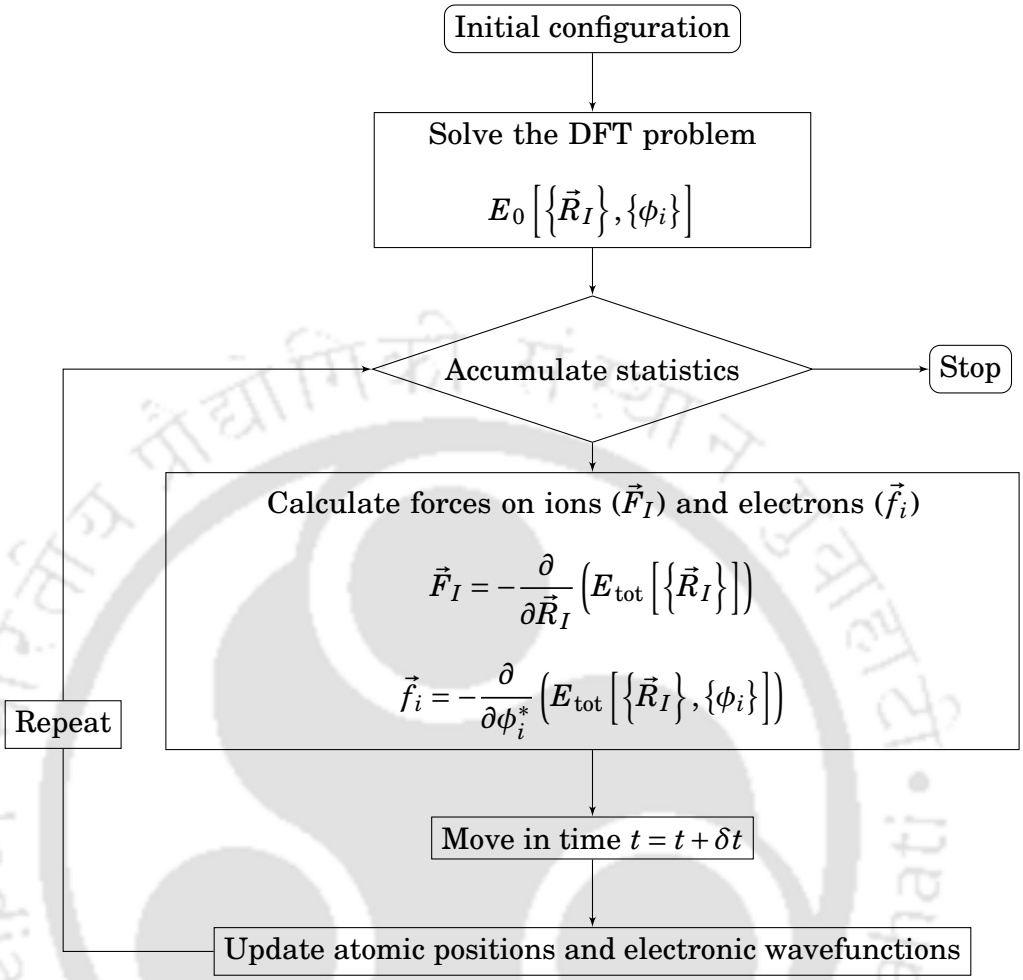

Figure 2.3: Basic Car-Parrinello molecular dynamics algorithm.

course of simulation. For the procedure to work, there should not be substantial overlap between the vibrational density of states of the two subsystems (in other words, a gap between highest phonon frequency and orbital frequency), such that no heat transfer of any kind can take place [46]. μ is found to be the parameter controlling this [14, 21, 23]. In a CPMD simulation run, there are four types of energies we have to care about:

$$E_{\text{cons}} = \frac{1}{2}M_I\dot{\vec{R}}_I^2 + \sum_i \mu\langle\dot{\phi}_i|\dot{\phi}_i\rangle + \langle\psi_0|H_e^{\text{KS}}|\psi_0\rangle, \tag{2.15a}$$

$$E_{\text{phys}} = \frac{1}{2}M_I\dot{\vec{R}}_I^2 + \langle\psi_0|H_e^{\text{KS}}|\psi_0\rangle, \tag{2.15b}$$

$$V_e = \langle\psi_0|H_e^{\text{KS}}|\psi_0\rangle, \tag{2.15c}$$

$$T_e = \sum_i \mu\langle\dot{\phi}_i|\dot{\phi}_i\rangle. \tag{2.15d}$$

E_{cons} should be a constant of motion for CPMD. V_e varies considerably with time, due

to phonon density of states (DOS). T_e performs a bound oscillatory motion around a constant value, which is a measure of the deviations from the BO surface. Amplitudes of T_e are about 3 times smaller than V_e and hence $E_{\text{phys}} = E_{\text{cons}} - T_e$ is also essentially constant.

There are two time scales of oscillation (frequency) of the electronic DOS. The first one arises from the drag force exerted by the moving nuclei, whose fluctuation is opposite to that of V_e, higher in amplitudes and slower in frequencies. The other one, intrinsic to the electronic degrees of freedom itself, is instrumental in the stability of CPMD and is of high frequencies, whose amplitudes are only a fraction of the first type (T_e). The intrinsic frequency of the electrons depends on the energy gap between the occupied and unoccupied orbitals and fictitious mass parameter (μ) [21, 46]:

$$\omega_e^{\min} \propto \left(\frac{E_{\text{gap}}}{\mu}\right)^{1/2}, \tag{2.16}$$

where E_{gap} is the energy difference between the LUMO (Lowest Unoccupied Molecular Orbital) and HOMO (Highest Occupied Molecular Orbital). In order to CPMD propagate smoothly, the difference $\omega_e^{\min} - \omega_n^{\max}$, where $\omega_n^{\max}$ is the highest phonon frequency for nuclei, should be large. E_{gap} being a system specific parameter, the only controlling parameter is μ, known as *adiabaticity parameter*. Now, decreasing the value of μ also stretches the frequency spectrum and therefore there is cut-off on E_{gap}:

$$\omega_e^{\max} \propto \left(\frac{E_{\text{cut}}}{\mu}\right)^{1/2}, \tag{2.17}$$

where E_{cut} is the largest KE in the wave-function expansion of the basis sets, discussed in subsequent sections. This gives a cut-off on the MD time step $\Delta t^{\max}$:

$$\Delta t^{\max} \propto \left(\frac{\mu}{E_{cut}}\right)^{1/2} \propto \omega_e^{\max} \tag{2.18}$$

Since, the maximum allowed time step of CPMD is determined by the maximum electron frequency, which in turn depends directly to the fictitious mass parameter μ, CPMD needs to make a compromise in choosing a typical value of $400 - 800\,a.u.$ for large gap systems, which allows a time step of about $5 - 10\,a.u.(0.12 - 0.24\,fs)$, depending on the mass of the lightest nuclear mass of the system [47].

The finite value of the fictitious mass parameter, μ, hampers the adiabatic decoupling of the motion of the nuclei and electrons in microcanonical (NVE) CPMD runs, allowing the dynamics to deviate from BO surface. Quench BO technique, in which the electrons

are periodically quenched to the BOMD, has been proposed, but it lacks any theoretical basis. The most often followed technique is therefore to used Canonical (NVT) ensemble dynamics, by thermostatting both the nuclei as well as the electronic DOFs, which allows them to oscillate slightly above the BO surface [23, 48].

Hellmann-Feynman Forces

A straightforward computation of the force on the nuclei by using $\vec{F}_I = -\vec{\nabla}_I \langle \psi_0 | H_e | \psi_0 \rangle$ is often too expensive and turns out to be highly inaccurate for AIMD simulations. Rather, it can be simplified as follows:

$$\begin{aligned} \vec{F}_I &= -\vec{\nabla}_I \langle \psi_0 | H_e | \psi_0 \rangle \\ &= -\langle \psi_0 | \vec{\nabla}_I H_e | \psi_0 \rangle - \langle \vec{\nabla}_I \psi_0 | H_e | \Psi_0 \rangle - \langle \Psi_0 | \mathscr{H}_e | \vec{\nabla}_I \psi_0 \rangle \end{aligned} \tag{2.19}$$

Hence, if the wave function is exact (or stationary), the contributions coming from $\vec{\nabla}_I \Psi_0$ vanish, under which Eq. (2.19) becomes,

$$\vec{F}_I^{\text{HFT}} = -\left\langle \psi_0 | \vec{\nabla}_I H_e | \psi_0 \right\rangle \tag{2.20}$$

This is known as the Hellmann-Feynman Theorem (HFT) [49–51]. Theoretically, this yields exact results provided the complete basis sets are used, which is not practicable in reality.

Which Method to Choose

The basic advantage of CPMD over BOMD is the fact that no diagonalization of the Hamiltonian is needed, except at the very first step. However, it limits the maximum allowed time-step of integration, which is about 10 times smaller than allowed in BOMD ($\tau_e^{\text{CPMD}} \approx \tau^{\text{BOMD}}/10 \approx 0.1 fs$).

Coming to the energy drift of the total physical energy, while the origin for BOMD is the *incomplete* orthonormalization of wave functions, for CPMD it is due to the transfer of energy between cold electrons and hot nuclei. Often it can be minimized by employing separate thermostats to electrons as well as the nuclei in CPMD. BOMD can be made as fast as CPMD (or even faster) at the expense of accuracy in energy conservation. However, for the case of some more challenging systems, such as for the cases of waters, CPMD has been found to be approximately $2-4$ times more efficient than pure BOMD considering speed and tolerance of energy convergence together [23].

Although, CPMD works well for systems with large energy gaps, for metallic systems, for which $E_{gap} \rightarrow 0$, the implementation is not straightforward and instead, BOMD is highly recommended. It is found that in a stable and properly converged CPMD run, the deviation of the CP forces is negligible than compared to BO forces.

Gaussian basis sets have the advantage of employing fewer number of basis sets to represent the wave-function and efficient computation of differentiation integration in real space. However, it suffers from other limitation, such as inclusion of Pulay forces [52] (depends on ionic positions), periodicity, etc. For that plane wave basis sets are generally preferred for their intrinsic periodicity and fast computation in Fourier space [23].

On the other hand, non-self-consistency in numerical calculation of effective one-particle Hamiltonian leads to *non-self-consistency forces*. Since CPMD does not require an explicit self-consistency during time evolution of the system, there is no non-self consistent forces for it. In BOMD, there is always a non-zero contribution due to non-self-consistency, which is not known a priori. Pulay force [52] vanishes exactly for fixed number of plane wave basis sets (origin less). However, if the number does not remain constant, e.g., in NPT simulations, this argument does not hold good. There is no *basis set superposition error* (BSSE) [53–55], if fixed number of basis sets and box-size are used for plane waves.

Recently, a smart algorithm known as QUICKSTEP [56] based on dual basis sets (Gaussian to represent wave-functions and e.g. the Kohn-Sham matrix, and plane wave to represent the electronic density) has been proposed and implemented in the software package CP2K [57]. It has the advantage of employing fewer basis functions per atom as compared to plane wave representations, and sparse representation of Kohn-Sham and density matrices allowing linear scaling methods to perform the density matrix optimization. In short, it allows the advantages of both the types of basis sets. However, in our works, which involves studies of solvation in liquid waters, we have employed the basic CPMD methodologies.

2.3 Density Functional Theory

Density Functional Theory (DFT) gives a viable way to numerically solve the many body time independent ground state problem in a cost efficient manner. It is based on two papers by Hohenberg, Kohn and Sham [16, 17]. The former [16] has given two theorems, now known as HK-theorems, that theoretically laid the foundation of this formalism,

while latter showed how properties of the homogeneous gas can be utilized in theoretical studies of inhomogeneous system of interacting electrons, with hydrogen-like orbitals, based on the HK-theorems, discussed below.

Theorem 1. *The external potential, $V_{ext}(\vec{r})$ is uniquely determined by the electron density $n_0(\vec{r})$.*

Use of electron density instead of wave-function reduces the many body problem from $3N_e \rightarrow 3$, where N_e is the number of electronic degrees of freedom, which uniquely defines an external potential. Thus, except for degenerate cases, the potential, in turn, uniquely determines the ground state wave-function, and therefore, all the other observables of the system (e.g., kinetic energy) are uniquely determined by $V_{\text{ext}}(\vec{r})$. In short, $n(\vec{r}) \rightarrow V_{\text{ext}}(\vec{r}) \rightarrow \psi_0 \rightarrow E_0$.

Theorem 2. *The ground-state energy can be obtained variationally: the density that minimizes the total energy is the exact ground-state density [16].*

Since, ψ_0 is a functional of $n_0(\vec{r})$, so is the kinetic and interaction energies of the many body system and hence the energy functional

$$F\left[n(\vec{r})\right] = \left\langle \psi_0 | T + V | \psi_0 \right\rangle, \tag{2.21}$$

is universal, independent of number of particles (N) and external potential $V_{\text{ext}}(\vec{r})$, such that, the energy functional, for a given potential $V_{\text{ext}}(\vec{r})$, becomes,

$$\begin{aligned} E[n] &= T[n] + E_{\text{ee}}[n] + \int V_{\text{ext}}(\vec{r})\, n(\vec{r}) \\ &= F[n] + \int V_{\text{ext}}(\vec{r})\, n(\vec{r}). \end{aligned} \tag{2.22}$$

This functional takes minimum value for the exact correct ground state density, and hence the ground state can be obtained by minimizing it, if $F[n]$ were known:

$$E_0 = E^{\text{DFT}}[n_0] = \min_{\psi} \left\langle \psi | H_e | \psi \right\rangle = \min_{\rho} \left\langle \psi[\rho] | H_e[\rho] | \psi[\rho] \right\rangle = \min_{\rho} E^{\text{DFT}}[n_0], \tag{2.23}$$

where ground state configuration is reached for $n = n_0$. The terms of the many body energy functional that do not allow to solve the problem exactly are (a) Electron-electron interaction (E_{ee}) and (b) Electron kinetic energy term (T_e). Using *Thomas-Fermi approximation*[58] the former is approximated by the so called *Hartree energy*[59],

$$E_{ee} \approx E_H\left[n(\vec{r})\right] = \frac{1}{2} \iint d\vec{r}\; d\vec{r}\,' \frac{n(\vec{r})\, n\left(\vec{r}\,'\right)}{|\vec{r} - \vec{r}\,'|} \tag{2.24}$$

which is nothing but the classical electrostatic interaction energy between the electron densities $n(\vec{r})$ and $n\left(\vec{r}'\right)$. The electron kinetic energy term (T_e) poses more of a concern involving a $\vec{\nabla}^2$-term, and at this point we have make a crucial approximation of DFT, namely,

$$n(\vec{r}) \;=\; \sum_{i=1}^{N_{\rm occ}} f_i \phi_i(\vec{r}) \phi_i^*(\vec{r}), \tag{2.25}$$

where ϕ_i are fictitious single-particle wave-functions, known as Kohn-Sham (KS) orbitals [17], $N_{\rm occ}$ being the number of occupied orbitals with occupation number f_i for state i, which are related to the number of electrons (N_e) by the following relation

$$\sum_{i=1}^{N_{\rm occ}} f_i \;=\; N_e, \tag{2.26}$$

with which the T_e term is approximated as,

$$T_e \approx -\frac{1}{2} \sum_{i=1}^{N_e} \int \phi_i^*(\vec{r}) \vec{\nabla}^2 \phi_i(\vec{r}) \, d\vec{r} \;=\; T_s\left[\{\phi_i\left[n(\vec{r})\right]\}\right]. \tag{2.27}$$

In essence, the original many particle interacting problem is mapped into a non-interacting single-particle problem with the same electron density. Hohenberg-Kohn theorems demands that this mapping is unique. In fact, this is a single-particle mean-field approximation to the many body inhomogeneous interacting problem, and consequently all the many-body correlation effects are not taken into account. However, Hohenberg-Kohn theorems predicts that the neglected correlation effects are also functional of electron density, known as the *Exchange and Correlation* (XC) functional [16, 17, 59]. With above sets of simplifications, the KS-energy functional becomes,

$$E^{\rm KS}[\{\phi_i\}] \;=\; T_s[\{\phi_i\}] + \int V_{\rm ext}(\vec{r}) n(\vec{r}) {\rm d}\vec{r} + \frac{1}{2} \int V_{\rm H}(\vec{r}) n(\vec{r}) {\rm d}\vec{r} + E_{\rm xc}[n], \tag{2.28}$$

where,

$$E_{\rm XC} \;=\; \left(T[n(\vec{r})] - T_s\left[\{\phi_i\left[n(\vec{r})\right]\}\right]\right) + \left(E_{ee}[n(\vec{r})] - E_H[n(\vec{r})]\right) \tag{2.29}$$

is the XC energy, a unknown to the problem. In order to calculate the ground state of the system, we need to minimize Eq. (2.28) w.r.t. the electron density. This yields the so

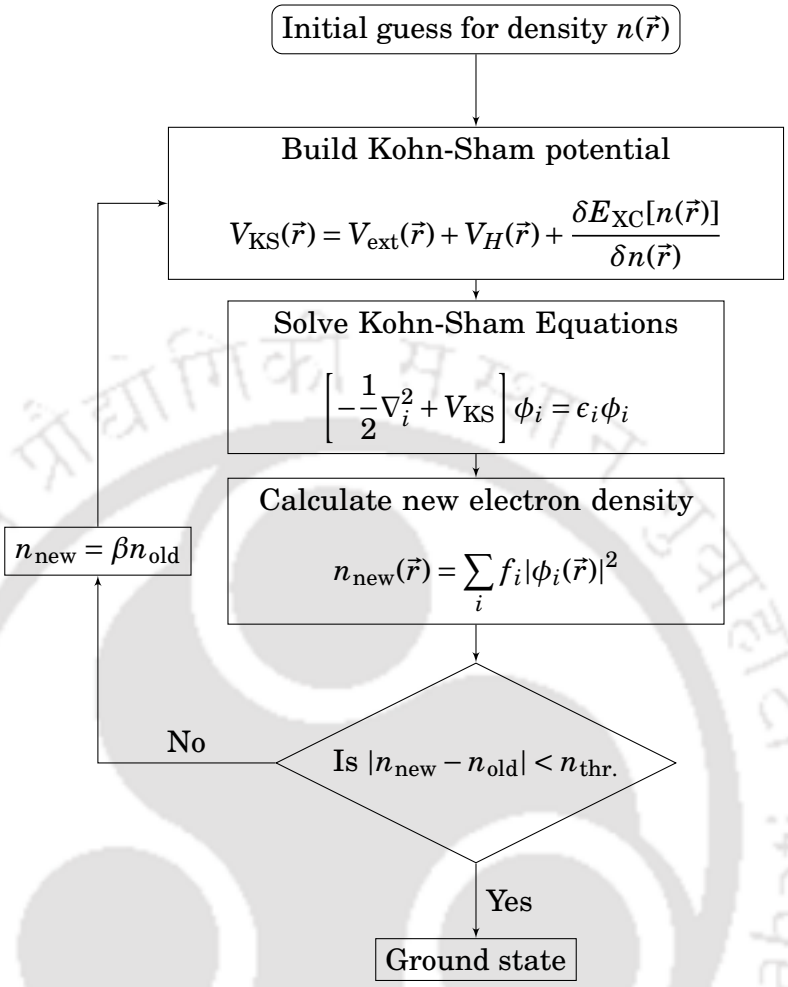

Figure 2.4: Basic algorithm of DFT.

called KS equations:

$$\left[-\frac{1}{2}\vec{\nabla}^2 + V_{\mathrm{ext}}(\vec{r}) + V_{\mathrm{H}}(\vec{r}) + \frac{\delta E_{\mathrm{xc}}[n]}{\delta n(\vec{r})}\right]\phi_i(\vec{r}) = \sum_j \Lambda_{ij}\phi_j(\vec{r}) \tag{2.30a}$$

$$\Rightarrow \left[-\frac{1}{2}\vec{\nabla}^2 + V^{\mathrm{KS}}(\vec{r})\right]\phi_i(\vec{r}) = \sum_j \Lambda_{ij}\phi_j(\vec{r}) \tag{2.30b}$$

$$\Rightarrow \left[\hat{T}_{\mathrm{s}} + \hat{V}_{\mathrm{eff}}\right]\phi_i(\vec{r}) = \sum_j \Lambda_{ij}\phi_j(\vec{r}) \tag{2.30c}$$

$$H_e^{\mathrm{KS}}\phi_i(\vec{r}) = \epsilon_i \phi_i(\vec{r}), \tag{2.30d}$$

where $\{\epsilon_i\}$ are known as the Kohn-Sham eigenvalues. V_{eff} depends on the density and indirectly on the orbitals. In practice, Kohn-Sham system of equations are solved self-consistently, as shown in the Fig.(2.4).

Exchange–Correlation Functional

In principle, the DFT yields exact results provided the XC term is known. However, the exact form of it is not known, except for uniform electron gas. Different approximated forms are generally used that has to be chosen sensitively depending on the systems to be studied [23, 36, 43, 59]. XC-term can be broken up into exchange (E_X) and correlation (E_C) terms [59]:

$$E_{\mathrm{XC}} = \frac{1}{2}\iint \frac{n(\vec{r})n_{\mathrm{XC}}\left(\vec{r},\vec{r}'\right)}{|\vec{r}-\vec{r}'|}\,d\vec{r}\,d\vec{r}' = E_X\left[n(\vec{r})\right]+E_C\left[n(\vec{r})\right], \tag{2.31}$$

where,

$$n_{\mathrm{XC}}\left(\vec{r},\vec{r}'\right) = n_{\mathrm{X}}\left(\vec{r},\vec{r}'\right)+n_{\mathrm{C}}\left(\vec{r},\vec{r}'\right) \tag{2.32}$$

is the called the XC hole. More specifically, $n_{\mathrm{X}}\left(\vec{r},\vec{r}'\right)$ is due to the Pauli repulsion (antisymmetry of the wave-functions) omitted in the Hartree term (E_H) that causes a lowering of the energy for fermionic systems. This term can be calculated exactly using Hartree-Fock exchange energy, given by

$$E_X\left[n(\vec{r})\right] = -\frac{1}{2}\sum_{i,j}\int d\vec{r}\int d\vec{r}'\,\frac{\phi_i^*(\vec{r})\phi_j^*\left(\vec{r}'\right)\phi_i(\vec{r})\phi_j\left(\vec{r}'\right)}{|\vec{r}-\vec{r}'|}, \tag{2.33}$$

but comes under much heavier computational overhead due to its non-local nature. On the other hand, the correlation term E_C comes basically from the repulsion between the electrons having opposite spins further lowering the electronic energy. The exact form of E_C is not known. Under the so called local density approximation (LDA) [60],

$$E_{\mathrm{XC}}^{\mathrm{LDA}} = E_X^{\mathrm{LDA}}[n]+E_C^{\mathrm{LDA}}[n] = \int d\vec{r}\,n(\vec{r})\epsilon_{\mathrm{xc}}(n), \tag{2.34}$$

where the expression for exchange term is simple and may be obtained from the homogeneous gas system,

$$E_x^{\mathrm{LDA}}[n] = C\int n^{4/3}(\mathrm{r})\mathrm{dr}, \tag{2.35}$$

where C is a constant. There are several expressions for the correlation energy, $E_c^{\mathrm{LDA}}[n]$, which have been found by fitting to the results of accurate quantum Monte Carlo (QMC) of a uniform electron gas. Under LDA, the XC energy functional is purely local and homogeneous and contributions arising from any sort of inhomogeneity of the electrons are neglected. Improvement of LDA approximation is achieved by including the density

gradient $\vec{\nabla} n(\vec{r})$ and density itself to the XC functionals, known as generalized gradient approximation (GGA) which is often called a semi-local functional [59, 60],

$$E_{xc}^{\mathrm{GGA}} = \int n(\vec{r}) \epsilon_{xc}^{\mathrm{GGA}} \left[n(\vec{r}), \vec{\nabla} n(\vec{r}) \right] \mathrm{d}\vec{r} \tag{2.36}$$

Most of the GGA functionals have been constructed as the correction added to the LDA term. Examples of such functionals are PBE [61], BLYP [62, 63], etc. Although GGA functionals improve considerably over LDA, still may not be very accurate, one reason being the inexact qualitative behavior of the exchange potential. Meta-GGA functionals try to improve accuracy by incorporating the Laplacian term, $\vec{\nabla}^2 \mathrm{n}(\vec{r})$ into the GGA approximation. However, the most improved results have been obtained by introducing the so called Hybrid functionals (eg., B3LYP, PBE1PBE, etc.), which includes fraction of the exact HF exchange energy. Incorporating such functionals has been computationally very demanding and very rarely employed in AIMD simulations.

Pseudo-potentials

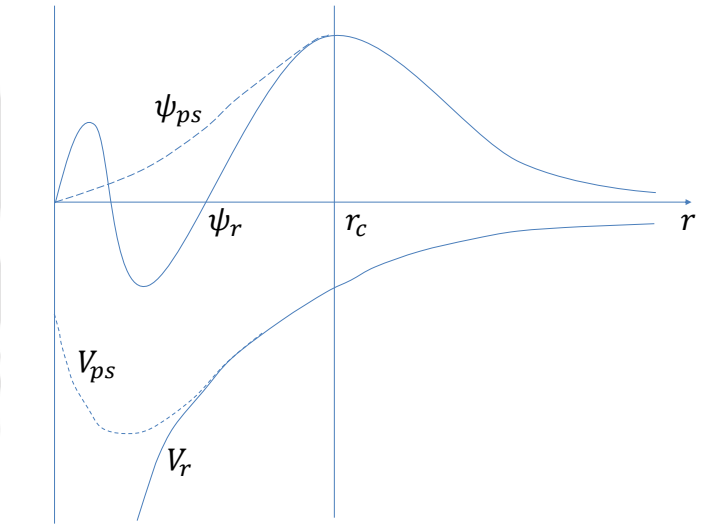

Figure 2.5: Schematic diagram of the relationship between all-electron and pseudo- potentials and wave-functions. r_c is the cut-off radius beyond which real and pseudo components must match.

Since most of the physical and chemical properties of an atom are determined by the valence electrons only, the computational overhead in a DFT calculation can be greatly reduced by considering only the valence electrons explicitly in calculation. The potential of the core is replaced by some effective potential, known as pseudo-potential, which

essentially reduces the all-electron problem to that of an effective ionic core and the valence electrons. In other words, the core states are eliminated and replaced by smooth functions, thereby reducing the number of plane waves required to represent the wave-function. The pseudo and all-electron wave-functions has to be identical beyond the core radius r_c, shown in Fig. 2.5.

There are two common types of pseudo-potentials used in modern plane-wave electronic structure codes: (1) Norm-conserving [64], and (2) Ultra-soft (USP) [65]. The main requirement of the norm-conserving pseudo-potentials is that the pseudo- and all-electron wave-functions have equal norms inside the cutoff distance r_c. This type of pseudo-potentials was first developed by Kleinman and Bylander [66], that paved the way to accurately calculate of solid state properties. In 1990, Vanderbilt [65] proposed a new scheme for generating much *softer* pseudo-potentials, that allows to use much smaller cutoff by relaxing the norm-conservation constraints with some generalized orthonormality conditions. Such pseudo-potentials are called ultra-soft pseudo-potential.

Having discussed the basic techniques of AIMD an related intricacies, we shall discuss some of the standard analysis tools used in analyzing the MD data that have been employed in the thesis.

2.4 Methods for Analysis

2.4.1 Radial Distribution Function

The radial distribution function (RDF), $g(r)$, is the basic tool for structural analysis of a MD trajectory. It gives the probability of finding an atom at a distance r from another tagged atom, and is calculated as the ratio between local density ($n(r)$) to the global density (n) of the atoms in the system under simulation,

$$g(r) = \frac{n(r)}{n}. \tag{2.37}$$

If there exists N_A atoms of type A, and N_B of type B in a simulation of volume V, the RDF of atoms B w.r.t. type A is given by,

$$g_{BA}(r) = \frac{n_B(r)}{n_B} = \frac{V}{N_B} n_B(r). \tag{2.38}$$

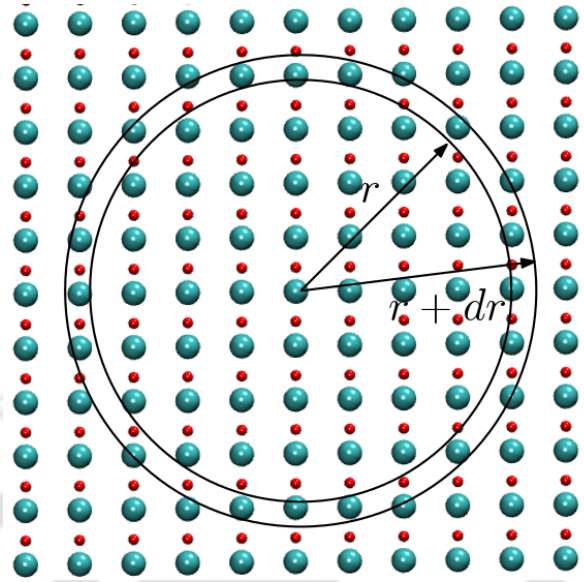

Figure 2.6: Calculation of $g(r)$.

$n(r)$ can be obtained by considering a spherical shell of radius r and thickness Δr around each tagged particle (A) as shown in Fig. 2.6.

$$n_B(r) = \frac{1}{4\pi r^2 \Delta r}\left(\frac{1}{N_A}\sum_{i=1}^{N_A}\delta(r - r_i)\right) \tag{2.39}$$

Inserting Eq. (2.39) into Eq. (2.38), we get the working form of RDF:

$$g_{BA}(r) = \frac{V}{4\pi r^2 \Delta r N_A N_B}\sum_{i=1}^{N_A}\delta(r - r_i), \tag{2.40}$$

with the condition that,

$$\int_0^\infty 4\pi r^2 n g(r) dr = N, \tag{2.41}$$

where N is the total number of atoms of a given type.

The shape of $g(r)$ strongly depends on the type of material and varies considerably from solids to gases (see Fig. 2.7). Gases do not possess any regular structure and hence, the RDFs generally have a single coordination shell that rapidly decays to the normal bulk density of a gas, $g(r) = 1$. For liquids, there exists local structural ordering, but at large values of r, the molecules become independent of each other, and the distribution returns to the bulk density ($g(r) = 1$). That is $g(r) \to 1$ as $r \to \infty$. Also, $g(r) \to 0$ as $r \to 0$ because of the short range repulsion between the atoms. Crystalline solids are dense and ordered and therefore they show sharp peaks of $g(r)$ at low temperature which do not converge to one because of the long range orderings. It looks like delta functions, at low

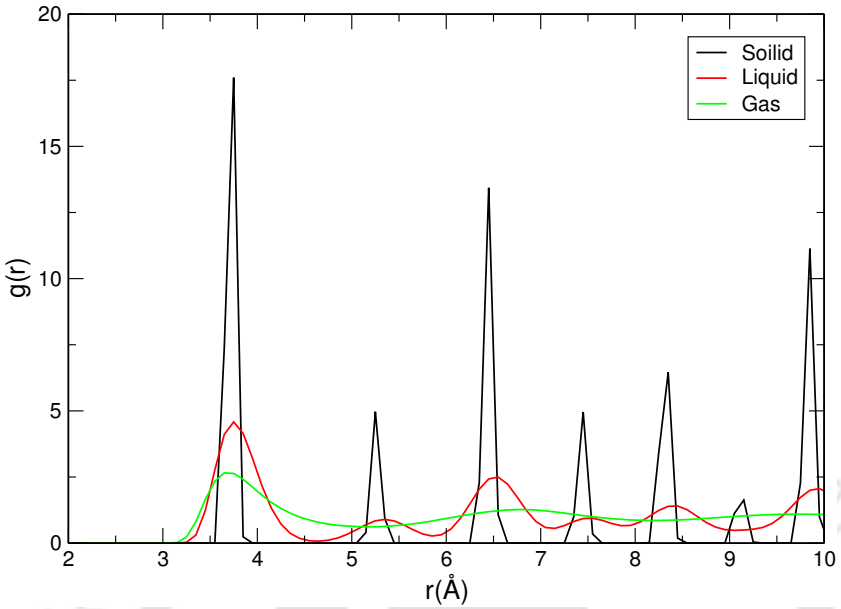

Figure 2.7: Comparison of the typical behavior of RDFs for matter at solid, liquid and gaseous phases. Figures produced for a system of argon atoms simulated with a basic self developed Fortran code.

temperatures, but broadens due to thermal/quantum mechanical vibrational motions. On the other hand, liquids or gases show broader peaks of $g(r)$ because of the inherent disorders in structure [2, 3, 67].

The number of atoms up to a distance r from a tagged atom can be obtained by integrating over $g(r)$,

$$n(r) = 4\pi \int_0^r r^2 n g(r) dr. \tag{2.42}$$

This is popularly known as running coordination number (RCN), and can be used to calculate coordination numbers of an atom or species.

2.4.2 Auto-Correlation Function and Spectroscopy

A time-correlation function measures how the value of some quantity A at time t' depends on some other/same quantity B at time t'' which, for an equilibrium system depends on only the time difference $t = t'' - t'$.

$$C_{AB}(t) = \lim_{T\to 0} \frac{1}{T} \int_0^T B(t+t')A(t')dt' = \langle B(t+t')A(t')\rangle \tag{2.43}$$

For $A = B$ we get the auto-correlation function, eg. velocity auto-correlation function given by,

$$C(t) = \langle v(t+t').v(t') \rangle \tag{2.44}$$

For an equilibrium system the initial value is given by $G(0) = \frac{3k_BT}{m}$ and for long times the initial and final velocity must become completely uncorrelated i.e., $G(t \to \infty) = 0$. The importance of the autocorrelation functions lies in the fact given by the *Wiener-Khintchin's theorem*, which states that the power spectra of a dynamic quantity is equal to the Fourier transform of the corresponding autocorrelation function,

$$P(\omega) = \int_{-\infty}^{\infty} C(t) e^{i\omega t} dt \tag{2.45}$$

The power spectra corresponding to velocity autocorrelation function yields the vibrational density of states of the system. Power spectra could be directly compared with different spectroscopic data depending on the type of autocorrelation function taken into account. For instance, IR spectra may be calculated from the dipole autocorrelation functions, and Raman spectra is obtained by taking molecular polarizibilities into consideration [2, 3, 68, 69].

2.4.3 Hydrogen bond analysis

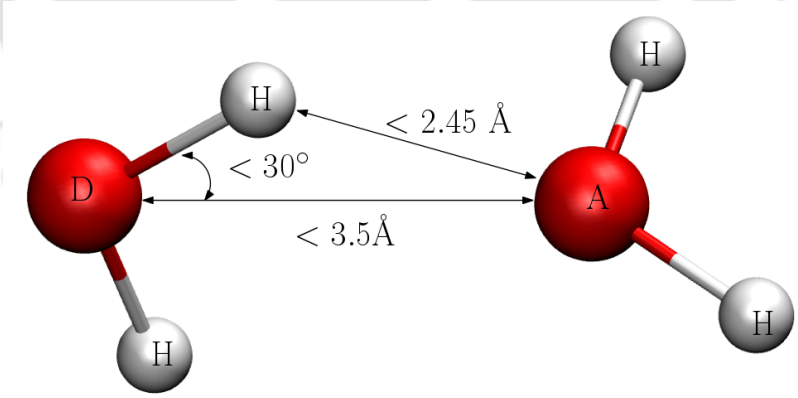

Figure 2.8: Definition of a hydrogen bond

A hydrogen bond between two water molecules is defined in terms of the following criterion [70–76]:

- The donor-acceptor O···O distance is less than 3.5 Å,

- The donor-acceptor H$\cdots$O distance is less than 2.45 Å,
- The Hydrogen-donor-acceptor (H$-$D$-$A) angle is less than 30°.

H-bonds are characterized by H-bond correlation function[70–75, 77] given by,

$$C_{\mathrm{HB}}(t) = \frac{\langle h(0).h(t)\rangle}{\langle h\rangle} \tag{2.46}$$

where $h(t) = h[\vec{r}(t)]$ is known as the hydrogen bond population operator for the instantaneous configuration $\vec{r}(t)$. This operator takes value 1 if there exist H-bond between two tagged atoms, otherwise zero. The average number of hydrogen bond in an equilibrium fluid containing N water molecules is $\frac{N(N-1)}{2}\langle h\rangle$, where $\langle h\rangle$ denotes the average value of $h(t)$. Therefore, $C_{\mathrm{HB}}(t)$ basically signifies the probability that a hydrogen bond is intact at time t, and based on all the three criterion of formation of hydrogen bond between a species. Similarly H-bond correlation function based on distance criterion alone can also be defined,

$$C^{d}_{\mathrm{HB}}(t) = \frac{\langle h(0).h^{d}(t)\rangle}{\langle h\rangle} \tag{2.47}$$

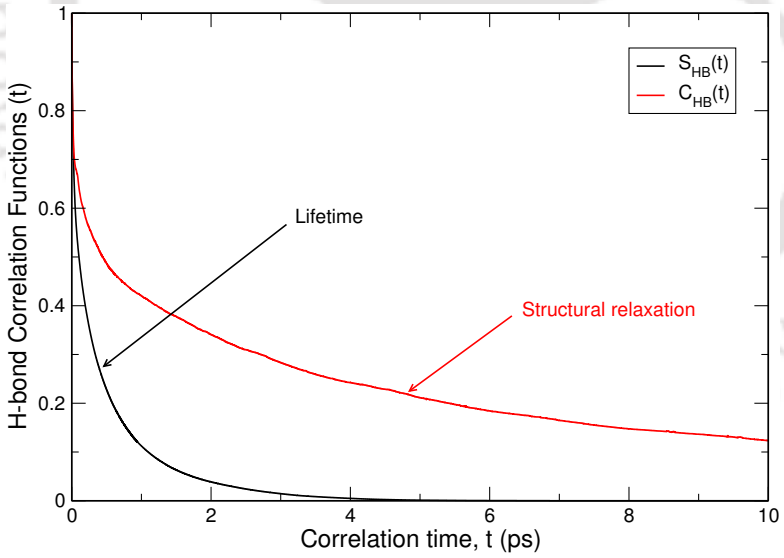

Figure 2.9: Typical behavior of hydrogen bond correlation functions, $S_{\mathrm{HB}}(t)$ and $C_{\mathrm{HB}}(t)$.

The lifetime of hydrogen bonds between a donor-acceptor pair can be estimated by defining two more time correlation functions based on distance and angular criterion.They are given by,

$$S_{\mathrm{HB}}(t) = \frac{\langle h(0).H(t)\rangle}{\langle h\rangle} \tag{2.48}$$

$$S^{d}_{\mathrm{HB}}(t) = \frac{\langle h(0).H^{d}(t)\rangle}{\langle h\rangle} \tag{2.49}$$

where $H(t) = 1$ if the tagged pair of donor-acceptor sites remain continuously hydrogen bonded for a time t, otherwise zero [2, 70, 72]. $S_{\mathrm{HB}}(t)$, known as *continuous* H-bond correlation function, as defined above, is sensitive to the intermediate H-bond breaking, hence provide a qualitative measure of the lifetimes of H-bonds.

2.4.4 Water Orientational Correlation Function

The dynamics of orientational relaxation of H_2O molecules can be studied by using the second order Legendre polynomial (P_2) of vector ($\vec{v}$) correlation function [70, 77–80], given by,

$$C_2(t) = \langle P_2(\hat{v}(0).\hat{v}(t))\rangle \tag{2.50}$$

where, $\hat{v} = \vec{v}/|\vec{v}|$ is the unit vector along $\vec{v}$ (along the OH bond of H_2O) and $P_2(x) = (3x^2 - 1)/2$ is the 2^{nd}-order Legendre polynomial [70, 77–80]. In this form, these results are directly related to the experimentally calculated rotational anisotropy measurements of water molecules [77, 79]. These plots exhibits an initial rapid decay (owing to the librational motions of the H_2O molecules), followed by slower decay that characterize the orientatonal relaxation of the water molecules.

These quantities have been extensively employed in the results discussed in the coming chapters.

BIBLIOGRAPHY

[1] John A Sokolowski and Catherine M Banks. *Principles of modeling and simulation: a multidisciplinary approach*. John Wiley & Sons, 2011.

[2] Michael P Allen and Dominic J Tildesley. *Computer simulation of liquids*. Oxford university press, 2017.

[3] Daan Frenkel and Berend Smit. *Understanding molecular simulation: From algorithms to applications*, volume 1. Elsevier (formerly published by Academic Press), 2002.

[4] Dieter W Heermann. Computer-simulation methods. In *Computer Simulation Methods in Theoretical Physics*, pages 8–12. Springer, 1990.

[5] DC Rapoport. *The Art of Molecular Dynamics Simulations*. New York: Cambridge University Press, 1997.

[6] Kurt Binder and Giovanni Ciccotti. *Monte Carlo and molecular dynamics of condensed matter systems*, volume 49. Compositori, 1996.

[7] R.K. Pathria and P.D. Beale. *Statistical Mechanics*. Elsevier Science, 1996.

[8] BJ Alder and TEf Wainwright. Phase transition for a hard sphere system. *J. Chem. Phys.*, 27(5):1208–1209, 1957.

[9] Berni J Alder and T E Wainwright. Studies in molecular dynamics. i. general method. *J. Chem. Phys.*, 31(2):459–466, 1959.

[10] Bruce J Berne, G Cicootti, and David F Coker. Classical and quantum dynamics in condensed phase simulations. 1998.

[11] A Rahman. Correlations in the motion of atoms in liquid argon. *Phys. Rev.*, 136(2A):A405, 1964.

[12] Frank H Stillinger and Aneesur Rahman. Improved simulation of liquid water by molecular dynamics. *J. Chem. Phys.*, 60(4):1545–1557, 1974.

[13] Frank H Stillinger and Aneesur Rahman. Molecular dynamics study of liquid water under high compression. *J. Chem. Phys.*, 61(12):4973–4980, 1974.

[14] Roberto Car and Michele Parrinello. Unified approach for molecular dynamics and density-functional theory. *Phys. Rev. Lett.*, 55(22):2471, 1985.

[15] Dominik Marx and Jurg Hutter. *Modern methods and algorithms of quantum chemistry*. John von Neumann Institute for Computing (NIC), 2000.

[16] Pierre Hohenberg and Walter Kohn. Inhomogeneous electron gas. *Phys. Rev.*, 136(3B):B864, 1964.

[17] Walter Kohn and Lu Jeu Sham. Self-consistent equations including exchange and correlation effects. *Phys. Rev.*, 140(4A):A1133, 1965.

[18] CG Gray and KE Gubbins. *Fundamentals (Theory of Molecular Fluids)*, volume 1. Oxford: Clarendon,

1984.

[19] Jürg Hutter. Lecture notes introduction to ab initio molecular dynamics, 2002.

[20] Loup Verlet. Computer" experiments" on classical fluids. i. thermodynamical properties of lennard-jones molecules. *Phys. Rev.*, 159(1):98, 1967.

[21] Dahlia K Remler and Paul A Madden. Molecular dynamics without effective potentials via the car-parrinello approach. *Mol. Phys.*, 70(6):921–966, 1990.

[22] Mike C Payne, Michael P Teter, Douglas C Allan, TA Arias, and JD Joannopoulos. Iterative minimization techniques for ab initio total-energy calculations: molecular dynamics and conjugate gradients. *Rev. Mod. Phys.*, 64(4):1045, 1992.

[23] Dominik Marx and Jürg Hutter. *Ab initio molecular dynamics: basic theory and advanced methods*. Cambridge University Press, 2009.

[24] R Car and M Parrinello. The unified approach to density functional and molecular dynamics in real space. *Solid state communications*, 62(6):403–405, 1987.

[25] Noam Agmon, Huib J. Bakker, R. Kramer Campen, Richard H. Henchman, Peter Pohl, Sylvie Roke, Martin Thämer, and Ali Hassanali. Protons and Hydroxide Ions in Aqueous Systems. *Chem. Rev.*, 116(13):7642–7672, 2016.

[26] Ali A Hassanali, Jérôme Cuny, Vincenzo Verdolino, and Michele Parrinello. Aqueous solutions: state of the art in ab initio molecular dynamics. *Philos. Trans. R. Soc.*, 372(2011):20120482–20120482, 2014.

[27] Barbara Kirchner, Philipp J di Dio, and Jürg Hutter. Real-World Predictions from Ab Initio Molecular Dynamics Simulations. In Barbara Kirchner and Jadran Vrabec, editors, *Multiscale Mol. Methods Appl. Chem.*, pages 109–153. Springer Berlin Heidelberg, Berlin, Heidelberg, 2012.

[28] Mark E. Tuckerman, Amalendu Chandra, and Dominik Marx. Structure and dynamics of OH - (aq). *Acc. Chem. Res.*, 39(2):151–158, 2006.

[29] Dominik Marx. Proton transfer 200 years after Von Grotthuss: Insights from ab initio simulations. *ChemPhysChem*, 7(9):1849–1870, 2006.

[30] Dominik Marx, Amalendu Chandra, and Mark E Tuckerman. Aqueous basic solutions: hydroxide solvation, structural diffusion, and comparison to the hydrated proton. *Chem. Rev.*, 110(4):2174–2216, 2010.

[31] M E Tuckerman. Ab initio molecular dynamics: basic concepts, current trends and novel applications. *J. Phys. Condens. Matter.*, 14(50):R1297–R1355, 2002.

[32] Mauro Ferrario, Giovanni Ciccotti, and Kurt Binder. *Computer simulations in condensed matter: from materials to chemical biology*, volume 1. Springer, 2007.

[33] Christopher J Mundy and I-Feng W Kuo. First-principles approaches to the structure and reactivity of atmospherically relevant aqueous interfaces. *Chem. Rev.*, 106(4):1282–1304, 2006.

[34] John S. Tse. Ab Initio Molecular Dynamics with Density Functional Theory. *Annu. Rev. Phys. Chem.*, 53(1):249–290, 2002.

[35] Jun John Sakurai and Jim Napolitano. *Modern quantum mechanics*. Cambridge University Press, 2017.

[36] Richard M Martin. *Electronic structure: basic theory and practical methods*. Cambridge university

press, 2004.

[37] Max Born and Robert Oppenheimer. Zur quantentheorie der molekeln. *Ann. Phys.*, 389(20):457–484, 1927.

[38] W Kolos. W. kolos, adv. quantum chem. 5, 99 (1970). *Adv. Quantum Chem.*, 5:99, 1970.

[39] Werner Kutzelnigg. The adiabatic approximation i. the physical background of the born-handy ansatz. *Mol. Phys.*, 90(6):909–916, 1997.

[40] Donald Leo Thompson. *Modern methods for multidimensional dynamics computations in chemistry*. World Scientific, 1998.

[41] Attila Szabo and Neil S Ostlund. *Modern quantum chemistry: introduction to advanced electronic structure theory*. Courier Corporation, 2012.

[42] Roy McWeeny. *Methods of molecular quantum mechanics*. Academic press, 1992.

[43] R G Yang and W Yang. *Density Functional Theory of Atoms and Molecules*. Oxford University Press, Oxford, 1989.

[44] Reiner M Dreizler and Eberhard KU Gross. *Density–Functional Theory*. Springer, 1990.

[45] Herbert Goldstein, Charles P Poole, and John L Safko. *Classical Mechanics: Pearson New International Edition*. Pearson Higher Ed, 2014.

[46] G Pastore, E Smargiassi, and F Buda. Theory of ab initio molecular-dynamics calculations. *Phys. Rev. A*, 44(10):6334, 1991.

[47] Folkmar A Bornemann and Christof Schütte. Adaptive accuracy control for car-parrinello simulations. *Nume.Math.*, 83(2):179–186, 1999.

[48] I-Feng W Kuo, Christopher J Mundy, Matthew J McGrath, J Ilja Siepmann, Joost VandeVondele, Michiel Sprik, Jürg Hutter, Bin Chen, Michael L Klein, Fawzi Mohamed, et al. Liquid water from first principles: investigation of different sampling approaches. *J. Phys. Chem. B*, 108(34):12990–12998, 2004.

[49] H Hellmann. Zur rolle der kinetischen elektronenenergie für die zwischenatomaren kräfte. *Zeitschrift für Physik*, 85(3-4):180–190, 1933.

[50] Richard Phillips Feynman. Forces in molecules. *Phys. Rev.*, 56(4):340, 1939.

[51] Ira N Levine, Daryle H Busch, and Harrison Shull. *Quantum chemistry*, volume 5. Prentice Hall Upper Saddle River, NJ, 2000.

[52] Peter Pulay. Ab initio calculation of force constants and equilibrium geometries in polyatomic molecules: I. theory. *Mol. Phys.*, 17(2):197–204, 1969.

[53] Paul Bendt and Alex Zunger. Simultaneous relaxation of nuclear geometries and electric charge densities in electronic structure theories. *Phys. Rev. Lett.*, 50(21):1684, 1983.

[54] M Fähnle, C Elsässer, and H Krimmel. The basic strategy behind the derivation of various ab-initio force formulae. *Phys. Status Solidi B*, 191(1):9–19, 1995.

[55] GP Srivastava and D Weaire. The theory of the cohesive energies of solids. *Adv. Phys.*, 36(4):463–517, 1987.

[56] Joost VandeVondele, Matthias Krack, Fawzi Mohamed, Michele Parrinello, Thomas Chassaing, and Jürg Hutter. Quickstep: Fast and accurate density functional calculations using a mixed gaussian and plane waves approach. *Comput. Phys. Commun.*, 167(2):103–128, 2005.

[57] CP2K. General program to perform molecular dynamics simulations. *CP2k developers group under the terms of the GNU General Public License,http://www.cp2k.org*.

[58] NH March. The thomas-fermi approximation in quantum mechanics. *Adv. Phys.*, 6(21):1–101, 1957.

[59] Thomas D Kühne, Matthias Krack, Fawzi R Mohamed, and Michele Parrinello. Efficient and accurate car-parrinello-like approach to born-oppenheimer molecular dynamics. *Physical review letters*, 98(6):066401, 2007.

[60] Kieron Burke and Lucas O Wagner. Dft in a nutshell. *International Journal of Quantum Chemistry*, 113(2):96–101, 2013.

[61] BHLB Hammer, Lars Bruno Hansen, and Jens Kehlet Nørskov. Improved adsorption energetics within density-functional theory using revised perdew-burke-ernzerhof functionals. *Phys. Rev. B*, 59(11):7413, 1999.

[62] Axel D Becke. Density-functional exchange-energy approximation with correct asymptotic behavior. *Phys. Rev. A*, 38(6):3098, 1988.

[63] Chengteh Lee, Weitao Yang, and Robert G Parr. Development of the colle-salvetti correlation-energy formula into a functional of the electron density. *Phys. Rev. B*, 37(2):785, 1988.

[64] DR Hamann, M Schlüter, and C Chiang. Norm-conserving pseudopotentials. *Phys. Rev. Lett.*, 43(20):1494, 1979.

[65] David Vanderbilt. Soft self-consistent pseudopotentials in a generalized eigenvalue formalism. *Phys. Rev. B*, 41:7892–7895, Apr 1990.

[66] L Kleinman. L. kleinman and dm bylander, phys. rev. lett. 48, 1425 (1982). *Phys. Rev. Lett.*, 48:1425, 1982.

[67] Takeshi Egami and Simon JL Billinge. *Underneath the Bragg peaks: structural analysis of complex materials*, volume 16. Elsevier, 2003.

[68] Martin Thomas, Martin Brehm, Reinhold Fligg, Peter Vöhringer, and Barbara Kirchner. Computing vibrational spectra from ab initio molecular dynamics. *Physical Chemistry Chemical Physics*, 15(18):6608–6622, 2013.

[69] Martin Brehm and Barbara Kirchner. Travis-a free analyzer and visualizer for monte carlo and molecular dynamics trajectories. *J. Chem. Inf. Model.*, 51(3):2007–2023, 2011.

[70] Alenka Luzar and David Chandler. Effect of environment on hydrogen bond dynamics in liquid water. *Phys. Rev. Lett.*, 76(6):928, 1996.

[71] Alenka Luzar. Resolving the hydrogen bond dynamics conundrum. *J. Chem. Phys.*, 113(23):10663–10675, 2000.

[72] Amalendu Chandra. Effects of ion atmosphere on hydrogen-bond dynamics in aqueous electrolyte solutions. *Phys Rev Lett*, 85(4):768, 2000.

[73] P Padma Kumar, Andrey G Kalinichev, and R James Kirkpatrick. Hydrogen-bonding structure and dynamics of aqueous carbonate species from car- parrinello molecular dynamics simulations. *J. Phys. Chem. B*, 113(3):794–802, 2008.

[74] Félix S Csajka and David Chandler. Transition pathways in a many-body system: application to hydrogen-bond breaking in water. *J. Chem. Phys.*, 109(3):1125–1133, 1998.

[75] Bhabani S Mallik, A Semparithi, and Amalendu Chandra. Vibrational spectral diffusion and hydrogen

bond dynamics in heavy water from first principles. *J.Phys. Chem. A*, 112(23):5104–5112, 2008.

[76] P Padma Kumar, Andrey G Kalinichev, and R James Kirkpatrick. Dissociation of carbonic acid: Gas phase energetics and mechanism from ab initio metadynamics simulations. *The Journal of chemical physics*, 126(20):204315, 2007.

[77] Ashu Choudhary and Amalendu Chandra. Anisotropic structure and dynamics of the solvation shell of a benzene solute in liquid water from ab initio molecular dynamics simulations. *Phys. Chem. Chem. Phys.*, 18(8):6132–6145, 2016.

[78] Zhonghua Ma and Mark E Tuckerman. On the connection between proton transport, structural diffusion, and reorientation of the hydrated hydroxide ion as a function of temperature. *Chem. Phys. Lett.*, 511(4):177–182, 2011.

[79] Snehasis Chowdhuri and Amalendu Chandra. Molecular dynamics simulations of aqueous nacl and kcl solutions: Effects of ion concentration on the single-particle, pair, and collective dynamical properties of ions and water molecules. *J. Chem. Phys.*, 115(8):3732–3741, 2001.

[80] Damien Laage and James T Hynes. A molecular jump mechanism of water reorientation. *Science*, 311(5762):832–835, 2006.

CHAPTER 3

AIMD STUDIES OF WATERBORNE SE–VI SPECIES

3.1 Introduction

Selenium exists in aqueous environment mostly in Se–VI and Se–IV valence states. The parent form of the former is known as selenic acid (H_2SeO_4), which is a very strong acid with the experimentally reported pK_{a1} value of −3.0 [1]. Its mono-deprotonated form namely $HSeO_4^-$ is also a strong acid with $pK_{a2} = 1.70$ [1].

$$H_2SeO_4 \xrightarrow[-3.0]{pK_{a1}} HSeO_4^- \xrightarrow[1.70]{pK_{a2}} SeO_4^{2-} \tag{3.1}$$

Thus, SeO_4^{2-} is expected to be stable at neutral and low acidic conditions. The structure and hydrogen bonding of hydrated $HSeO_4^-$ and SeO_4^{2-} have been recently probed experimentally employing large angle X-ray scattering (LAXS), EXAFS and double difference infrared (DDIR) spectroscopy by Eklund and Persson [1]. An *ab initio* quantum mechanical charge field molecular dynamics (QMCF-MD) simulation study had been conducted by Sakwarathorn et al. [2] to characterize the structure and spectroscopic natures of solvated SeO_4^{2-} species.

In this work, a detailed *ab initio* Density Functional Theory (DFT) [3, 4] based Car-Parrinello Molecular Dynamics (CPMD) [5] simulation has been carried out on selenic

An article based on this chapter is published in *Phys. Chem. Chem. Phys*, vol. **18**, year 2016, pages 14561-14568; title:"Ab initio molecular dynamics investigation of structural, dynamic and spectroscopic aspects of Se–VI species in the aqueous environment"; authors Sangkha Borah and P. Padma Kumar. Selected contents are reproduced with permission ©Royal Society of Chemistry 2016.

acid (H_2SeO_4) in the aqueous environment. Fresh microscopic insights on the hydration structure, nature of hydrogen-bonding (H-bonding) and vibrational properties of aqueous selenates have been presented comprehensively.

3.2 Methods

The *ab-initio* simulations employed in this work follows the Car-Parrinello molecular dynamics (CPMD) scheme [5] as implemented in version 3.15.3 of the CPMD software package [6, 7]. From a pre-equilibrated system of 64 H_2O molecules in a cubic box of length 12.42 Å (at a density of ~ 1 g/cc), a cluster of four water molecules is removed to plant an H_2SeO_4 molecule. The resulting system consisting of one H_2SeO_4 molecule solvated by 60 H_2O molecules in a 12.42 Å box (having a density of ~ 1.06 g/cc, close to the experimental [8] density of ~ 1.09 g/cc) is equilibrated at 315 K for a few nano-seconds with classical force-field models in NVT ensemble. The final configuration is further equilibrated with CPMD for over 50 pico-seconds, before production runs of 50 pico-seconds are carried out. All CPMD simulations are performed with gradient-corrected, norm-conserving Becke [9], Lee-Yang-Parr [10] (BLYP) pseudo-potentials, and Kohn-Sham orbitals are expanded using plane wave basis at a cut-off of 85 Ry [4]. Nose-Hoover thermostats [11, 12] are used to control the temperature of the ions at 315 K. At a fictitious mass of 600 au, the electronic subsystem is thermostated at a total classical kinetic energy of 0.03 au [13]. CPMD simulations of pure water system, consisting of 64 H_2O molecules in 12.42 Å box, are also performed under similar settings to make useful comparison. A time step of 0.1 fs is used for integration, and the trajectory is printed at every 5 MD steps. Trajectories collected over 50 ps of production runs are subjected to detailed analysis for local hydration structure, dynamics and nature of H-bonding. Further normal-mode analysis of $HSeO_4^-$ and SeO_4^{2-} molecules, which turn-out to be the predominant species in neutral aqueous environment, is carried out in gas-phase using Martyna-Tuckerman's Poisson solver scheme [14] as implemented in CPMD software.

For the ease of description, we shall use the label O_{Se} for the oxygens of the Se-species not bonded to hydrogen (H), and $O_{Se,H}$ for the oxygens of selenate species bonded to hydrogen, to distinguish them from water oxygens (O).

3.3 Results and Discussions

3.3.1 Proton transfer

Being a strong acid with $pK_{a1} = -3.0$, the H_2SeO_4 molecule is found to give away one of its hydrogens very quickly to the surrounding water, within a few pico-seconds of simulation run (during the equilibration phase itself) forming $HSeO_4^-$ and never reformed during the entire simulation run. Although $HSeO_4^-$ further deprotonates to SeO_4^{2-}, with the creation of two hydronium, H_3O^+ ions, out of 60 H_2O molecules, during the simulation, instances of reformation of $HSeO_4^-$, lasting for few pico-seconds are noted. This owes to the highly acidic water surrounding it. The deprotonation events,

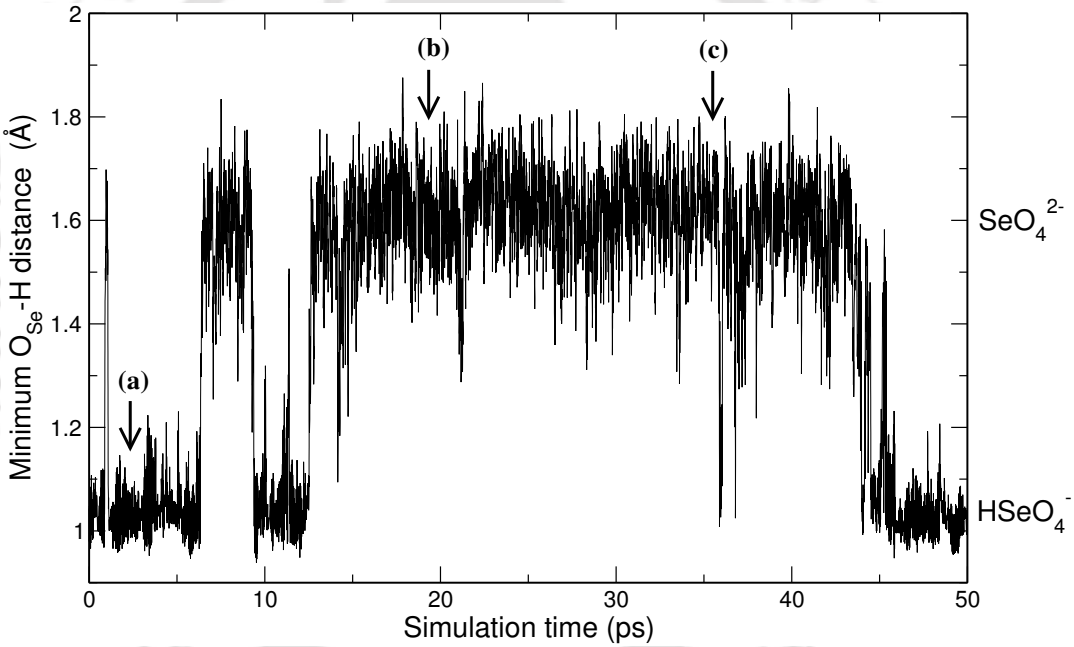

Figure 3.1: Time evolution of the minimum $O_{Se}-H$ distance during the CPMD simulation at 315 K, depicting the proton transfer events. The minimum $O_{Se}-H$ distance less than 1.3 Å represents $HSeO_4^-$ and the distance above 1.4 Å represents SeO_4^{2-} species.

$$HSeO_4^- + H_2O \rightleftharpoons SeO_4^{2-} + H_3O^+ \tag{3.2}$$

during the course of the MD simulation can be conveniently monitored through the shortest $O_{Se}\cdots H$ distance in the system (out of all the possible, 4 O_{Se} × 122 H = 488 distances, without distinguishing if an H is presently or was earlier associated with the solute species). Shown in Fig. 3.1, the shortest $O_{Se}-H$ distance less than 1.3 Å signals presence of $HSeO_4^-$ and above 1.4 Å attributed to SeO_4^{2-} species, given that H_2SeO_4

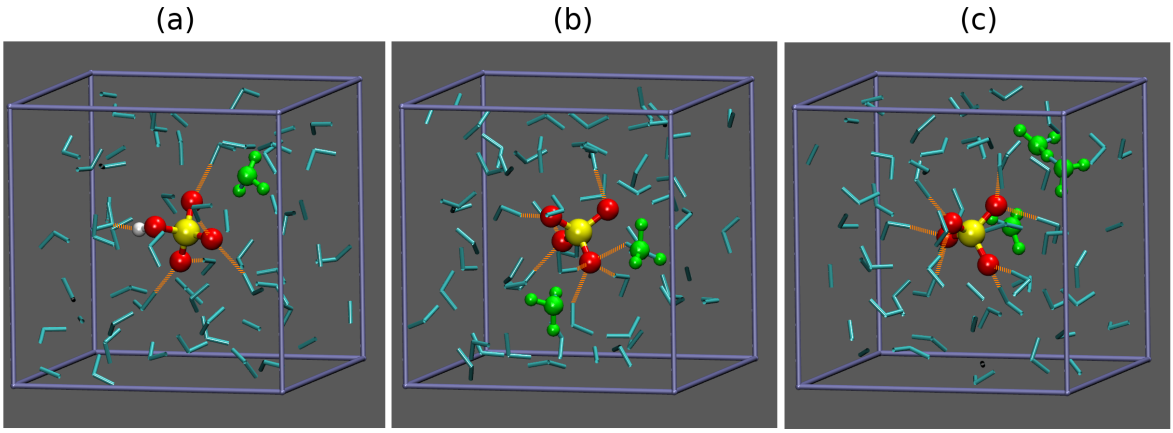

Figure 3.2: Snapshots from CPMD simulation taken at instances shown by arrows in Fig. 3.1. (a) Single deprotonated $HSeO_4^-$ species, (b) and (c) fully deprotonated SeO_4^{2-} system along with the formation of the hydronium (H_3O^+) and Zundel ion ($H_5O_2^+$) (shown in green color balls) during simulation. The instantaneous H-bonds with the central species is shown in brown dotted lines. H_2O molecules are shown as sticks in cyan.

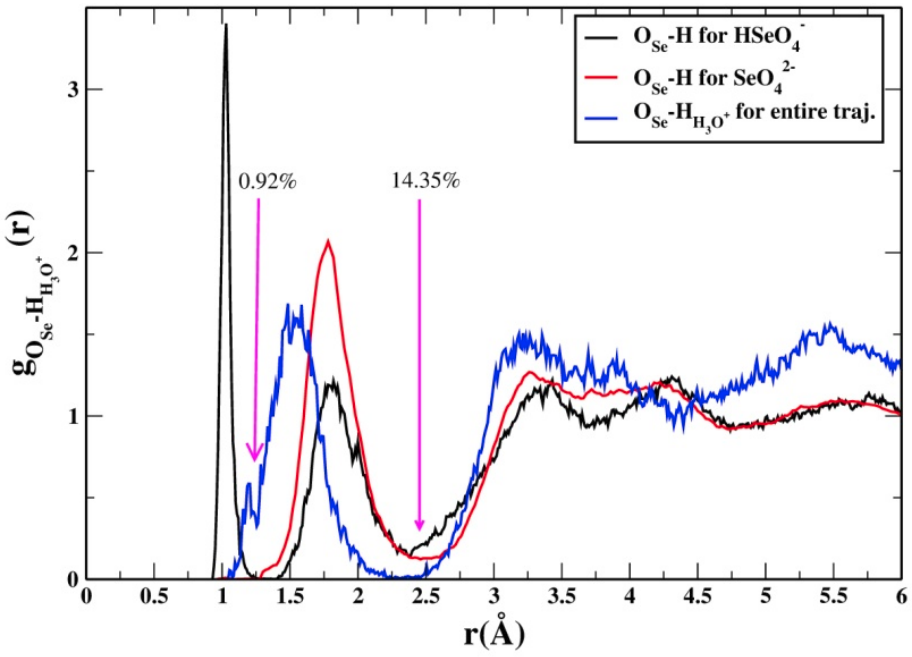

Figure 3.3: Radial distribution function, $g(r)$ of instantaneous H of H_3O^+ ions w.r.t. the O_{Se} atoms, showing the transition states structures, $SeO_4^{2-}\cdots H^+\cdots H_2O$, where the H^+ is within 1.3 Å of the solute and solvent oxygens, exists for about 1% of MD frames across the 50 ps trajectory. It remains in the 1st shell for less than 15% of the entire frames. The RDFs for $O_{Se}-H$ for $HSeO_4^-$ and SeO_4^{2-} extracted from the trajectory for analysis is also shown along-with, for comparison.

species deprotonates during the early equilibration phase and never reappeared during the production phase. Across the 50 ps trajectory the presence of SeO_4^{2-} to $HSeO_4^-$ is estimated to be 69:31. However, exploiting the relation for the dissociation constant, Eq. (3.3) for the above reaction, Eq. (3.2) ,

$$pK_{a2} = -\log\left(\frac{[SeO_4^{2-}]\,[H_3O^+]}{[HSeO_4^-][H_2O]}\right) \tag{3.3}$$

a reversal of the scenario, 36:64, in favour of $HSeO_4^-$ is expected based on the experimental pK_{a2} value of 1.70. It shall be noted that, accurate determination of the dissociation constant would require much longer MD simulations, or use of alternate techniques, such as metadynamics, as demonstrated a few recent studies [15–17].

Fig. 3.2 shows three representative snapshots of the system picked at instances marked by (a), (b) and (c) in Fig. 3.1. Fig. 3.2(a) depicts the $HSeO_4^-$ species co-existing with a hydronium ion (identified by oxygen having 3 hydrogens within 1.3 Å) and is outside of its first hydration shell of the solute. The oxygens and hydrogen of the $HSeO_4^-$ are shown, respectively as red and while balls, and hydroniums as green balls. The instantaneous H-bonds between the water and the selenate are shown in brown dotted lines in Fig. 3.2. Fig. 3.2(b) and Fig. 3.2(c) show two snapshots of the SeO_4^{2-} species, the former displays two hydronium species while the latter has one hydronium as well as a Zundel ion ($H_5O_2^+$). The Zundel ion is an intermediate state of proton transfer between two water molecules, examined in detail in several previous *ab-initio* studies (see the review article by D. Marx [18] and references therein). Several such proton transfer events through Grotthuss mechanism [18, 19] were observed during the time scale of the simulation. Statistical analysis, based on an O···H cutoff distance of 1.3 Å, suggests that approximate transition states structures, $SeO_4^{2-}\cdots H^+\cdots H_2O$, where the H^+ is within 1.3 Å of the solute and solvent oxygens simultaneously, exists for about 1% of MD frames across the 50 ps trajectory. The H_3O^+ ions in the system are located within the first hydration shell for less than 15% frames for both species, thus they reside largely outside of the first hydration shell (see Fig. 3.3). The extended periods of existence of $HSeO_4^-$ and SeO_4^{2-} noted in Fig. 3.1 allow structural characterization of these individual species in the aqueous environment, which is presented bellow.

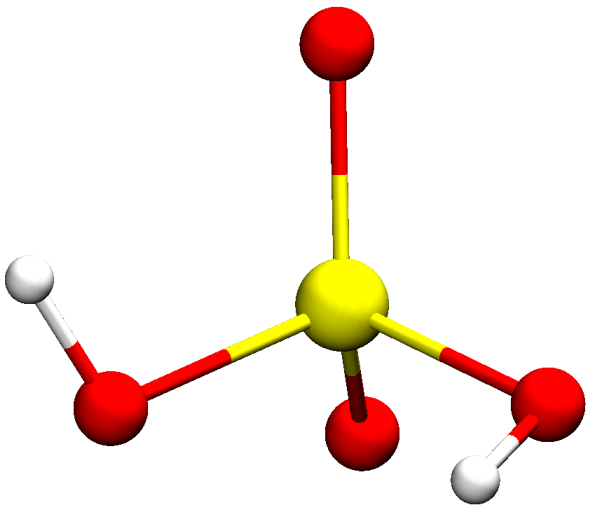

Figure 3.4: The gas-phase geometry optimized structure of H_2SeO_4.

3.3.2 Molecular structure

The gas phase geometry optimized structure of Selenic acid (H_2SeO_4) is shown in Fig. 3.4, employing gradient corrected BLYP pseudo-potentials. It has a tetrahedral structure, with the $Se{=}O_{Se}$ and $Se{-}O_{Se,H}$ bond-lengths of 1.59 Å and 1.76 Å respectively. While the angle made by the double bonds ($O_{Se}{-}Se{-}O_{Se}$) is ~ 125°, that formed by the single-bonds ($O_{Se,H}{-}Se{-}O_{Se,H}$) is ~ 100°. The $O_{Se}{-}Se{-}O_{Se,H}$ bonds make an average angle of ~ 107°. In Fig. 3.5, the radial distribution functions (RDF) of the $Se{-}O_{Se}$ (intra-molecular) and the $O_{Se}{-}H$ (without distinguishing intra and inter-atomic hydrogen atoms) pairs are presented. In Fig. 3.5(a) the RDFs for $Se{-}O_{Se}$ (on an expanded *abscissa*) for both $HSeO_4^-$ and SeO_4^{2-} species are shown. The O_{Se}'s never get exchanged with the water oxygens, inferred from the visualization of the trajectory and is reflected by its zero intensity beyond 1.9 Å. For the SeO_4^{2-} species the $Se{-}O_{Se}$ RDF is unimodal as the four $Se{-}O_{Se}$ bonds are equivalent in solution, measuring an average bond length of 1.65 Å. However, the $Se{-}O_{Se}$ RDF for the $HSeO_4^-$ species is bimodal with three of the $Se{-}O_{Se}$ bonds (not bonded to H) in $HSeO_4^-$ species measures 1.63 Å, while the $O_{Se,H}$ bearing the hydrogen forms a longer bond length of 1.73 Å. These results are found to be in close agreement with the experimentally measured values by Eklund et al. [1]. They found the mean $Se{-}O_{Se}$ bond length for SeO_4^{2-} ion at 1.657 Å, determined by LAXS [20] and 1.643 Å by EXAFS [21]. This result is also in good agreement with the previous QMCF study on SeO_4^{2-} in aqueous conditions under normal pH conditions where the $Se{-}O_{Se}$

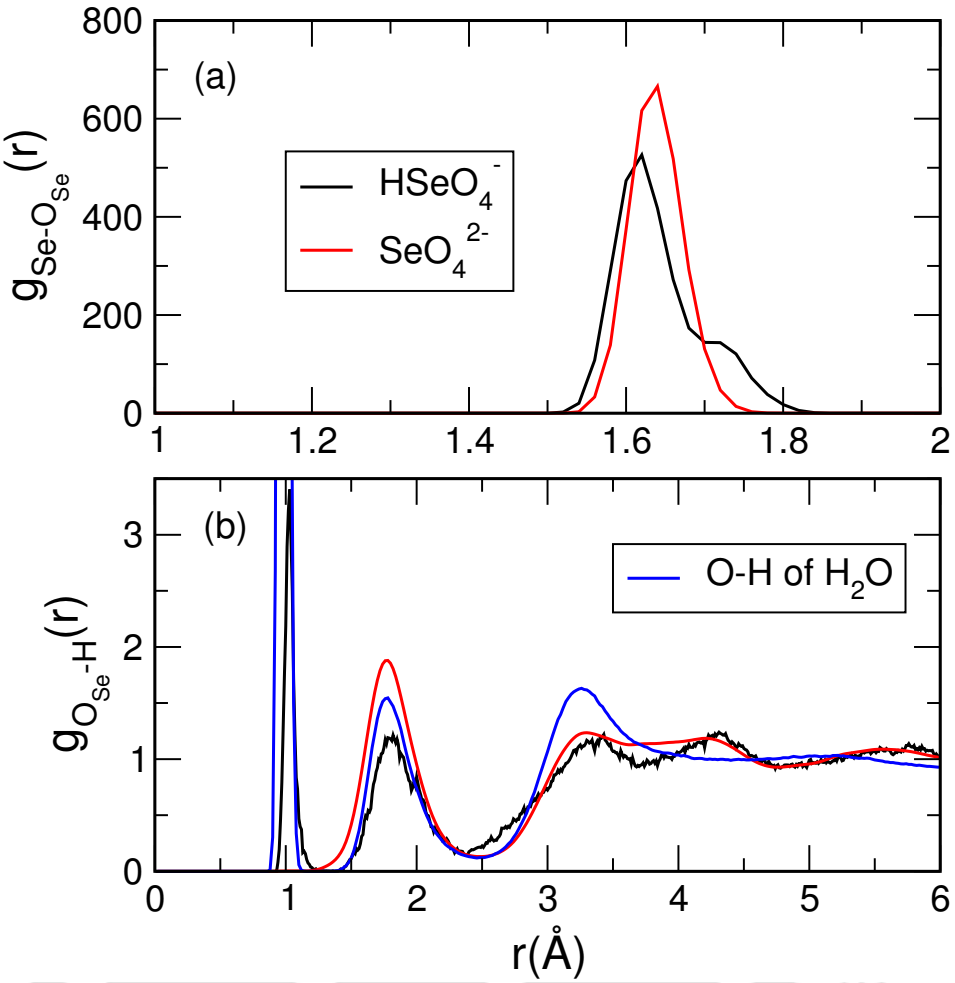

Figure 3.5: Radial distribution functions, $g(r)$'s, of $HSeO_4^-$ (black) and SeO_4^{2-} (red) systems between (a) Se–O_{Se} and (b) O_{Se}–H. O–H $g(r)$'s for the pure water (blue) from present CPMD simulations at 315 K are also shown. See text for the nomenclature employed.

bond-length was found to equal to 1.64 Å [2]. The RDFs of H, without distinguishing intra-molecular one for $HSeO_4^-$, around the O_{Se} are plotted in Fig. 3.5(b). For $HSeO_4^-$, the first sharp peak around 1.0 Å clearly marks the intra-molecular hydrogen, quite close to the O–H bond length for water. Both $HSeO_4^-$ and SeO_4^{2-} show peaks around 1.78 Å, whose minimum appearing with about 2.5 Å, are clearly the H-bonded ones. The higher peak intensity for SeO_4^{2-} shows its larger hydration shell, which shall be discussed later in detail. To get further insights of the structure, we have analyzed the angular distribution (figure not shown) individually for $HSeO_4^-$ and SeO_4^{2-} species. The O_{Se}–Se–O_{Se} angular distributions for SeO_4^{2-} are all peaked around the average value of 109.42°, close to the tetrahedral value of 109.5°. These values are in close

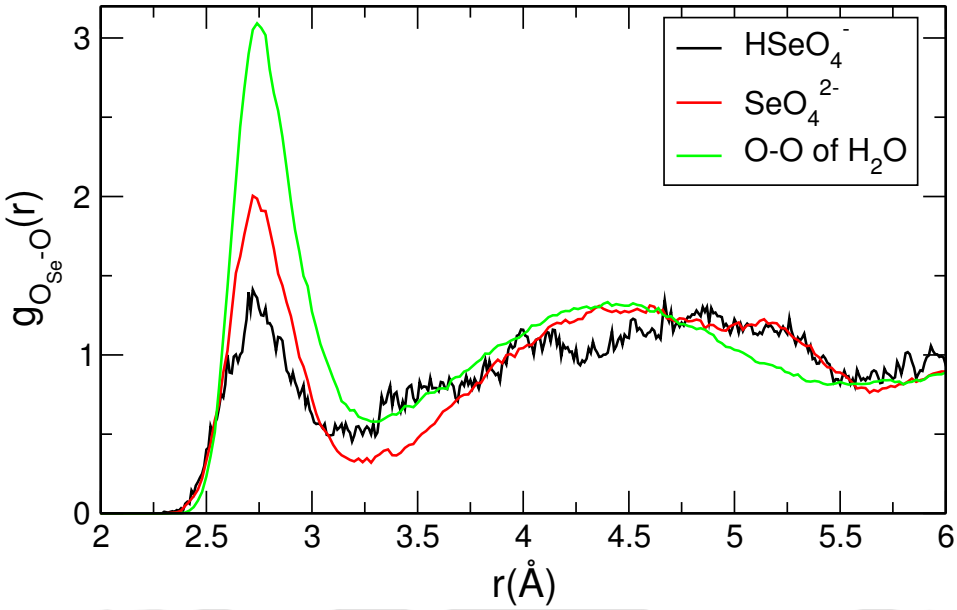

Figure 3.6: Oxygen-oxygen radial distribution functions (RDF) between solute species, $HSeO_4^-$ and SeO_4^{2-}, with water molecules, along with that of the pure-water system from the present CPMD simulations at 315 K.

agreement with experimental (109.5°) and simulation (109.0°) studies. For $HSeO_4^-$ the three $O_{Se}-Se-O_{Se}$ angles (of oxygens not bearing H) are at an average value of 112.27°, while $O_{Se}-Se-O_{Se,H}$ angle measures 106.4°.

3.3.3 Hydration structure

The hydration structure depends on the nature of solutes and their ability to accept or donate hydrogen-bonds with the surrounding water. Fig. 3.6 compares the oxygen-oxygen RDFs for the different solute species to solvent water oxygens. The $O_{Se}-O$ RDFs show significant differences in the hydration structure of $HSeO_4^-$ and SeO_4^{2-} species. While the first peak positions are similar for all the solute species, intensities at both the maxima as well as minima are slightly more pronounced for SeO_4^{2-} system, reflecting its more compact 1st hydration shell. The peak intensities in solute water systems are lower than those of pure water. The second hydration shell also display noticeable changes. O–O RDFs for pure water are found to be in good agreement with the previous CPMD simulations. The local hydration structures of the solutes are best visualized by spatial density distributions (SDD), shown in Fig. 3.7(a)-3.7(c). These are produced by transforming the coordinates of H-bonded water molecules to a selected

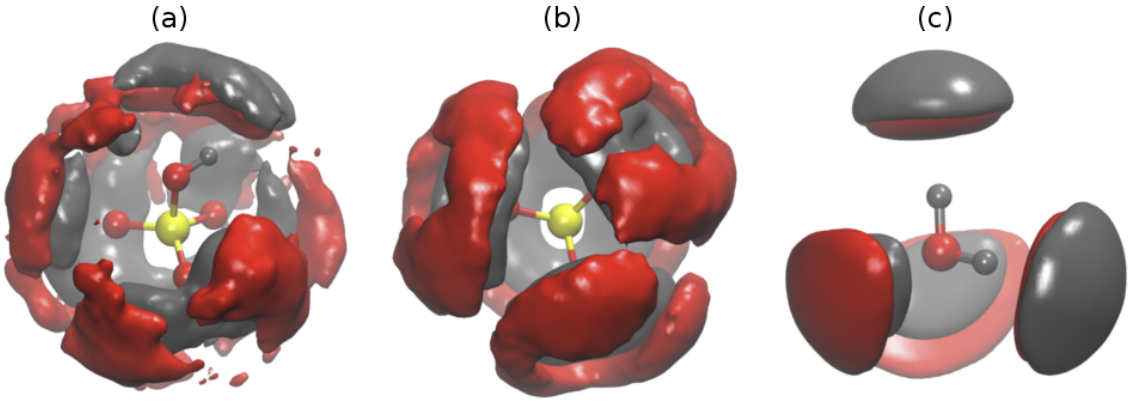

Figure 3.7: The spatial density distributions (SDD) of hydrogens (gray) and oxygens (red) of H-bonded H_2O molecules, around (a) the $HSeO_4^-$ (b) the SeO_4^{2-} species, and (c) a water molecule from the present simulation study. A uniform threshold number density (isovalue) of 0.04 $Å^{-3}$ is chosen for the isosurface in all the spatial density distribution plots.

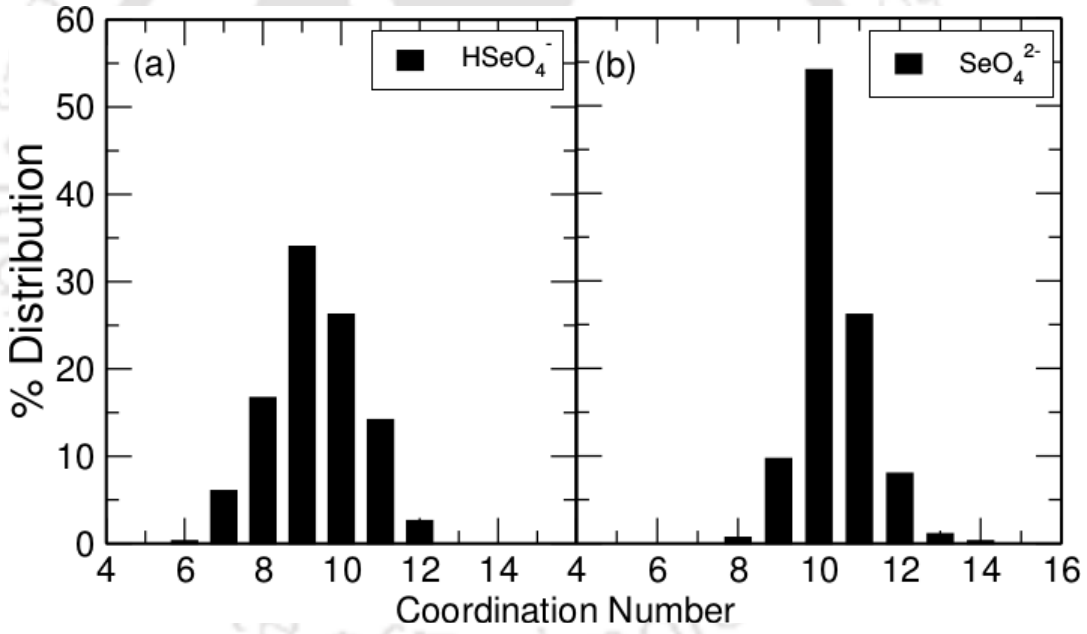

Figure 3.8: The coordination number distribution of solvent (oxygens of H_2O molecules) within 3.5 Å of oxygens of the solutes ($HSeO_4^-$) (a) and SeO_4^{2-}(b).

choice of body fixed axes of the solute species. These transformed coordinates are then mapped on to a fine 3-dimensional grid and averaged over the length of the simulation. These figures include all the oxygens (red) and hydrogens (gray) of the H_2O molecules solvating the solute species (employing the criteria defined in chapter 2). Fig. 3.7(a) and (b) show the water SDD around $HSeO_4^-$ and SeO_4^{2-} species respectively. In Fig. 3.7(c), the atomic SDD of H_2O molecules surrounding a H_2O molecule which are H-bonded

to the reference H_2O molecule are shown. Fig. 3.8(a) and 3.8(b) show the coordination number distribution (in percentage) of the solvents within 3.5 Å of oxygens of the solutes, $HSeO_4^-$ and SeO_4^{2-} respectively. These plots, in addition, gives the measure of the fluctuations in hydration shell of the solutes. It can be observed from these plots that SeO_4^{2-} has a much more compact water distribution around it than that of $HSeO_4^-$, consistent with the 3.7 plots shown above.

3.3.4 Hydrogen-bonding

The time averaged H-bond statistics, computed based on the H-bonding criteria (mentioned in chapter 2), suggests useful quantitative information about the solvated systems, as illustrated in Fig. 3.9. $O_{Se,H}$ of $HSeO_4^-$ donates, on an average, 0.97 H-bond to water and accepts 0.15 H-bonds; while the three O_{Se} accepts total of 5.7 H-bonds. The donated H-bond of $O_{Se,H}$ (that is $O_{Se,H}-H\cdots O$) nearly always remains intact, and to a specific water molecule, which presumably prevents it from accepting one full H-bond due to *steric* effects. The total number of H-bonds formed by $HSeO_4^-$ with surrounding water molecules is 6.8. SeO_4^{2-}, on the other hand, accepts a total of 9.20 H-bonds from water, significantly more in number than that of $HSeO_4^-$. This explains the higher stability of SeO_4^{2-} in less acidic aqueous environments. Fig. 3.9 also compares the statistics of water-water H-bonds dissolving $HSeO_4^-$ and SeO_4^{2-} species. The number of H-bonds between water dissolving $HSeO_4^-$ is 3.46 per H_2O molecules, while in SeO_4^{2-} this number becomes 3.36. Simulations of pure H_2O-system suggests water forms 3.62 H-bonds per H_2O molecule on an average (including accepted and donated), in agreement with the previous CPMD studies [22]. Thus, the number of water-water H-bonds dissolving selenate species are somewhat smaller compared to the pure H_2O-H_2O case.

Fig. 3.10 portraits the H-bond life-time correlation functions, $S_{HB}(t)$ and $S^d_{HB}(t)$, for the different H-bonds between selenate species with water. The H-bonds donated by $HSeO_4^-$ are labelled as $O_{Se,H}-H\cdots O$, and, accepted by O_{Se} are as $O_{Se}\cdots H-O$. The H-bonds accepted by the proton bearing $O_{Se,H}$ of $HSeO_4^-$ are too few (~ 0.15), and is not shown. The corresponding functions calculated for pure water are shown for useful comparison. It is proposed that the initial steep decay of $S_{HB}(t)$ is due to the cleavage of a small fraction of *weak* H-bonds, that only just-meets the H-bond geometry (of the donor-hydrogen-acceptor triplets). These peripheral H-bonds are susceptible to the faster internal modes, such as stretching and bending, of the donor-acceptor molecules. The

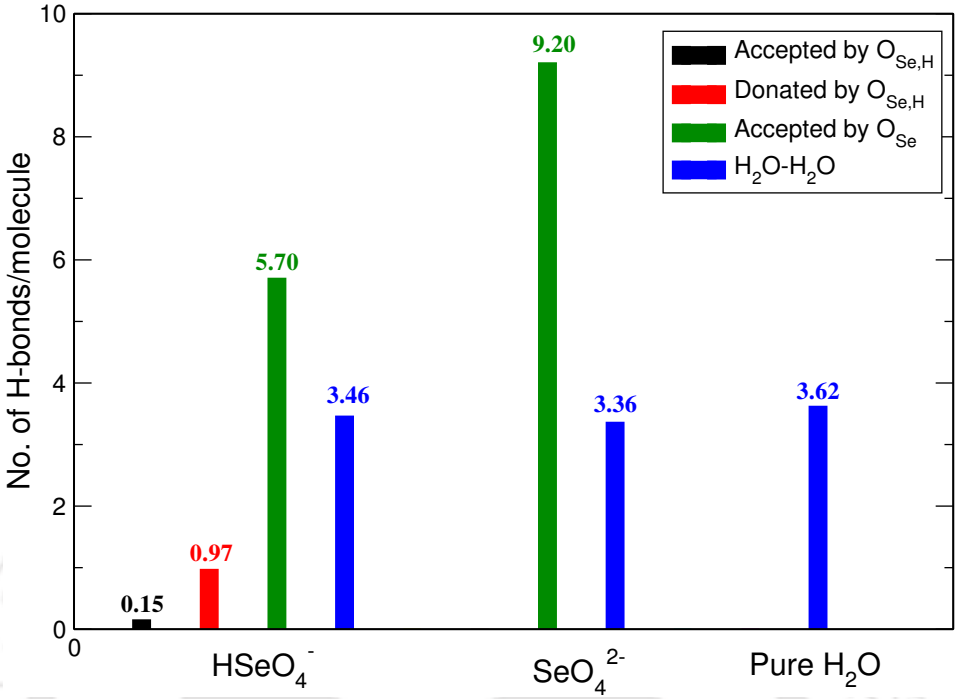

Figure 3.9: Statistics of H-bonds formed by different atomic species with water from the present CPMD simulation at 315 K. The water-water H-bonds (sum of the accepted and donated bonds per water molecule) are also shown.

dominant linear regime in ln $S^d_{\mathrm{HB}}(t)$, reflecting exponential decay, is attributed to the translational, diffusive modes of the surrounding water molecules. The characteristic time scales (fitted to the linear regime) of the $S_{\mathrm{HB}}(t)$, which is a measure of the life-time of H-bonds, is reported in Table 3.1 along with that of $S^d_{\mathrm{HB}}(t)$. The H-bonds accepted by the O_{Se} of the $SeO_4{}^{2-}$ clearly scores above those accepted by $HSeO_4{}^-$ and between water molecules, suggestive of their stronger nature. The lifetime calculated for pure water H-bonds is in agreement with previous CPMD simulation studies [22, 23]. The difference in the characteristic timescales of $S^d_{\mathrm{HB}}(t)$ and $S_{\mathrm{HB}}(t)$ in Table 3.1 suggest that reorientation of water molecules, over their translational motion, is the dominant mechanism of H-bond cleavage. The H-bond donated by $HSeO_4{}^-$ (i.e., $O_{Se,H}$ as donor) is qualitatively different from the rest, and makes very long-lived H-bonds (lifetime of 3.92 ps). With hardly any initial non-exponential decay, it stays linear all through over the period. It is noted in the movies of the dynamics that the water molecule accepting the H-bond from $HSeO_4{}^-$ stays-put without being replaced, until the species deprotonates. The slow decay of $S_{\mathrm{HB}}(t)$ noted owes to the wagging motion of the $O_{Se,H}-H$ bond. It shall be noted that the characteristic time-scales of $O_{Se,H}-H\cdots O$ H-bond reported in

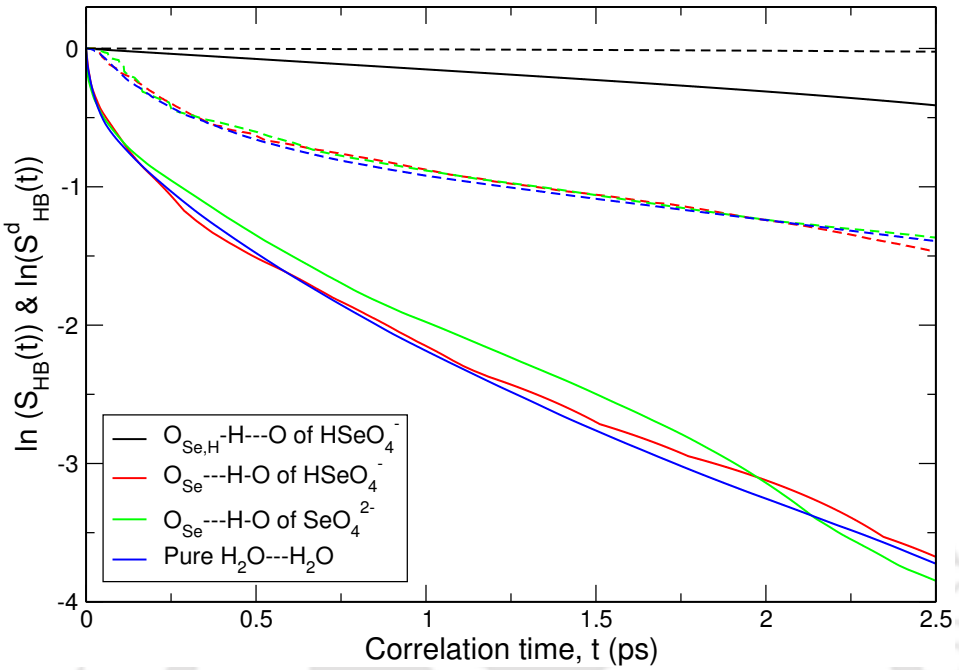

Figure 3.10: Comparison of the correlation functions, $S_{\mathrm{HB}}(t)$and $S^{d}_{\mathrm{HB}}(t)$, of H-bonds between selected atomic species. $S_{\mathrm{HB}}(t)$ are shown as continuous lines and the corresponding $S^{d}_{\mathrm{HB}}(t)$ in matching colors but by dotted lines.

Table 3.1: Lifetime estimates of different H-bonds, τ_s, computed from the correlation function $S_{\mathrm{HB}}(t)$, along with the characteristic decay time of $S^{d}_{\mathrm{HB}}(t)$, τ^{d}_{s}, for the different H-bonds.

System	H-bond type	τ_s(ps)	τ^{d}_{s}(ps)
$HSeO_4^-$	$O_{Se,H}-H\cdots O$	~ 3.92	~ 43.0
$HSeO_4^-$	$O_{Se}\cdots H-O$	0.76	3.05
SeO_4^{2-}	$O_{Se}\cdots H-O$	1.10	3.22
Pure water	$O-H\cdots O$	0.87	3.17

Table 3.1 is purely qualitative due to the short span over which $HSeO_4^-$ is continuously observed in the present simulation.

3.3.5 Vibrational density of states

The Fourier transformed velocity autocorrelation functions, often called power spectra, for aqueous $HSeO_4^-$ and SeO_4^{2-}-systems are shown in Fig. 3.11. The spectra for individual atomic species, H of $HSeO_4^-$ and H of pure-H_2O system are shown in the top panel of Fig. 3.11. The corresponding spectra of the different oxygens, O_{Se} and $O_{Se,H}$ of $HSeO_4^-$ as well as O_{Se} of SeO_4^{2-} are shown in the bottom panel. Over all, the predicted frequencies

are in good qualitative agreement with available experimental and theoretical studies [2, 24, 25].

Additionally, the frequencies from the vibrational analysis of gas phase $HSeO_4^-$ and SeO_4^{2-} are dubbed in both panes (up- and down-triangles) for ease of comparison. These gas phase frequencies along with a brief description of the modes are also provided for $HSeO_4^-$ and SeO_4^{2-}, respectively in Table 3.2 and Table 3.3. It shall be noted that the modes are in general of *mixed* character, and the description provided is qualitative, as is based on visualization of atomic displacements along the eigenvectors of the Hessian.

The $O_{Se,H}$ –H stretching mode of $HSeO_4^-$ observed at 3666 cm^{-1} in the gas-phase vibrational analysis, is found to be significantly red-shifted in aqueous environment, with a large dispersion spanning over 2000 – 3300 cm^{-1}. This is in significant contrast to the power spectra of H in pure-H_2O. The large red-shift of H ($HSeO_4^-$) in aqueous environment owes to the strong H-bonding $O_{Se,H}-H\cdots O$ with the surrounding waters, but should also be contributed by the weak $O_{Se,H}$ – H bond that is on the verge of breaking. The *drag effect* on the lighter hydrogen by the large fictitious electron mass (that is crucial to the efficiency of the Car-Parrinello scheme) also contributes to this effect. The intensity around 1230 cm^{-1} in H ($HSeO_4^-$) spectra (top panel, Fig. 3.11) is be attributed to the bending of the $O_{Se,H}$ – H bond about the Se – $O_{Se,H}$ bond observed at 1039 cm^{-1} in the gas-phase analysis (Table 3.2). The visualization shows that only the H ($HSeO_4^-$) species makes noticeable displacement in this particular mode, consistent with the lack of intensity around this frequency in the $O_{Se,H}$ spectrum shown in green on the lower panel of Fig. 3.11. The intensity in H spectra over 250-1000 cm^{-1} suggest that the various stretching and bending modes of oxygens also involve some degree of displacement of this species. The intensity around 150 cm^{-1} in the H spectrum coincides with the wagging mode observed at 132 cm^{-1} in gas-phase $HSeO_4^-$.

The spectra of all oxygen species of $HSeO_4^-$ and SeO_4^{2-} (lower panel, Fig. 3.11) are qualitatively very similar, all exhibits varying amounts of red-shifts of their stretching modes ($600-950$ cm^{-1}) relative to gas-phase. The bending modes of both species are confined to a relatively narrow range of $250-400$ cm^{-1}. The $O_{Se,H}$ spectra (shown in green, lower panel in Fig. 3.11) shows maximum red-shift which is consistent with the strong nature of its donated H-bond ($O_{Se,H}-H\cdots O$) noted earlier. The O_{Se} spectra of $HSeO_4^-$ (shown in blue) suggests varying degrees of red-shifts for the Se^- O_{Se} stretching modes; however that of the SeO_4^{2-} presents a more complex behaviour. The two higher frequency modes, as given in table 3.3, correspond to asymmetric and symmetric stretch-

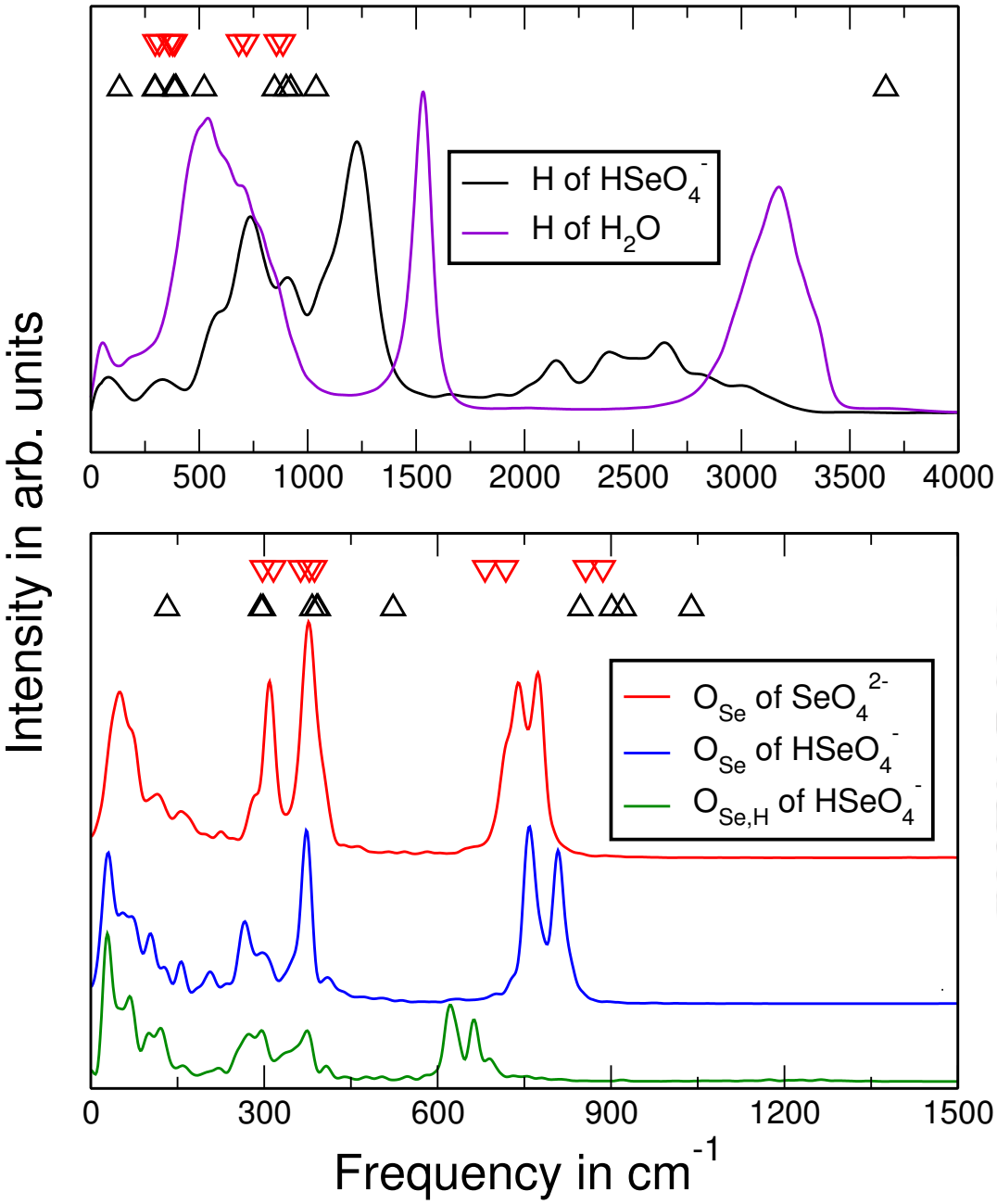

Figure 3.11: Power spectra of vibrational modes calculated from the Fourier transform of velocity autocorrelation function of the atomic motions in the aqueous environment. The gas phase vibrational modes for $HSeO_4^-$ and SeO_4^{2-} species are shown by black and red triangles respectively.

ing of the same $Se-O_{Se}$ pairs (with O_{Se} species labelled 2 and 3), presumably forming $Se=O_{Se}$ double bonds, while the two lower frequency stretches, forming $Se-O_{Se}$ single bonds (with the O_{Se} species labelled 1 and 4). All the four $Se-O_{Se}$ bonds of SeO_4^{2-}

Table 3.2: Gas-phase frequencies of $HSeO_4^-$ along with a qualitative description of the normal modes.

Serial no.	Frequency (cm^{-1})	Description
1	132	Wagging mode of $O_{Se,H}-H$.
2 - 6	294, 298, 383, 391, 393	Various $O_{Se}-Se-O_{Se}$ bending modes.
7	523	$Se-O_{Se,H}$ stretching mode.
8	847	$Se-O_{Se}$ symmetric stretching involving all three O_{Se}.
9	902	$Se-O_{Se}$ stretching involving three O_{Se}. Two of them are in phase, while the third is out-of phase w.r.t. to the other two.
10	922	$Se-O_{Se}$ asymmetric stretching involving two O_{Se} atoms.
11	1039	$Se-O_{Se,H}-H$ bending.
12	3666	$O_{Se,H}-H$ stretching.

Table 3.3: Gas-phase frequencies of SeO_4^{2-} along with a qualitative description of the normal modes.

Serial no.	Frequency (cm^{-1})	Description
1-5	387, 378, 363, 316, 297	Various $O_{Se}-Se-O_{Se}$ bending modes
6	682	$Se-O_{Se}$ asymmetric stretching involving $O_{Se}(1)$ & $O_{Se}(4)$
7	718	$Se-O_{Se}$ symmetric stretching involving $O_{Se}(1)$ & $O_{Se}(4)$
8	856	$Se-O_{Se}$ symmetric stretching involving $O_{Se}(2)$ & $O_{Se}(3)$
9	886	$Se-O_{Se}$ asymmetric stretching involving $O_{Se}(2)$ & $O_{Se}(3)$

being practically identical in solution, the double peaks in power spectrum presumably distinguishes the asymmetric and symmetric stretches.

The bending modes of $O_{Se}-Se-O_{Se}$ spread in the range of 250-400 cm^{-1} are hardly affected in solution environment. The intensities at low frequencies (0-200 cm^{-1}) are attributed to various rigid-body like tumbling modes of $HSeO_4^-$ and SeO_4^{2-} species under the potential energy basin of surrounding water molecules.

3.4 Conclusion

In this chapter, we have discussed results from the detailed Car-Parrinello *ab initio* molecular dynamics simulation on selenate species in aqueous environment. H_2SeO_4 is found to deprotonate quickly, forming $HSeO_4^-$ which exhibits a dynamic equilibrium with SeO_4^{2-} in aqueous environment owing to its strong acidic character with low pK_{a1} and pK_{a2} values of −3.0 and 1.70 respectively. The hydrogen of $HSeO_4^-$ forms strong and prolonged H-bond to an immediate water molecule, while its oxygen bearing the hydrogen rarely accepts one from the surrounding hydration shell. SeO_4^{2-} is observed to make a more compact first hydration shell, and attracts larger number of hydrogen bonds compared to $HSeO_4^-$. This explains the greater stability of the SeO_4^{2-} species particularly in less acidic environments. Analysis of the life-time suggests that H-bonds accepted by SeO_4^{2-} are longer lived than those between water molecules, while those accepted by $HSeO_4^-$ are comparatively slightly short lived. The breakings of the individual H-bonds owe dominantly to the rotational/librational motion of the surrounding water molecules, rather than translation diffusion.

Fresh insights on vibrational properties of the $HSeO_4^-$ and SeO_4^{2-} species are derived from the power spectra analysis. Comparison with gas-phase normal-mode analysis provides qualitative information on the origin of intensities in the predicted spectra. The stretching modes of these species in general show significant red-shifts in aqueous environment due to strong H-bonding with water, while the bending modes are hardly affected. These qualitative understanding would be useful for the spectroscopic investigations of speciation and reactivity of selenium in aqueous environment.

BIBLIOGRAPHY

[1] Lars Eklund and Ingmar Persson. Structure and hydrogen bonding of the hydrated selenite and selenate ions in aqueous solution. *Dalton Trans.*, 43(17):6315–6321, 2014.

[2] Theerathad Sakwarathorn, Sangobtip Pongstabodee, Viwat Vchirawongkwin, Lorenz R Canaval, Andreas O Tirler, and Thomas S Hofer. Characteristics of selenate in aqueous solution–an ab initio qmcf-md study. *Chemical Physics Letters*, 595:226–229, 2014.

[3] Pierre Hohenberg and Walter Kohn. Inhomogeneous electron gas. *Phys. Rev.*, 136(3B):B864, 1964.

[4] Walter Kohn and Lu Jeu Sham. Self-consistent equations including exchange and correlation effects. *Phys. Rev.*, 140(4A):A1133, 1965.

[5] Roberto Car and Michele Parrinello. Unified approach for molecular dynamics and density-functional theory. *Phys. Rev. Lett.*, 55(22):2471, 1985.

[6] CPMD. General program to perform ab initio molecular dynamics simulations. *CPMD developers group under the terms of the GNU General Public License, http://www.cpmd.org*.

[7] J Hutter. Car-parrinello molecular dynamics-an electronic structure and molecular dynamics program. *CPMD Manual*, 2012.

[8] Melvin Edison Diemer and Victor Lenher. The specific gravity and percentage strength of selenic acid. *J. Phys. Chem.*, 13(7):505–511, 1909.

[9] Axel D Becke. Density-functional exchange-energy approximation with correct asymptotic behavior. *Phys. Rev. A*, 38(6):3098, 1988.

[10] Chengteh Lee, Weitao Yang, and Robert G Parr. Development of the colle-salvetti correlation-energy formula into a functional of the electron density. *Phys. Rev. B*, 37(2):785, 1988.

[11] Shūichi Nosé. A molecular dynamics method for simulations in the canonical ensemble. *Mol. Phys.*, 52(2):255–268, 1984.

[12] Shuichi Nosé. A unified formulation of the constant temperature molecular dynamics methods. *J. Chem. Phys.*, 81(1):511–519, 1984.

[13] Dominik Marx and Jürg Hutter. *Ab initio molecular dynamics: basic theory and advanced methods*. Cambridge University Press, 2009.

[14] Glenn J Martyna and Mark E Tuckerman. A reciprocal space based method for treating long range interactions in ab initio and force-field-based calculations in clusters. *J. Chem. Phys.*, 110(6):2810–2821, 1999.

[15] Anil Kumar Tummanapelli and Sukumaran Vasudevan. Ab initio md simulations of the brønsted acidity of glutathione in aqueous solutions: Predicting pka shifts of the cysteine residue. *J. Phys. Chem. B*, 119(49):15353–15358, 2015.

[16] Anil Kumar Tummanapelli and Sukumaran Vasudevan. Ab initio molecular dynamics simulations of amino acids in aqueous solutions: Estimating pka values from metadynamics sampling. *J. Phys. Chem. B*, 119(37):12249–12255, 2015.

[17] Anil Kumar Tummanapelli and Sukumaran Vasudevan. Dissociation constants of weak acids from ab initio molecular dynamics using metadynamics: Influence of the inductive effect and hydrogen bonding on pka values. *J. Phys. Chem. B*, 118(47):13651–13657, 2014.

[18] Dominik Marx. Proton transfer 200 years after Von Grotthuss: Insights from ab initio simulations. *ChemPhysChem*, 7(9):1849–1870, 2006.

[19] CJT De Grotthuss. *Mémoire sur la décomposition de l'eau: et des corps qu'elle tient en dissolution à l'aide de l'électricité galvanique*. 1805.

[20] Sergei G Podorov, NN Faleev, KM Pavlov, DM Paganin, SA Stepanov, and E Förster. A new approach to wide-angle dynamical x-ray diffraction by deformed crystals. *J. Appl. Crystallogr.*, 39(5):652–655, 2006.

[21] Boon K Teo. *EXAFS: basic principles and data analysis*, volume 9. Springer Science & Business Media, 2012.

[22] P Padma Kumar, Andrey G Kalinichev, and R James Kirkpatrick. Hydrogen-bonding structure and dynamics of aqueous carbonate species from car- parrinello molecular dynamics simulations. *J. Phys. Chem. B*, 113(3):794–802, 2008.

[23] Amalendu Chandra. Effects of ion atmosphere on hydrogen-bond dynamics in aqueous electrolyte solutions. *Phys Rev Lett*, 85(4):768, 2000.

[24] GE Walrafen. Raman spectral studies of aqueous solutions of selenic acid. *J. Chem. Phys.*, 39(6):1479–1492, 1963.

[25] K Sathianandan, LD McCory, and JL Margrave. Infrared absorption spectra of inorganic solids—iii selenates and selenites. *Spectrochim. Acta*, 20(6):957–963, 1964.

CHAPTER 4

AIMD STUDY OF WATERBORNE SE–IV SPECIES

4.1 Introduction

In addition to Se–VI species, the other form of selenium that is highly soluble in aqueous conditions is the valence state IV, the parent form is known as selenous acid (H_2SeO_3). This is a weaker acid compared to H_2SeO_4, having experimentally reported pK_{a1} value of 2.62[1]. Its mono-deprotonated form ($HSeO_3^-$) is stable in normal aqueous conditions, and is a weak acid, with pK_{a2} = 8.32 [1].

$$H_2SeO_3 \xrightarrow[2.62]{pK_{a1}} HSeO_3^- \xrightarrow[8.32]{pK_{a2}} SeO_3^{2-} \tag{4.1}$$

The structure and hydrogen bonding of hydrated H_2SeO_3 and $HSeO_3^-$ have been recently probed experimentally employing large angle X-ray scattering (LAXS), EXAFS and double difference infrared (DDIR) spectroscopy by Eklund and Persson [1]. Reportedly, Se–IV species are more toxic, soluble and mobile compared to those of Se–VI [2–5].

In this chapter, we are reporting a comprehensive CPMD study of water-borne Se–IV species, H_2SeO_3, $HSeO_3^-$ and SeO_3^{2-}, in aqueous environment. Fresh insight on the hydration, hydrogen bonding and vibrational properties is presented.

An article based on this chapter is published in *Phys. Chem. Chem. Phys*, vol. **18**, year 2016, pages 26755-26763; title: "Ab initio molecular dynamics study of Se–IV species in aqueous environment"; authors Sangkha Borah and P. Padma Kumar. Selected contents are reproduced with permission ©Royal Society of Chemistry 2016.

4.2 Methods

CPMD simulation is carried out at 315 K on the following systems:

1. One molecule of selenous acid (H_2SeO_3) solvated by 60 H_2O molecules: CPMD trajectory of 90 ps is generated for detailed analysis (after dedicating 30 ps for equilibration). As detailed in the next section, several proton transfer events between the species and the surrounding water molecules are observed, thus establishing a dynamic equilibrium between H_2SeO_3 and $HSeO_3^-$ species. The extended periods of existence of H_2SeO_3 and $HSeO_3^-$ during the course of the simulation permit analysis of the solvation behavior of both species.

2. One SeO_3^{2-} ion solvated in 60 H_2O molecules: this system is prepared to investigate the solvation of SeO_3^{2-} species, however the species quickly protonates forming $HSeO_3^-$ (owing to the high pK_{a2} value of 8.32), and therefore the run is discarded for further analysis after 30 ps.

3. SeO_3^{2-} ion solvated by 59 H_2O molecules and one hydroxyl (OH^-) ion: the SeO_3^{2-} species is observed to stay stable, without protonation during the 30 ps-long production run (after dedicating 40 ps for equilibration).

4. Furthermore, gas-phase geometry optimization of all three species is carried out, followed by normal mode analysis. These calculations are intended to gain a qualitative understanding of the vibrational modes corresponding to the power spectra intensities in the solution phase.

All the solution-phase calculations are carried out in a cubic box of 12.42 Å, at an approximate density of 1.05 g/cc. The initial configuration for system (i) above is prepared from the final configuration of our previous simulation of H_2SeO_4 solvated in 60 water molecules (in a 12.42 Å box), further geometry-optimized, and equilibrated for 30 ps of CPMD simulation at 315 K. The initial configuration for the subsequent runs follows the well-equilibrated structures from previous runs, with necessary deletion of atoms, followed by geometry optimization, and CPMD equilibration for not less than 30 ps at 315 K. The gas-phase normal mode analyses are carried out employing Martyna–Tuckerman [6] Poisson solver as implemented in CPMD software. Additionally, results from one of our earlier CPMD simulations of a pure water system, consisting of 64 H_2O molecules in a cubic box of 12.42 Å, are drawn in for the sake of useful comparisons.

All simulations are carried out at the same technical level: norm-conserving pseudopotentials with gradient-corrected BLYP functionals are employed. Kohn–Sham orbitals are expanded in the plane wave basis up to a cut-off of 85 Ry. MD simulations are carried out in the canonical (NVT) ensemble using Nose-Hoover thermostats at a temperature of 315 K. A fictitious electronic mass of 600 a.u. is employed, and the classical kinetic energy for the electronic degrees of freedom is maintained around 0.03 a.u. A time step of 4 a.u. (~ 0.1 fs) is used for integration. All simulations are performed with the CPMD software, version 3.15.3.

For the convenience of discussion, we will designate the intra-molecular oxygen atoms of H_2SeO_3, $HSeO_3^-$, and SeO_3^{2-} as $O_{Se,H}$ or O_{Se}, based on whether it is bonded to an intra-molecular H or not, and the oxygens and hydrogen of water by O and H respectively.

4.3 Results and Discussions

4.3.1 Molecular Structure

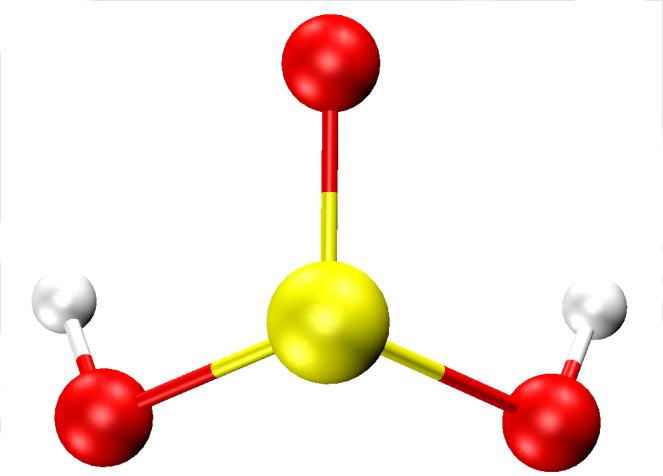

Figure 4.1: Geometry optimized gas phase structure of H_2SeO_3.

For the geometry-optimized H_2SeO_3 (Fig. 4.1) the $Se-O_{Se,H}$ and $Se-O_{Se}$ bond lengths are respectively 1.80 and 1.61 Å. The SeO_3 unit is non-planar, having a trigonal pyramidal structure with Se at its apex. The hydrogens are off-plane to the pyramidal base with the dihedral angles $O_{Se}-Se-O_{Se,H}-H$ measuring 16.5 degrees. The $O_{Se,H}-H$ bond lengths are 0.98 Å, close to those of water. In the solution phase the average $Se-O_{Se,H}$

and Se – O_{Se} bond lengths are respectively 1.77 and 1.62 Å, slightly shorter than the gas-phase value. For $HSeO_3^-$, the Se – $O_{Se,H}$ and Se – O Se bond lengths are 1.93 and 1.65 Å in the gas phase, against their respective average values of 1.80 and 1.65 Å in solution. The Se – O_{Se} bond lengths in SeO_3^{2-} are 1.68 and 1.69 Å respectively in the gas phase and in solution. The oxygen-selenium-oxygen angles are found to increase by 3 – 4 degrees down this series.

4.3.2 Proton transfer events

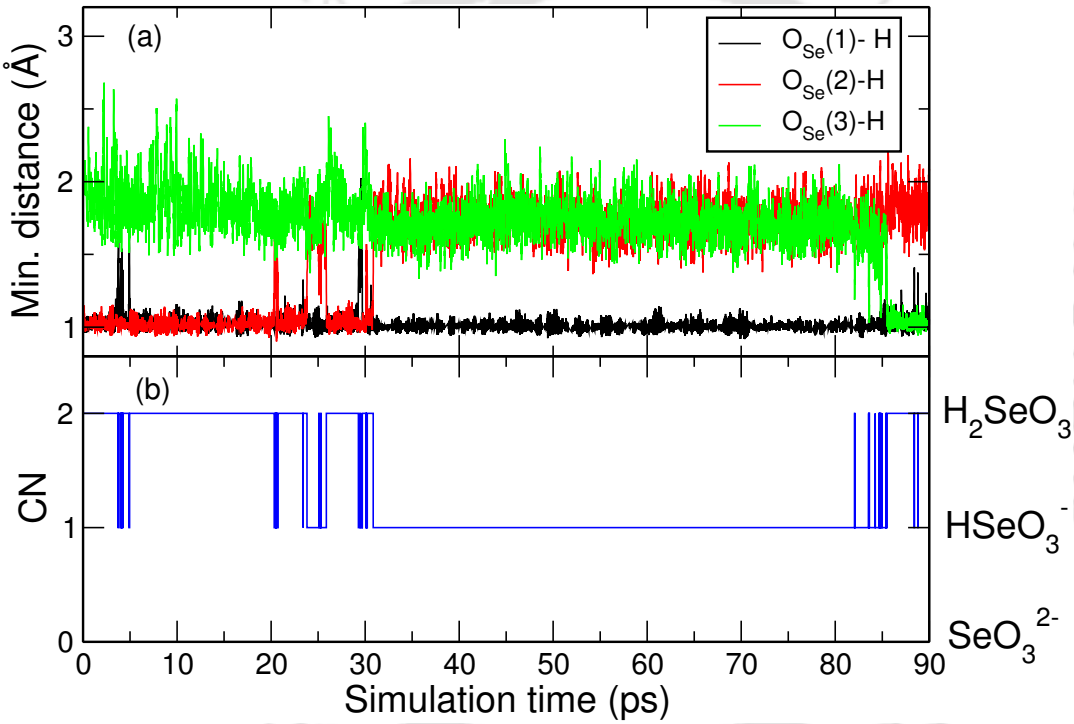

Figure 4.2: (a) Time evolution of the distance to the nearest H atom in the system from each of the solute oxygens (O_{Se}(1) to O_{Se}(3)), for system (i) in methods. (b) The evolution of digitalized total hydrogen coordination (CN) of the solute, applying a cut-off criterion of 1.3 Å for O_{Se} – H distances to the data in (a). See text for more detail.

With an experimental pK_{a1} value of 2.62, the H_2SeO_3 molecule deprotonates to the $HSeO_3^-$ species, but no further deprotonation leading to the formation of SeO_3^{2-} is observed during the 90 ps of production runs. This is due to the high pK_{a2} value of 8.32 reported in experimental studies. The proton transfer events,

$$H_2SeO_3 + H_2O \rightleftharpoons HSeO_3^- + H_3O^+ \tag{4.2}$$

observed during the simulation of $60\,H_2O + H_2SeO_3$ (system (i) in methods) can be monitored by the minimum $O_{Se} - H$ distance, among all possible values between a given O_{Se} and H atom in the system (that is, without distinguishing the hydrogens of the solute species and solvent). In Fig. 4.2(a), where individual O_{Se} atoms are labeled $O_{Se}(1) - (3)$, it may be seen that $O_{Se}(1)$ and $O_{Se}(2)$ are in the protonated state in the beginning of the production run signaling selenium as H_2SeO_3. Meanwhile, $O_{Se}(1)$ remains almost always bonded (shown in black) to a hydrogen, and $O_{Se}(2)$ (shown in red) deprotonates around 30 ps of simulation for good, following the forward reaction in Eq. (4.2). The selenium thus exists as $HSeO_3$ resulting in the surrounding solvent being acidic. This prompts the protonation of $O_{Se}(3)$ (shown in green) around 85 ps, suggesting the existence of a dynamic equilibrium between H_2SeO_3 and $HSeO_3^-$ as in Eq. (4.2).

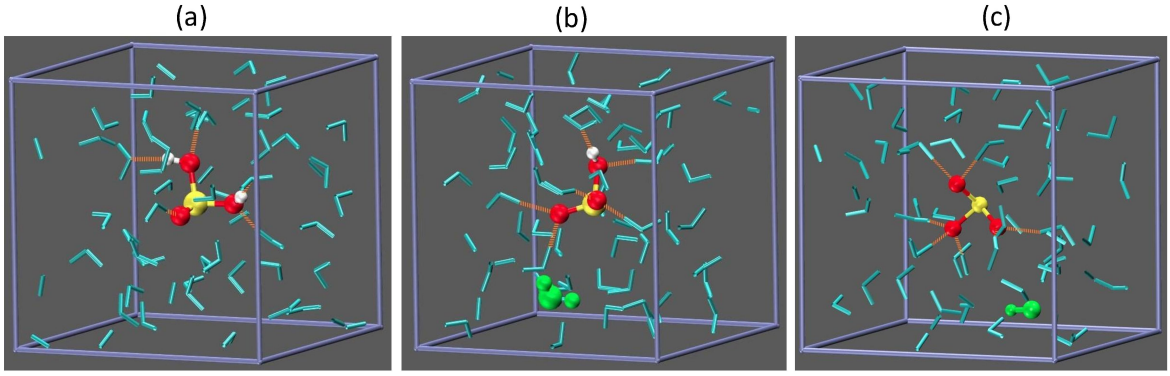

Figure 4.3: Snapshots showing the presence of (a) H_2SeO_3 and (b) $HSeO_3^-$ from the simulation of system (i) in methods. (c) Snapshot of SeO_3^{2-} hydration from system (iii) in methods. H_2O molecules are shown as sticks in cyan. Instantaneous H-bonds with the central solute species are shown in brown dotted lines. The hydronium (H_3O^+) and hydroxide (OH^-) ions are shown as green balls.

In Fig. 4.2(b), the sum of the hydrogen coordination of the three O_{Se} atoms applying an $O_{Se} - H$ cut-off distance of 1.3 Å is plotted. Clearly, the hydrogen coordination numbers of two and one signal the presence of H_2SeO_3 and $HSeO_3^-$ species respectively. SeO_3^{2-} does not make an appearance in this system during the entire run. As mentioned in the previous section, the second set of simulations (system (ii) discussed in the previous section) on $SeO_3{}^{2-}$ is in neutral aqueous conditions, and the species quickly captures one hydrogen from the surrounding solution forming $HSeO_3^-$ which remained stable for the rest of the simulation. However, in a basic environment containing one hydroxide ion (OH^-) and 59 H_2O molecules (system (iii)), SeO_3^{2-} remains perpetual without protonation during the entire course of simulation. In Fig. 4.3(a)–(c), snapshots of

H_2SeO_3 , $HSeO_3^-$ (from simulation of system (i) in methods) and SeO_3^{2-} (from simulation of system (iii) in methods) in aqueous environment from the present simulation are shown. The hydronium ion, H_3O^+ , and hydroxide ion, OH^-, are shown as green balls, respectively in Fig. 4.2(b) and 4.2(c). The instantaneous H-bonds formed by the solute are shown in brown lines.

4.3.3 Hydration Structure

The hydration structure of a solute is characterized by the number of H-bonds formed by the solute with the solvent molecules, as well as on their strengths. In other words, it is related to the geometrical arrangements of the surrounding solvent molecules with respect to the solute. To characterize the statistical distribution of H_2O molecules around the Se – IV species, the radial distribution functions (RDFs) of $O_{Se} - H$ and $O_{Se} - O$ pairs are shown respectively in Fig. 4.4(a) and 4.4(b). The changes in the surrounding water structure due to the presence of these species could be inferred in the $O - O$ RDFs between H_2O molecules, shown in Fig. 4.4(c) (the same for pure H_2O is also shown for comparison). The 1^{st} sharp peak in the $O_{Se} - H$ RDF in Fig. 4.4(a) is due to the intra-molecular hydrogen. The 2^{nd} peak in the $O_{Se} - H$ RDF largely accounts for the hydrogen of H-bonded water molecules that manifest as the first peak in the $O_{Se} - O$ RDF in Fig. 4.4(b). A few peaks in the $O_{Se} - H$ RDF beyond the 1^{st} hydration shell, which contrasts with that of pure water, suggest some degree of orientational ordering of hydrogen radially from the solute species. Both the $O_{Se} - O$ and $O_{Se} - H$ RDFs display an increasing order of hydration structure, from the H_2SeO_3, through $HSeO_3^-$ to SeO_3^{2-} systems. A higher degree of compactness of the solvent around the SeO_3^{2-} species is evident from the more pronounced maxima as well as the minima of its 1^{st} hydration shell.

The 3D spatial density distribution (SDD) of solvent oxygens and hydrogens, of H-bonded water molecules, around the solute species in Fig. 4.5, provides a direct qualitative illustration of the features noted above. The hydration shell for $HSeO_3^-$ is more prominent and well defined than that of H_2SeO_3. However, SeO_3^{2-} in its basic environment exhibits the most distinct hydration shell. The distributions of the water molecules around the solvents, calculated based on the H-bond criterion (i) explained above, are shown in Fig. 4.6(a)-(c). These plots, in addition, gives the measure of the fluctuations in hydration shell of the solutes. It can be observed from these plots that H_2SeO_3 has a more diffused

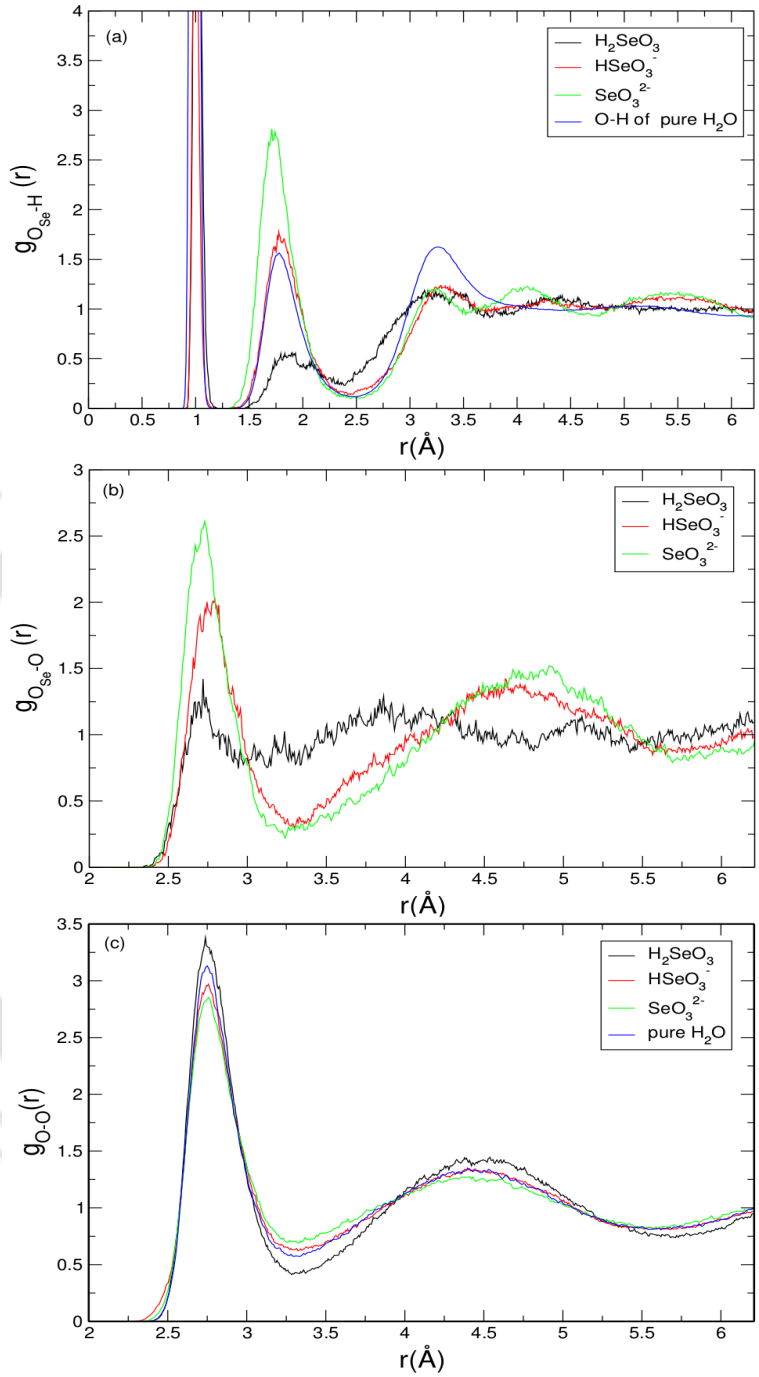

Figure 4.4: Atomic radial distribution functions (RDFs), $g(r)$, of (a) O_{Se}–H pairs (including the intra-molecular hydrogens as well) and (b) O_{Se}–O pairs for H_2SeO_3, $HSeO_3^-$, and SeO_3^{2-} species. (c) O – O $g(r)$ for water dissolving the three species is shown along with that of pure H_2O.

hydration shell compared to $HSeO_3{}^-$ and $SeO_3{}^{2-}$, consistent with the 4.5 plots.

Although visually it is not so prominent to assign significance, the water dissolving

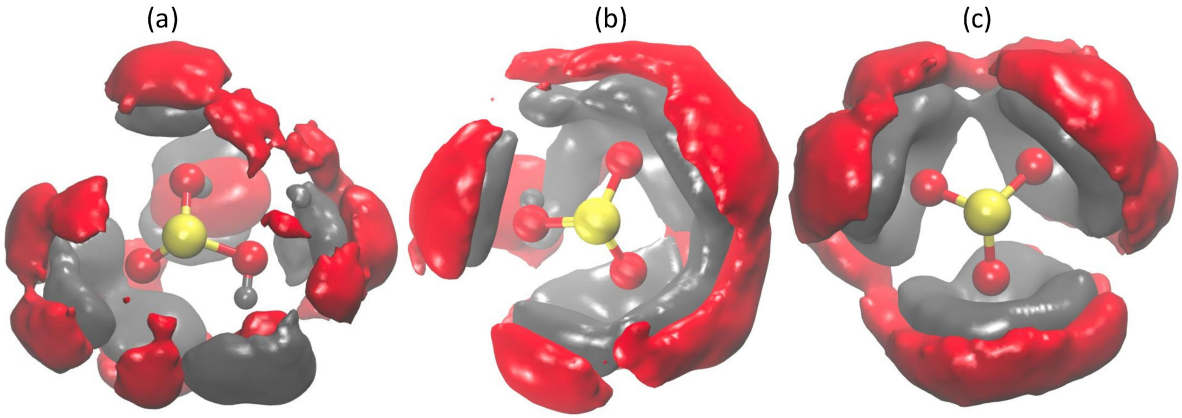

Figure 4.5: The 3D spatial density distribution (SDD) of hydrogen (as grey surfaces) and oxygen (as red surfaces) atoms of H_2O molecules H-bonded to (a) H_2SeO_3, (b) $HSeO_3^-$ and (c) SeO_3^{2-}. These are shown alongside for a uniform iso-density of 0.04 $Å^{3-}$ for all cases.

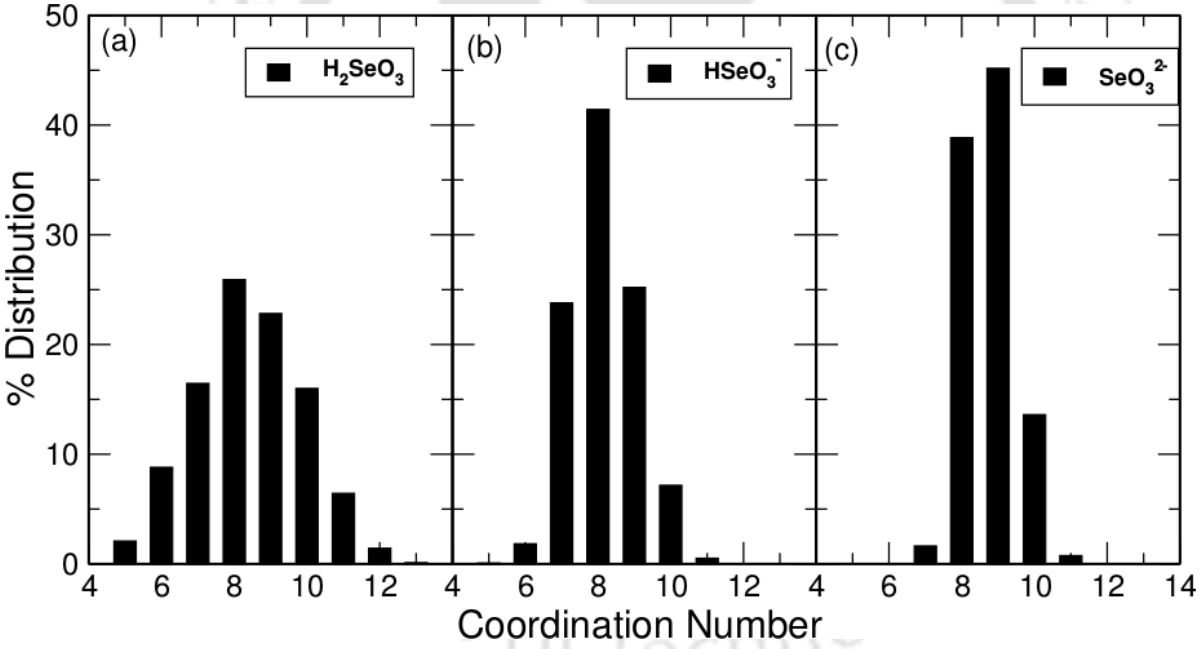

Figure 4.6: The distribution (in percentage) of the water molecules around (a) H_2SeO_3, (b) $HSeO_3^-$ and (c) SeO_3^{2-} calculated based on the hydrogen-bond criterion (i) explained above.

H_2SeO_3, shown in Fig. 4.4(c), exhibits relatively higher maxima and deeper minima in the O – O RDFs than those of $HSeO_3^-$, SeO_3^{2-} and that of pure H_2O. Thus, at the expense of a relatively weak solute-solvent structure, H_2SeO_3 promotes the solvent structure. The consequence of this on the lifetime and structural relaxation of the water-water H-bonds is more dramatic, as discussed in detail in the next sub-sections.

4.3.4 Hydrogen bonding

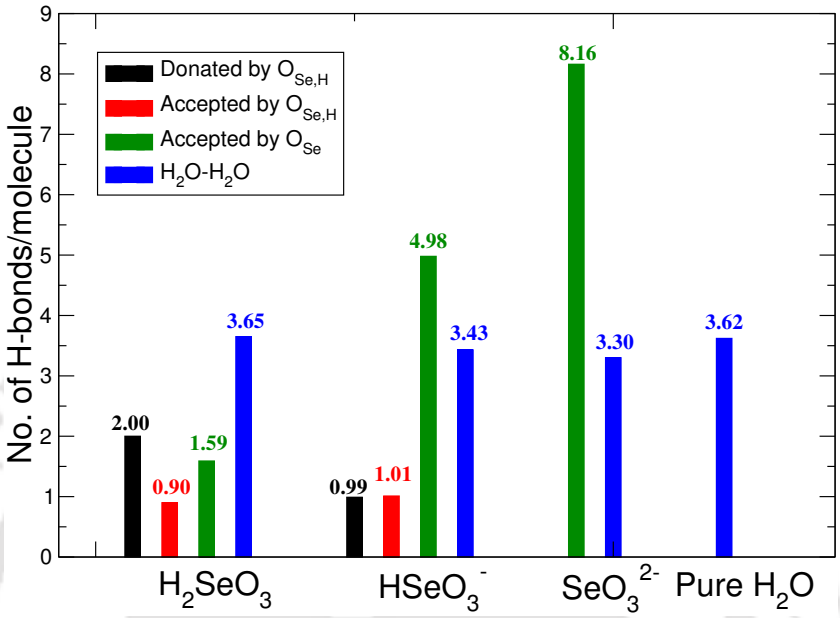

Figure 4.7: The statistics of the different types of H-bonds formed per solute molecules. The H-bonds between water molecules (both as donor and acceptor) dissolving the three selenium species, as well as that of pure water, are also shown.

Fig. 4.7 offers a quantitative comparison of the total number of H-bonds formed by their different atomic sites of the three Se−IV species. The total numbers of H-bonds formed by the species increase from H_2SeO_3, $HSeO_3^-$ to SeO_3^{2-} consistent with the compactness of hydration shells noted earlier. The $O_{Se,H}$ site of $HSeO_3^-$ practically always donates as well as accepts one H-bond from water. In H_2SeO_3 the two $O_{Se,H}$ sites almost always donate a H-bond. The $O_{Se,H}$ also accepts H-bonds but less frequently, at about 0.5 per site on average. The number of H-bonds accepted on average by the individual O_{Se} sites (not bearing a hydrogen) increases across the series. at about 1.6 for H_2SeO_3, 2.5 for $HSeO_3^-$ and 2.7 for SeO_3^{2-} (note that Fig. 4.7 reports the total number per solute species). This is attributed largely to the increase in the effective charge on the O_{Se} species across the series, though *steric* factors would also play a role.

Fig. 4.7 also compares the total number of water–water H-bonds (as the sum of accepted and donated per H_2O molecule) in the solution dissolving the three Se−IV species as well as that of pure H_2O. Reflected in the O − O RDFs discussed earlier, the number of H-bonds between the water molecules steadily decreases with an increase in the hydration structure of the Se−IV species.

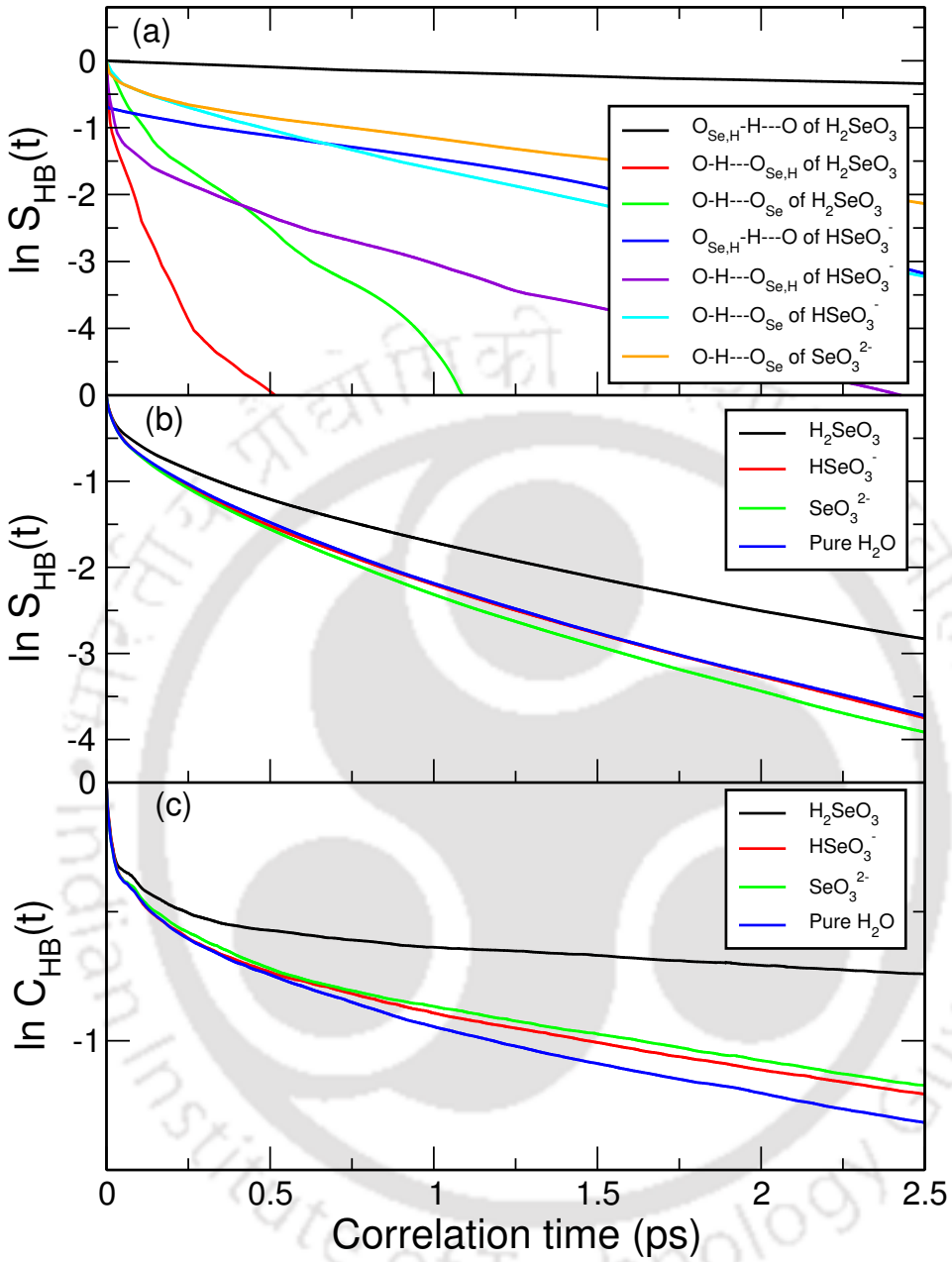

Figure 4.8: ((a) Comparisons of H-bond lifetime correlation functions, $S_{\mathrm{HB}}(t)$, for various solute-solvent H-bonds, (b) those for solvent H-bonds, (c) structural relaxation correlation functions, $C_{\mathrm{HB}}(t)$, for solvent H-bonds in comparison to pure H_2O H-bonds.

Fig. 4.8(a) shows the lifetime correlation function $S_{\mathrm{HB}}(t)$ for various solute–solvent H-bonds. As listed in Table 4.1, the corresponding characteristic time scales (by fitting to the linear regime) provide the estimate for the lifetimes of these H-bonds. However, being averaged over only a few pairs, the estimates in Table 4.1 are subject to large

Table 4.1: H-bond continuous correlation function characteristic decay times τ_s for different solute–solvent intermolecular H-bonds (represented as donor-hydrogen$\cdots$acceptor) obtained from CPMD simulations at 315 K

System	H-bond type	τ_s(ps)
H_2SeO_3	$O_{Se,H}-H\cdots O$	3.11
	$O-H\cdots O_{Se,H}$	0.14
	$O-H\cdots O_{Se}$	0.22
$HSeO_3^-$	$O_{Se,H}-H\cdots O$	0.74
	$O-H\cdots O_{Se,H}$	0.66
	$O-H\cdots O_{Se}$	1.14
SeO_3^{2-}	$O-H\cdots O_{Se}$	1.52

statistical errors, thus they serve only as indicators.

The solute-solvent H-bonds differ remarkably across the aqueous systems of H_2SeO_3, $HSeO_3^-$ and SeO_3^{2-} depending on the atomic site of the species, and whether they are donated or accepted in nature. H-bonds donated by H_2SeO_3 are of long lifetimes, although it forms very weak H-bonds as an acceptor. $HSeO_3^-$ on the other hand forms relatively stronger H-bonds, in terms of their lifetime, both as a donor as well as an acceptor. SeO_3^{2-} forms the strongest H-bonds as an acceptor. Fig. 4.8(b) and 4.8(c) illustrate the lifetime and structural relaxation of water–water H-bonds, computed for solutions of H_2SeO_3, $HSeO_3^-$ and SeO_3^{2-} along with those of pure H_2O. The corresponding characteristic time scales are listed in Table 4.1. Remarkably, the water dissolving H_2SeO_3 species exhibits slow structural relaxation and long H-bond lifetimes compared to that of pure H_2O. The behavior of water dissolving H_2SeO_3 and SeO_3^{2-} species is quite similar to that of pure water. This feature is consistent with the picture of a more structured solvent around H_2SeO_3, evidenced also in the $O-O$ RDFs (Fig. 4.4(c)), and in the number of water-water H-bonds (Fig. 4.7) for this system. This suggests that noticeable differences in the bulk transport properties, such as the viscosity (for the water dissolving H_2SeO_3) may be expected.

The orientational correlation functions for different solvent-water molecules, $C_2(t)$, defined in chapter 2, with the vector $\vec{v}$ chosen to be the OH vectors of H_2O molecules, is shown in Fig 4.9. As for the H-bond correlations, $C_{HB}(t)$, the characteristic decay constant are estimated by fitting to single exponentials over the region between $0.5-3.5$ ps, for sake of simplicity. The relaxation times of solvent water molecules for the different As-V species are also tabulated in table 4.2, as the 4^{th} column. The experimental values

of H_2O orientational relaxation lies around 1.7-2.6 ps [7–9], while MD simulations have generally over-estimated the values [8–14]. Previous literature suggests that these values are sensitive to the computational techniques adopted, such as the density functional employed, fitting procedure, statistics, etc [8, 9, 12–14].

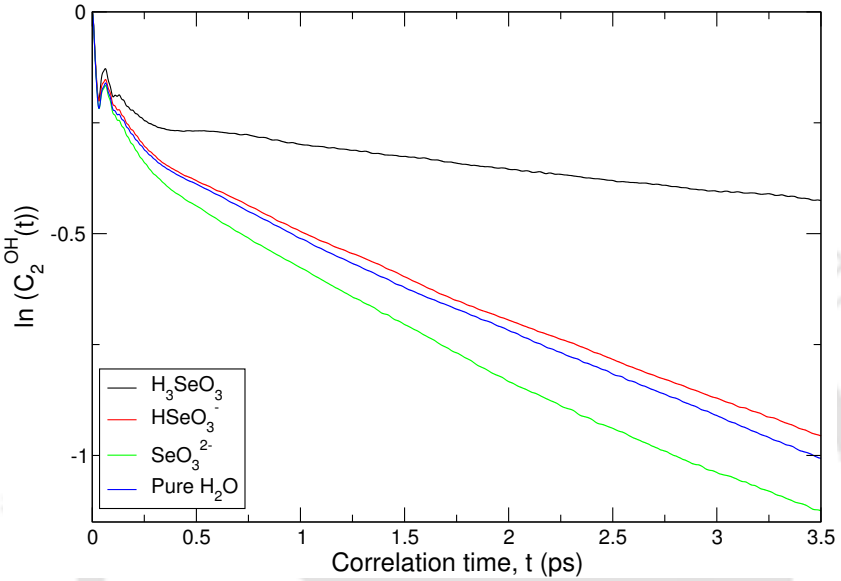

Figure 4.9: Orientational correlation functions, calculated for H_2O molecules along the vector OH.

Table 4.2: The estimated lifetimes and structural relaxation times of the H-bonds, τ_s and τ_c of the solvent water molecules, respectively from $S_{HB}(t)$ and $C_{HB}(t)$ in Fig. 4.8(b) and 4.8(c). The 4^{th} column provides the orientational relaxation times, τ_2^{OH} of H_2O molecules.

Solute	τ_s(ps)	τ_c (ps)	τ_2^{OH}(ps)
H_2SeO_3	1.65	16.42	18.52
$HSeO_3^-$	0.89	5.44	5.16
SeO_3^{2-}	0.79	4.92	4.16
Pure H_2O	0.88	5.42	4.86

Fig. 4.9 and table 4.2 suggest that waters dissolving Se – IV species exhibit somewhat different orientational relaxation compared to pure water, the slowest being noted for the case of H_2SeO_3, while SeO_3^{2-} shows the fastest relaxation among others. It has been noted earlier that these relaxation are sensitive to the presence of ions in the environment, particularly the dipole moment and polarizabilities of the solutes, in addition to external influences, such as temperature and pressure [12, 15–17, 17–22]. Bursulaya et. al.[15] showed that the increase of dipole moment of the solutes slows

down the orientational relaxation of solutes. For that we computed the dipole moments for the various Se–IV species in gas phases, which are found to be 0.66 D, 1.81 D and 0.71 D, respectively for H_2SeO_3, $HSeO_3^-$ and SeO_3^{2-}, in comparison to H_2O for which dipole moment is found to be 1.81 D. Thus, dipole moment of H_2SeO_3 is low, and hence may not be playing a critical role in structural relaxation and higher lifetime of waters, shown in Fig. 4.8. This result, is in contrast to the case of $H_2AsO_4^-$, to be discussed in the next chapter, which has a dipole moment of 3.80 D, much higher than waters (1.81 D). Thus, at the expense of the overall loss of H-bonds (both in numbers as well as overall lifetimes) leading to a relatively less-structured hydration shell, the solvent waters in presence of H_2SeO_3 become over-structured (noted earlier in the O–O rdf in Fig. 4.4(c)) by forming more H-bonds among themselves. These are more in number as compared to pure water, also exhibits higher lifetimes, structural and orientational relaxations.

It is known that the presence of hydronium (H_3O^+) and hydroxide (OH^-) ions in aqueous solutions impact the overall dynamics of the solution [23–27]. Previous AIMD simulations have shown an anomalously higher mobility of these species compared to H_2O molecules through proton transfer mediated through the H-bond network [28–30]. The H-bonding characteristics of these species also differ significantly from H_2O molecules. In the present study of Se–IV solution, each H_3O^+ is found to donate 2.98 H-bonds on average, but accepts none, possibly due to *steric* factors. This is in agreement with previous studies [28]. The lifetime of these H-bonds is found to be smaller by an order of magnitude for H_2O in pure bulk water (for an estimate respectively 0.063 ps and 0.88 ps). The number of H-bonds formed by OH^- is found to be 3.91 as an acceptor and 0.51 as a donor. Thus, by and large, the oxygen of the hydroxide ions coordinates with four water molecules most of the time. Meanwhile its hydrogen less actively participates in H-bonds compared to that of H_2O molecules in pure water. This is in good agreement with the findings of Ma and Tuckerman [21], where an explicit population analysis of 3-, 4- and 5-coordinated oxygen of OH^- (that is, H-bond acceptance of OH^-) against its H-bond donation tendency is detailed. The lifetime estimates for H-bonds donated and accepted by OH^- are respectively 0.15 ps and 0.63 ps.

4.3.5 Vibrational Density of States

The vibrational density of states (VDOS) of H_2SeO_3, $HSeO_3^-$ and SeO_3^{2-} species in aqueous environment is calculated using the Fourier transform velocity autocorrelation

Table 4.3: Gas phase frequencies of H_2SeO_3 along with a qualitative description of vibrational modes

Serial no.	Frequency (cm^{-1})	Description
1 - 5	139, 259, 325, 350, 354	Various bending modes
6	575	Asymmetric stretching of $Se - O_{Se,H}$
7	599	Symmetric stretching of $Se - O_{Se,H}$
8	938	Stretching of $Se - O_{Se}$
9 - 10	965, 1009	Of mixed nature involving $Se - O_{Se,H} - H$ bending as well as $O_{Se,H} - H$ stretching
11	3613	Asymmetric stretching of $O_{Se,H} - H$
12	3615	Symmetric stretching of $O_{Se,H} - H$

function (VACF), as shown in Fig. 4.10. The gas-phase vibrational modes for the species are also shown in Fig. 4.10, duplicated in both panels, as triangles (black for H_2SeO_3, red for $HSeO_3^-$ and orange for SeO_3^{2-}) to facilitate useful comparison. A qualitative description based on the visualization of the Eigen modes of H_2SeO_3, taken as a prototype, is listed in Table 3. In Fig. 4.10(a), the VDOS of H atoms of the solutes is compared to that of pure water. $O_{Se,H} - H$ stretching modes, spreading over the range 2000–3300 cm^{-1}, are significantly red-shifted with respect to the gas-phase frequencies as well as that of pure water owing to the relatively stronger nature of H-bonds donated to surrounding H_2O molecules. The effect is more pronounced for H_2SeO_3 than for $HSeO_3^-$ as the donated H-bonds of the species are stronger than those of $HSeO_3^-$, as seen earlier. Comparing with Table 4.3 the large intensity, spreading over 900–1300 cm^{-1} in the hydrogen VDOS, is attributed to $Se - O_{Se,H} - H$ bending modes. The spectra for water dissolving the selenium species, H_2SeO_3, $HSeO_3^-$ and SeO_3^{2-} are found to be very similar (not shown) to that of pure water.

Fig. 4.10(b) illustrates the VDOS calculated for the different oxygen atoms of the selenium species. The $Se - O$ stretching frequencies are found to spread over 400–900 cm^{-1} across the species in aqueous environment. The stretching modes of $O_{Se,H}$ (bearing hydrogen) are observed to be more red-shifted in $HSeO_3^-$ than in H_2SeO_3, despite the fact that H-bonds donated by the latter are relatively stronger. This is attributed to the stronger nature as well as the larger number of H-bonds accepted by the former (Fig. 13). The $Se - O_{Se}$ stretching modes of SeO_3^{2-} are of lowest frequencies in the series, but are less affected in aqueous environment relative to their gas phase frequencies. The intensity in the oxygen VDOS spreading over 200–400 cm^{-1} is attributed to various $O - Se - O$ bending modes. The intensity below 150 cm^{-1} is due to various rigid body-like

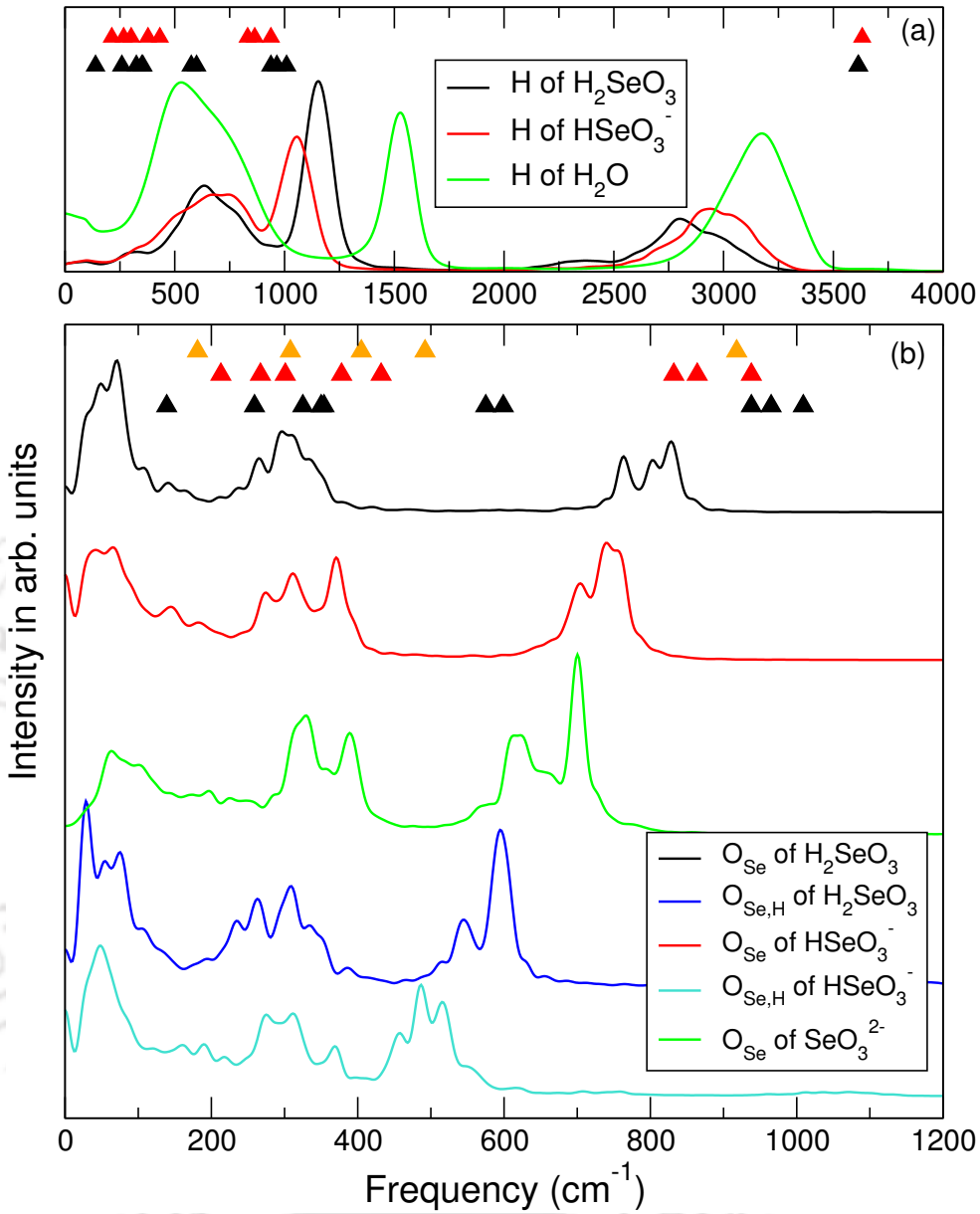

Figure 4.10: (a) Power spectra of vibrational modes calculated by taking the Fourier transform velocity autocorrelation function (VACF) of the atomic species for different (a) hydrogen and (b) oxygen atoms from the present study. The gas-phase vibrational modes of Se(IV) species are shown as triangles (black for H_2SeO_3, red for $HSeO_3^-$ and orange SeO_3^{2-}), in both panels for ease of comparison.

tumbling modes of the solutes in the hydration cages of surrounding water molecules. The predicted frequencies are found to be in good qualitative agreement with previous experimental studies [31–33].

4.4 Conclusions

The microscopic features of structure, hydrogen bonding and vibrational signatures of Se(IV) species, H_2SeO_3, $HSeO_3^-$ and SeO_3^{2-}, in aqueous environment are comprehensively investigated employing *ab initio* molecular dynamics. In neutral aqueous solution H_2SeO_3 and $HSeO_3^-$ engage in a dynamic equilibrium, with the species exchanging protons with the surrounding water molecules, consistent with the low pK_{a1} of 2.62. The SeO_3^{2-} species is found to be unstable in neutral water, as it absorbs a proton from the solvent molecule forming $HSeO_3^-$. However, in a basic environment, with the introduction of a hydroxide ion, the SeO_3^{2-} species stabilizes. The compactness of the hydration shell around the solute species is found to improve across the series, H_2SeO_3, $HSeO_3^-$ and SeO_3^{2-}. The total number of hydrogen bonds formed by the species with water as well as their lifetimes generally follow this trend. The hydrogen bonds donated by H_2SeO_3 and $HSeO_3^-$ are stronger in terms of their lifetime estimates. The lifetimes as well as the number of hydrogen bonds accepted by the species increase with the increase in the effective charge of the solute, that is, in favour of the SeO_3^{2-} species. Interestingly, the compactness of the hydration structure is found to have a noticeable impact on the solvent structure. The relatively loose hydration structure of H_2SeO_3 prompts a some- what over-structured water medium compared to the solutions of the other two selenium species as well as that of pure water. The impact on the dynamic responses is more pronounced, with a remarkable increase in the lifetime of H-bonds and a slower structural relaxation of water dissolving H_2SeO_3 being observed. The $O-H$ stretching frequencies of the solutes are significantly red-shifted with water owing to the stronger nature of H-bonds donated to the surrounding medium. The $Se-O$ stretching modes of the species, typically spread over $400-900$ cm^{-1}, also generally exhibit red shifts but less dramatically compared to $O-H$ stretching modes.

BIBLIOGRAPHY

[1] Lars Eklund and Ingmar Persson. Structure and hydrogen bonding of the hydrated selenite and selenate ions in aqueous solution. *Dalton Trans.*, 43(17):6315–6321, 2014.

[2] Peter D Jensen, Maria D Rivas, and John T Trumble. Developmental responses of a terrestrial insect detritivore, megaselia scalaris (loew) to four selenium species. *Ecotoxicology*, 14(3):313, 2005.

[3] Laurence M Cummins and Eugene T Kimura. Safety evaluation of selenium sulfide antidandruff shampoos. *Toxicol. Appl. Pharmacol.*, 20(1):89–96, 1971.

[4] Mustafa Tuzen and Ahmet Sarı. Biosorption of selenium from aqueous solution by green algae (cladophora hutchinsiae) biomass: equilibrium, thermodynamic and kinetic studies. *Chem. Eng. J.*, 158(2):200–206, 2010.

[5] Sílvia Santos, Gabriela Ungureanu, Rui Boaventura, and Cidália Botelho. Selenium contaminated waters: an overview of analytical methods, treatment options and recent advances in sorption methods. *Sci. Total. Environ.*, 521:246–260, 2015.

[6] Glenn J Martyna and Mark E Tuckerman. A reciprocal space based method for treating long range interactions in ab initio and force-field-based calculations in clusters. *J. Chem. Phys.*, 110(6):2810–2821, 1999.

[7] FK Vansant, BJ Van Der Veken, and HO Desseyn. Vibrational analysis of arsenic acid and its anions: I. description of the raman spectra. *J. Mol. Structure*, 15(3):425–437, 1973.

[8] Michiel Sprik, Jürg Hutter, and Michele Parrinello. Ab initio molecular dynamics simulation of liquid water: Comparison of three gradient-corrected density functionals. *J. Chem. Phys.*, 105(3):1142–1152, 1996.

[9] David E Smith and Liem X Dang. Computer simulations of nacl association in polarizable water. *J. Chem. Phys.*, 100(5):3757–3766, 1994.

[10] Bhabani S Mallik, A Semparithi, and Amalendu Chandra. Vibrational spectral diffusion and hydrogen bond dynamics in heavy water from first principles. *J.Phys. Chem. A*, 112(23):5104–5112, 2008.

[11] Ashu Choudhary and Amalendu Chandra. Anisotropic structure and dynamics of the solvation shell of a benzene solute in liquid water from ab initio molecular dynamics simulations. *Phys. Chem. Chem. Phys.*, 18(8):6132–6145, 2016.

[12] Amalendu Chandra. Effects of ion atmosphere on hydrogen-bond dynamics in aqueous electrolyte solutions. *Phys Rev Lett*, 85(4):768, 2000.

[13] Damien Laage and James T Hynes. A molecular jump mechanism of water reorientation. *Science*, 311(5762):832–835, 2006.

[14] Jean Boisson, Guillaume Stirnemann, Damien Laage, and James T Hynes. Water reorientation

dynamics in the first hydration shells of f- and i-. *Phys. Chem. Chem. Phys.*, 13(44):19895–19901, 2011.

[15] Badry D Bursulaya, Dominic A Zichi, and Hyung J Kim. Molecular dynamics simulation study of polarizable solute solvation in water. 1. equilibrium solvent structure and solute rotational dynamics. *J. Phys. Chem.*, 100(4):1392–1405, 1996.

[16] Henry S Frank and Wen-Yang Wen. Ion-solvent interaction. structural aspects of ion-solvent interaction in aqueous solutions: a suggested picture of water structure. *Discuss. Faraday Soc.*, 24:133–140, 1957.

[17] Yizhak Marcus. Effect of ions on the structure of water: structure making and breaking. *Chem. Rev.*, 109(3):1346–1370, 2009.

[18] Badry D Bursulaya, Dominic A Zichi, and Hyung J Kim. Role of solute electronic polarizability in solvation dynamics. *J. Phys. Chem.*, 99(25):10069–10074, 1995.

[19] Albert J Cross and John D Simon. Rotational dynamics of a solvated dipole: A molecular dynamics study of dielectric friction. *J. Chem. Phys.*, 86(12):7079–7083, 1987.

[20] A Geiger. Molecular dynamics simulation study of the negative hydration effect in aqueous electrolyte solutions. *Ber. Bunsenges. Phys. Chem.*, 85(1):52–63, 1981.

[21] Zhonghua Ma and Mark E Tuckerman. On the connection between proton transport, structural diffusion, and reorientation of the hydrated hydroxide ion as a function of temperature. *Chem. Phys. Lett.*, 511(4):177–182, 2011.

[22] Badry D Bursulaya, Jonggu Jeon, Dominic A Zichi, and Hyung J Kim. Generalized molecular mechanics including quantum electronic structure variation of polar solvents. ii. a molecular dynamics simulation study of water. *J. Chem. Phys.*, 108(8):3286–3295, 1998.

[23] Noam Agmon, Huib J. Bakker, R. Kramer Campen, Richard H. Henchman, Peter Pohl, Sylvie Roke, Martin Thämer, and Ali Hassanali. Protons and Hydroxide Ions in Aqueous Systems. *Chem. Rev.*, 116(13):7642–7672, 2016.

[24] Ali A Hassanali, Jérôme Cuny, Vincenzo Verdolino, and Michele Parrinello. Aqueous solutions: state of the art in ab initio molecular dynamics. *Philos. Trans. R. Soc.*, 372(2011):20120482–20120482, 2014.

[25] Dominik Marx, Amalendu Chandra, and Mark E Tuckerman. Aqueous basic solutions: hydroxide solvation, structural diffusion, and comparison to the hydrated proton. *Chem. Rev.*, 110(4):2174–2216, 2010.

[26] Mark E. Tuckerman, Amalendu Chandra, and Dominik Marx. Structure and dynamics of OH - (aq). *Acc. Chem. Res.*, 39(2):151–158, 2006.

[27] Mark E Tuckerman, Dominik Marx, and Michele Parrinello. The nature and transport mechanism of hydrated hydroxide ions in aqueous solution. *Nature*, 417(6892):925–929, 2002.

[28] Dominik Marx, Mark E Tuckerman, Jürg Hutter, and Michele Parrinello. The nature of the hydrated excess proton in water. *Nature*, 397(6720):601–604, 1999.

[29] Mark Tuckerman, Kari Laasonen, Michiel Sprik, and Michele Parrinello. Ab initio molecular dynamics simulation of the solvation and transport of h3o+ and oh-ions in water. *J. Phys. Chem.*, 99(16):5749–5752, 1995.

[30] Dominik Marx. Proton transfer 200 years after Von Grotthuss: Insights from ab initio simulations. *ChemPhysChem*, 7(9):1849–1870, 2006.

[31] Michael Falk and Paul A Giguère. Infrared spectra and structure of selenious acid. *Can. J. Chem.*, 36(12):1680–1685, 1958.

[32] CA Cody, RC Levitt, Rampur S Viswanath, and Philip J Miller. Vibrational spectra of alkali hydrogen selenites, selenous acid, and their deuterated analogs. *J. Solid State Chem.*, 26(3):281–291, 1978.

[33] RK Khanna, JC Decius, and ER Lippincott. Infrared-absorption spectrum and ferroelectric behavior of sodium trihydroselenite. *J. Chem. Phys.*, 43(9):2974–2979, 1965.

CHAPTER 5

AIMD STUDY OF WATERBORNE AS – V SPECIES

5.1 Introduction

Arsenic is mostly found in aqueous environment in As – V and As – III states. The parent form of As – V is the arsenic acid, H_3AsO_4, which is a weak acid with experimentally reported pK_{a1} value of 2.25 [1]. Its deprotonated forms namely $H_2AsO_4^-$ and $HAsO_4^{2-}$ are very weak acids with $pK_{a2} = 7.05$ and $pK_{a2} = 11.58$ [1].

$$H_3AsO_4 \xrightarrow[2.25]{pK_{a1}} H_2AsO_4^- \xrightarrow[7.05]{pK_{a2}} HAsO_4^{2-} \xrightarrow[11.58]{pK_{a3}} AsO_4^{3-} \tag{5.1}$$

The structure and spectroscopic aspects of various hydrated As – V species have been recently probed experimentally employing large angle X-ray scattering (LAXS), EXAFS and double difference infrared (DDIR) spectroscopy by Mähler et al [1]. An *ab initio* quantum mechanical charge field molecular dynamics (QMCF-MD) study had been conducted by Bhattacharjee et al. [2] to characterize the structure and spectroscopic natures of solvated $HAsO_4^{2-}$ species.

The work presented in this chapter details *ab initio* molecular dynamics simulation studies of arsenic acid (H_3AsO_4) and its deprotonated derivatives viz. $H_2AsO_4^-$, $HAsO_4^{2-}$ and AsO_4^{3-} in aqueous environment. Fresh microscopic insights on the hydra-

An article based on this chapter is published in *J. Phys. Chem. B*, vol. **122**(12), year 2018, pages 3153-3162; title: "First-Principle Molecular Dynamics Investigation of Waterborne As – V Species"; authors Sangkha Borah and P. Padma Kumar. Selected contents are reproduced with permission ©American Chemical Society 2018.

tion structure, nature of hydrogen-bonding (H-bonding) and vibrational properties of these species have been presented comprehensively.

5.2 Methods

Four sets of CPMD simulations have been carried out at 315 K temperature on various As – V species, namely (i) H_3AsO_4, (ii) $H_2AsO_4^-$, (iii) $HAsO_4^{2-}$ and (iv)AsO_4^{3-}, solvated by 60 H_2O molecules in a simulation box of length 12.42 Å, corresponding to the density of about 1.05 g/cc. All simulations are performed using the gradient-corrected, norm-conserving, Martin-Troullier (MT) type pseudo-potentials employing Becke [3] Lee-Yang-Parr[4] (B-LYP) exchange and correlation functionals [5]. The Kohn-Sham orbitals are expanded in plane-wave basis up to a cut-off of 85 Ry. Simulations are carried out in NVT ensemble with the electronic as well as ionic degrees of freedom controlled using Nose-Hoover thermostats [6–8]. The fictitious kinetic energy of electrons are maintained at 0.03 au, employing an electron mass of 600 au [5, 9, 10]. A time step of 0.1 fs is used for integration of equations of motion. The trajectories printed at every 5 MD steps, during the production phases, are subjected to detailed analysis discussed below.

The H_3AsO_4+60H_2O system is prepared from a well equilibrated configuration of H_2SeO_4+H_2O employed in a previous study, details of which are discussed in chapter 3. This initial structure is optimized for geometry, and further equilibrated for 50 ps using AIMD scheme. An additional 80 ps run is analyzed for detailed structural and dynamical properties. The other systems, involving $H_2AsO_4^-$, $HAsO_4^{2-}$ and AsO_4^{3-} species solvated by 60 H_2O molecules, are prepared from the final structure of H_3AsO_4 system simulated earlier. Each of these systems are further geometry optimized and equilibrated for 30-50 ps, before 50-80 ps of production runs are carried out.

Additionally, the geometry optimized gas-phase molecular structures are obtained for all of the As – V species, H_3AsO_4, $H_2AsO_4^-$, $HAsO_4^{2-}$ and AsO_4^{3-}, of the same level of theory, for making useful comparisons. Normal-mode analysis of H_3AsO_4 is carried out about its geometry optimized gas-phase structure [11, 12]. Further, dipole moments of H_3AsO_4, $H_2AsO_4^-$, $HAsO_4^{2-}$ and AsO_4^{3-} molecules in gas phase have been computed from the optimized structures, at the same theoretical level employing CPMD package [13]. A Born-Oppenheimer molecular dynamics (BOMD) simulation run of 10 ps have also been conducted at 315 K starting from a well equilibrated structure of one H_3AsO_4 solvated by 60 H_2O molecules in box of size 12.42 Å employing the CPMD software

package. The time step of integration for BOMD simulation is 0.25 fs. The trajectories for the final 6 pico-seconds runs have been used for the calculation of vibrational density of states.

For convenience of description, we shall use the label O_{As} for the oxygens of the As species not bonded to hydrogen, and $As-O_{As,H}$ for those bonded to hydrogen. The hydrogens and oxygens of H_2O will be labeled as H and O respectively.

5.3 Results and Discussions

5.3.1 Molecular Structure

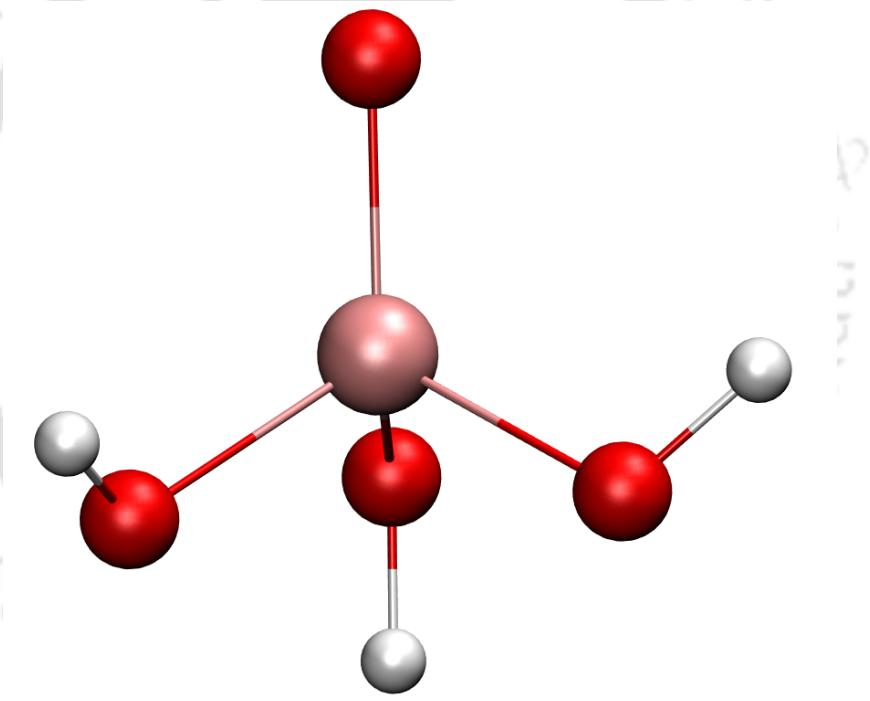

Figure 5.1: Gas phase geometry optimized structure of H_3AsO_4.

Fig. 5.1 shows the DFT optimized structure of H_3AsO_4. The central As atom is bonded to four oxygen atoms, among which three are bonded to hydrogens ($O_{As,H}-H$), thus forming one $As=O_{As}$ double bond and three $As-O_{As,H}$ single bonds, as shown in the figure. The $As=O_{As}$ bond length thus obtained is 1.57 Å, while $As-O_{As,H}$ single bonds measure ~ 1.71 Å. The $O_{As}-As-O_{As,H}$ angles measures about 115°, while the $O_{As,H}-As-O_{As,H}$ angles are around 100°. The three $As-O_{As,H}-H$ angles are around 110°. Table 5.1

Table 5.1: Comparison of $As-O_{As}$ and $As-O_{As,H}$ bond-lengths for the As–V species, in aqueous and gas phases to available experimental studies in crystalline phases [1]

Species	Type	Solution (Å)	Gas(Å)	Expt. (Å)
H_3AsO_4	$As-O_{As-H}$	1.69	1.71	1.69
	$As-O_{As}$	1.61	1.57	1.64
$H_2AsO_4^-$	$As-O_{As-H}$	1.71	1.77	1.71
	$As-O_{As}$	1.63	1.61	1.66
$HAsO_4^{2-}$	$As-O_{As-H}$	1.74	1.87	1.74
	$As-O_{As}$	1.64	1.64	1.67
AsO_4^{3-}	$As-O_{As}$	1.67	1.67	1.70

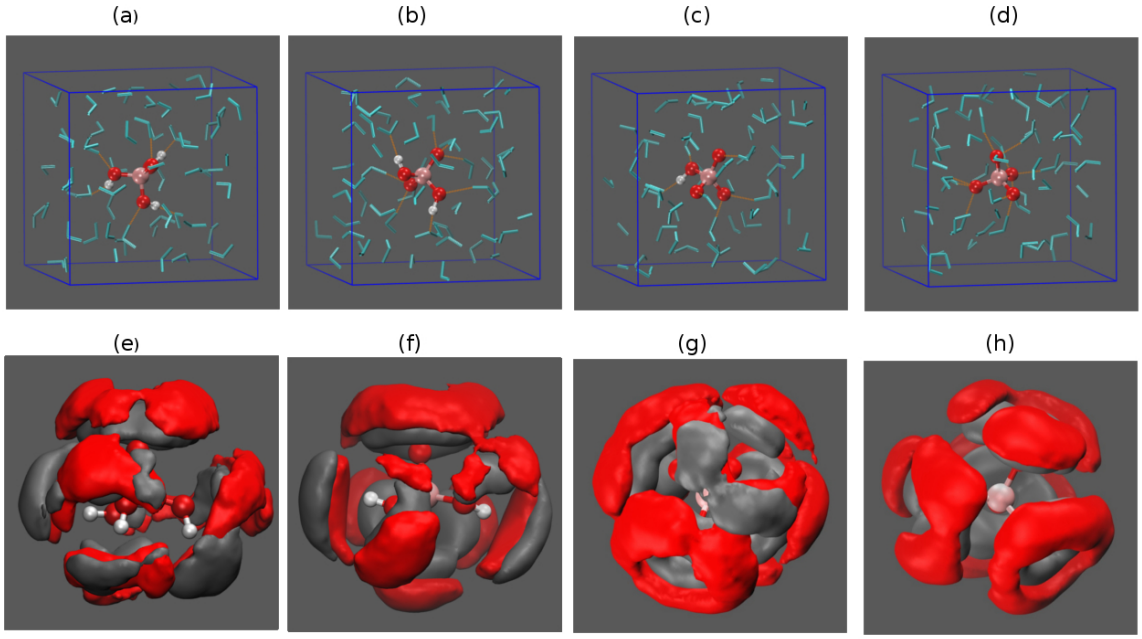

Figure 5.2: (a-d) Snapshots of As–V species viz., (a) H_3AsO_4 (b) $H_2AsO_4^-$ (c) $HAsO_4^{2-}$ and (d) AsO_4^{3-} in aqueous environment, from CPMD simulations at 315 K. The solvent water molecules are rendered by the "stick"-model in cyan, and the solute species by "ball-and-stick"-model. (e)-(h) The hydration structures of the species is visualized through their spatial density distributions (SDD) averaged over the CPMD trajectory, where oxygens of water is rendered in red and hydrogens in gray, around the solute.

presents the $As-O_{As}$ bond lengths for H_3AsO_4, $H_2AsO_4^-$, $HAsO_4^{2-}$ and AsO_4^{3-} obtained from CPMD studies in aqueous environment at 315 K, along with the ones obtained from gas phase calculations. Evidently, the $As-O_{As,H}$ bond-lengths are longer than $As-O_{As}$ across the species, and in all three phases. A systematic increase in the Arsenic-Oxygen bond-lengths with the effective charge of the species is also evident. These results from simulation are in overall consistency with the previous experimental

studies carried out in the crystalline phases (see the article by Mähler et al. [1] and the supplementary of the paper).

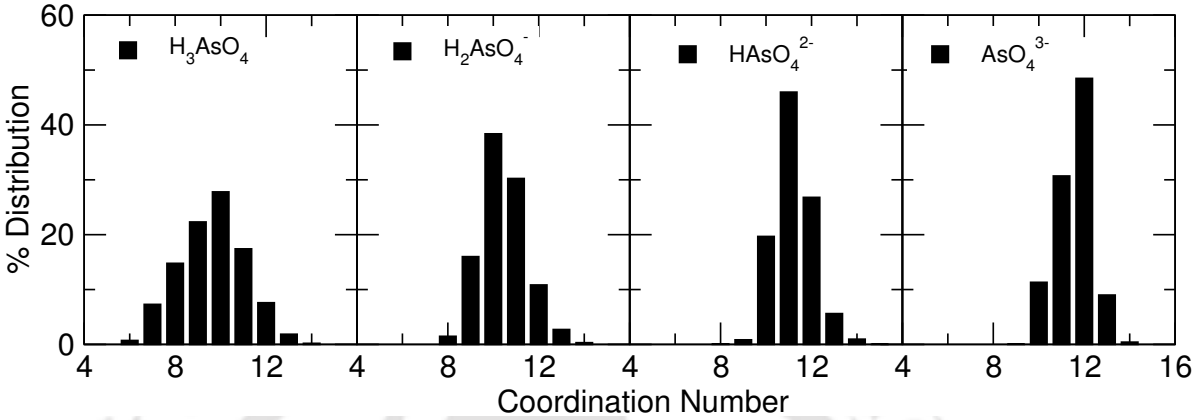

Figure 5.3: Coordination number distribution (in percentage) for (a) H_3AsO_4, (b) $H_2AsO_4^-$, (c) $HAsO_4^{2-}$ and (d) AsO_4^{3-}

5.3.2 Hydration Structure

We have observed a few protonation and deprotonation events, $H_3AsO_4 + H_2O \rightleftharpoons H_2AsO_4^- + H_3O^+$ during the course of 80 ps production run, with qualitatively consistency with its reported pK_{a1} value of 2.25 [1]. The deprotonated state lasted only for a few ps, as the $H_2AsO_4^-$ is not found to be stable in the highly acidic environment due to the presence of the H_3O^+ produced. It shall be noted that the presence of one H_3O^+ in 59 other H_2O molecules amounts to a pH of about 0.06, significantly lower than the experimental pK_{a1} value of 2.25. This results the equilibrium shifted heavily towards the H_3AsO_4 species. Thus, it is not possible to investigate with sufficient accuracy the deprotonation events for As – V species within the length- (or, system size) and time-scales of the present study. Aqueous $H_2AsO_4^-$ and $HAsO_4^{2-}$ did not exhibit any protonation-deprotonation events during the simulation runs owing to the high dissociation constants, $pK_{a2} = 7.05$ and $pK_{a3} = 11.58$ [1]. However, aqueous AsO_4^{3-} exhibited, within the 80 ps of production runs, a few instances of proton transfer, $AsO_4^{3-} + H_2O \rightleftharpoons HAsO_4^{2-} + OH^-$, lasting for a few fs, which is consistent with its pK_{a3} of 11.58 [1].

Fig. 5.2 (a)-(d) show typical snapshots of the simulated systems with waters represented with the “stick”-model in cyan, and the solute species in “ball-and-stick” representations. AIMD studies carried out on these systems reveal the important dissimilarities in their solvation structures, shown respectively in Fig.5.2 (e)-(h) through the three

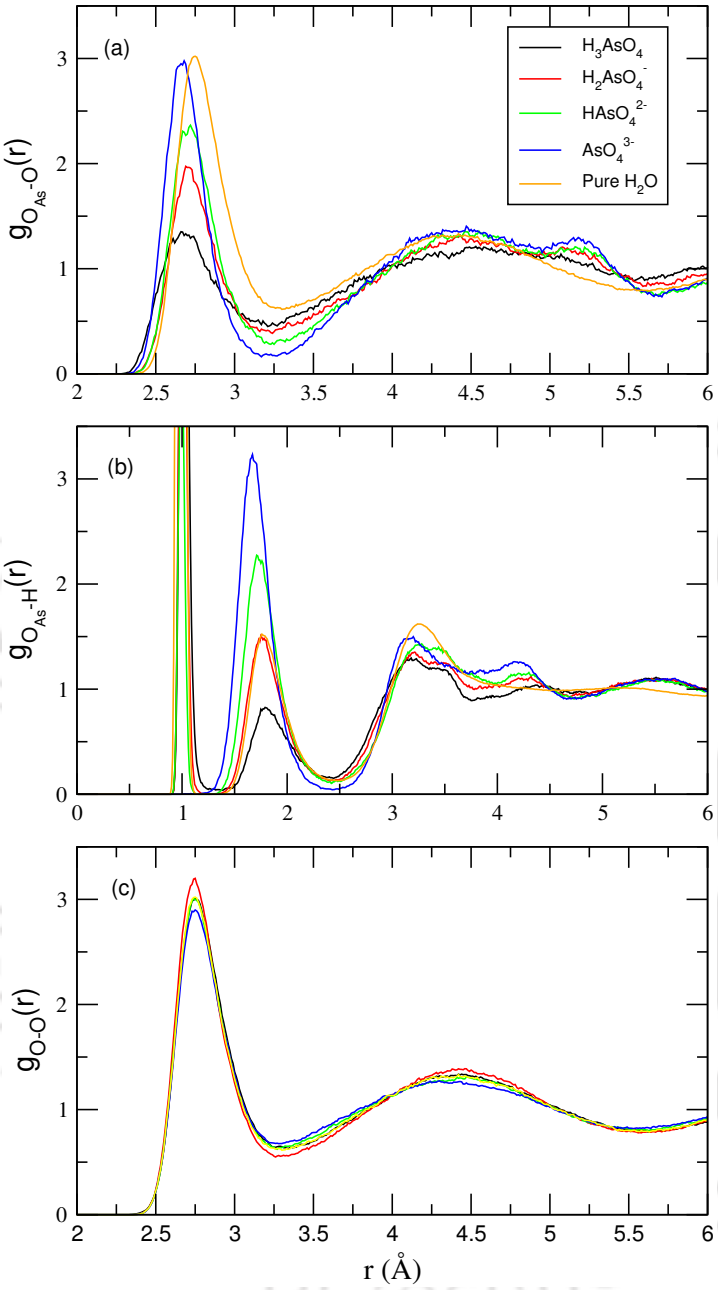

Figure 5.4: Radial distribution functions (RDF) (a) between Oxygens of the solute (O_{As} and $O_{As,H}$) and water, and (b) Hydrogens of the solute (H) and water, are compared to the O–O and O–H RDFs for pure water, from CPMD trajectories at 315 K. (c) shows the O–O RDFs for water dissolving the different As–V species.

dimensional Spatial Density Distribution (SDD) plots. These are generated by transforming the coordinates of the solvent molecules, frame by frame, to a selected body fixed axis of the solute species and averaged over the entire stored trajectory. These are

calculated using the TRAVIS software package [14]. Only those water molecules within the first hydration shell are shown, omitting those beyond the distance, as in criterion (i) and (ii) of the H-bond definition discussed in the methods section. The iso-density surfaces, in Fig.5.2, are plotted for a value of 0.04 $Å^{-3}$, with those for the hydrogens of water molecules in gray and oxygens in red. The SDD plots clearly suggest a systematic increase in the organization of the solvent molecules across the species, starting from H_3AsO_4 to AsO_4^{3-}. Fig. 5.3 shows the coordination number distribution (in percentage) of the solvents within 3.5 Å of oxygens of the solutes. These plots, in addition, gives the measure of the fluctuations in hydration shell of the solutes. It can be observed from these plots that there is a systematic reduction of the fluctuation in hydration shells across the series, consistent with the 5.2 plots.

5.3.3 Hydrogen-bonding

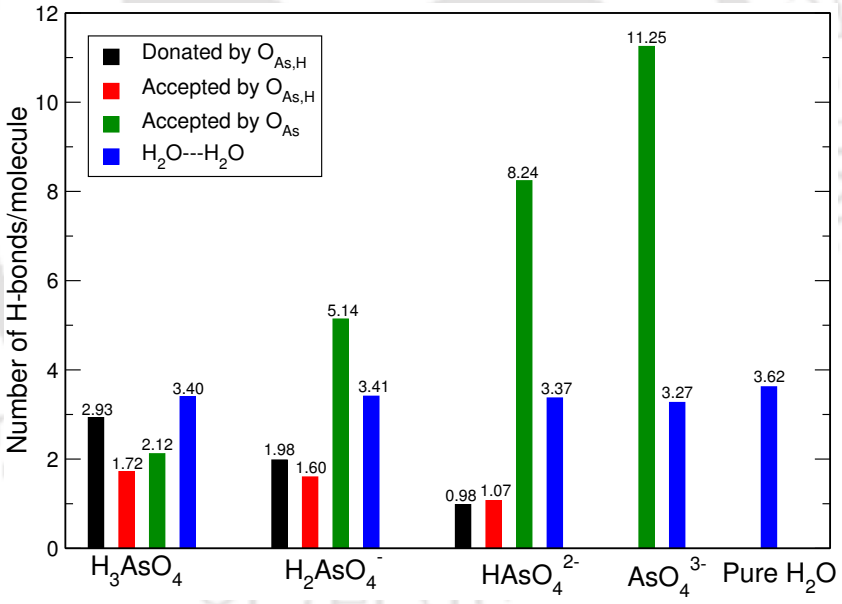

Figure 5.5: Number of H-bonds (computed based H-bonding criteria described in chapter 2) formed by the solute species are shown, along with those for bulk waters. H-bonds donated by $O_{As,H}$ are shown as black bars, accepted ones as red, while those accepted by O_{As} are shown as green colored bars. $H_2O\cdots H_2O$ H-bonds are shown as blue bars.

Fig. 5.4(a) shows the radial distribution functions (RDFs) of O of water molecules with respect to oxygen of the As–V species (without distinguishing between O_{As} and $O_{As,H}$), along with the O–O RDF for pure waters for comparison. The intensities of the 1^{st} peaks in the O_{As}–O RDFs show a systematic increase with the formal charge of the solute

species. The minima following the first peaks also show systematic decrease suggesting that with the increase in the formal charge of the solute species hydration shells become more compact. Fig.5.4(b) presents the corresponding $O_{As}-H$ RDFs which are calculated without distinguishing the intra-molecular and inter-molecular hydrogens. Thus, the first peaks around 1 Å may be identified with the intra-molecular hydrogens of the As – V species, and the second peaks constitute the H-bonded hydrogens of the surrounding water molecules. Again, as in the $O_{As}-O$ RDFs, the peak heights, or more appropriately the area under the peak, show a systematic increase with the charge of the As – V species. The higher first peak of solute-solvent RDFs (Fig.5.4(a) and (b)) followed by a deeper minimum for AsO_4^{3-} is suggestive of its compact, well defined hydration structure. These are in good qualitative agreement with the SDD plots shown in Fig. 5.2(e)-(h), and the hydrogen bond statistics presented later in this section.

Interestingly, both RDFs of all the As – V species reflect distinct intensities even beyond the second hydration shells (spread over 5-5.5 Å in $O_{As}-O$ and 4-4.5 Å in $O_{As}-H$ RDFs), contrasting to those of pure water. This suggests significant orientational organization of water molecules around the As – V species radially extending up to three hydration shells. A qualitative idea about the comparative stabilities and residence times of water molecules within the solvation shell can be predicted from these behaviors. It also leads to a considerable difference in H-bond numbers across the species as well as of solvent waters. It also predicts that, for the last three species, the effects of hydration are liable to extend beyond the first hydration shells and thus show considerably more hydrophilic characters, as discussed below.

The O – O RDFs of the water molecules in the presence of different As – V species shown in Fig.5.4(c) presents interesting aspects on the influence of the solute on the solvent structure. The solvent RDFs for the cases of H_3AsO_4 and $HAsO_4^{2-}$ are found to be qualitatively very similar with that of pure H_2O. However, O – O RDFs for $H_2AsO_4^-$ exhibits higher maxima and lower minima, predicting more ordered water structure. The corresponding RDF for the AsO_4^{3-} case is found to have the shorter peak and a shallow minima following it, thus the more compact, well developed hydration structure of this species observed earlier has an adverse effect on its solvent structure.

The H-bonds formed by the As – V species in water can be of three types- (a) donated by $O_{As,H}$ ($O_{As,H}-H\cdots O$), (b) accepted by $O_{As,H}$ ($O_{As,H}\cdots H-O$) and (c) accepted by O_{As} ($O_{As}\cdots H-O$), except for AsO_4^{3-}, where only the third type of H-bonds are formed. The number of the different types of H-bonds, calculated based on the H-bonding criteria

discussed in chapter 2, is presented in Fig. 5.5. Every $O_{As,H}$ atoms, in all cases, donates almost one H-bond to waters. However, the number of H-bonds accepted by these sites increases across the series, from H_3AsO_4 to $HAsO_4{}^{2-}$. This can be attributed to the increasing charge and availability of more configuration space for hydrogens of waters as compared to H_3AsO_4. The H-bonds accepted by the O_{As} sites also increases with the charge of the species, from H_3AsO_4 to $AsO_4{}^{3-}$. The $AsO_4{}^{3-}$ is found to accept the maximum number of H-bonds of about 2.8 per site. Overall, the total numbers of H-bonds formed (accepted and donated) by H_3AsO_4, $H_2AsO_4{}^-$, $HAsO_4{}^{2-}$ and $AsO_4{}^{3-}$ add up to be 6.8, 8.7, 10.3 and 11.2 respectively. These estimates are in good agreement with the RDF and spatial density distribution (SDD) discussed earlier. Shown with blue bars in Fig. 5.5, the H_2O-H_2O H-bonds in solutions, for all the cases, are found to be lesser in numbers compared to pure waters. This predicts a strong affinity of As−V species in aqueous environment, likely to extend beyond the first hydration shells. This increase in solute-solvent H-bonds are by and large at the expense of the H-bonds between water molecules.

In Fig. 5.6, we have presented various types of solute-solvent H-bond correlation plots, along with the one for pure waters (in logarithmic scale for the sake of clarity in visualization). These functions decay faster than a simple exponential for the first few hundred femto-seconds, presumably because of librational motions of water molecules. The long-time behavior is nearly exponential, thus the characteristic time constant (τ_s) provides a simple qualitative measure of the lifetimes of H-bonds. We shall however note that some authors have followed more rigorous approaches, such as fitting with multiple exponents, integrating the area under the graphs up to infinity, etc. (see the article by Antipova and Petrenko [15] and references therein). We are adopting a rather simple approach, [15] since only qualitative behavior is of significance. The average lifetimes, τ_s, of the H-bond between different solute-water sites, fitting to the long time ($t > 0.5$ ps) behavior of $S_{HB}(t)$ are presented in table 5.2. It shall be noted that these values are liable to large statistical errors due to the fewer number of solute-solvent bonds in the system, despite the fact that we have utilized maximum available time origins from the trajectories. Thus, these values serve largely as “indicators” of the nature of H-bonds.

From Fig. 5.6(a) and table 5.2, it is seen that, as a donor, H_3AsO_4 forms the long-lived H-bonds ($O_{As,H}-H\cdots O$) with water among all As−V species. Consistent with its low pK_{a1}, and the few deprotonation events noted during the MD run, H_3AsO_4 should be forming strongest of H-bonds in the series. The high τ_s of the H-bonds donated

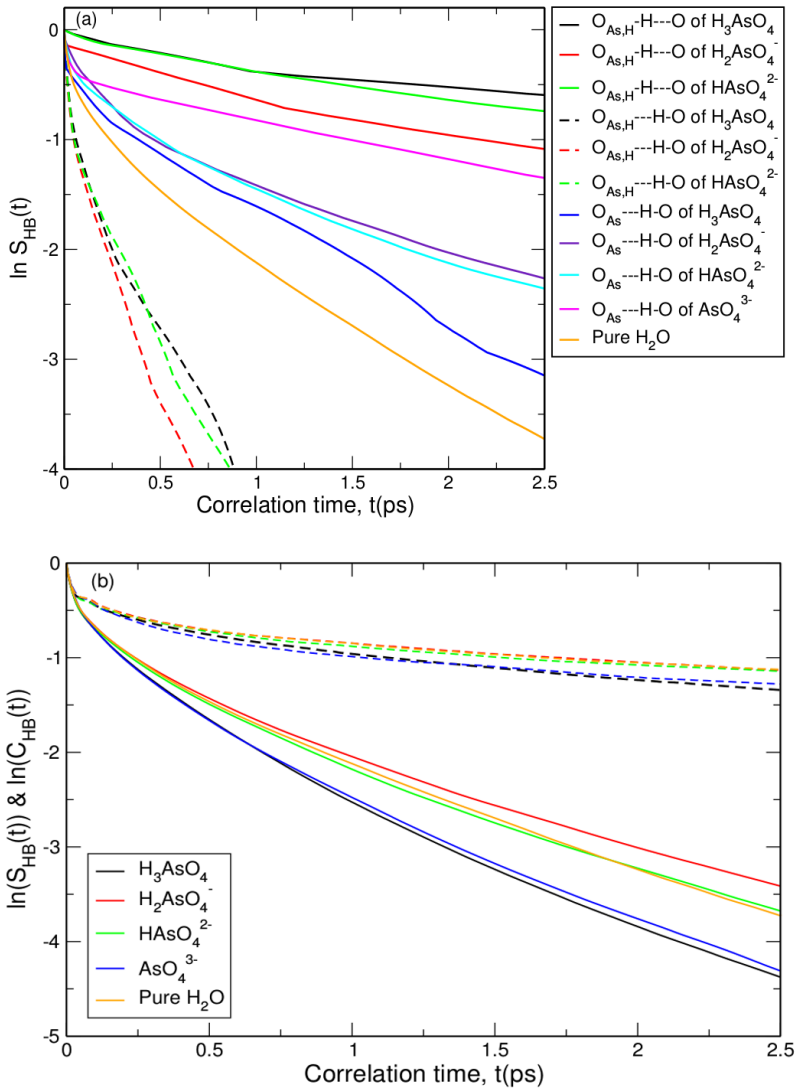

Figure 5.6: (a) Comparison of $S_{\mathrm{HB}}(t)$ for different types of H-bonds formed by different sites of the solute species in aqueous environment, along with that for pure water. (b) Comparison of $S_{\mathrm{HB}}(t)$ and $C_{\mathrm{HB}}(t)$ for bulk water H-bonds of different types of solution environments under study, along with that for pure waters. $S_{\mathrm{HB}}(t)$s are shown in continuous lines, as specified in legends, while $C_{\mathrm{HB}}(t)$s are represented by broken lines of respective colors.

by $O_{As,H}$ can be attributed to these strong H-bonds. In fact, excluding its few short-lived deprotonated states, the water molecule receiving its H-bonds hardly ever got exchanged during the course of time. On the contrary, the H-bonds accepted by O_{As} sites ($O_{As}\cdots H-O$) are most long-lived for AsO_4^{3-}. The life-times of H-bonds accepted by O_{As} show a systematic increase with the charge of the species. Though the same was expected of the $O_{As,H}$ sites, the life-times of accepted and donated by the $O_{As,H}$ in $H_2AsO_4^-$ and

$HAsO_4^{2-}$ does not quite fit into this pattern. This possibly owes to the statistical errors given the few number of solute-solvent H-bonds. It is very useful to note that the H-bonds accepted by the $O_{As,H}$ ($O_{As,H}\cdots H-O$) are slightly short-lived, or weaker, than pure waters, while those accepted by the O_{As} ($O_{As}\cdots H-O$) are long-lived, or stronger, in all cases. The H-bonds donated by the species ($O_{As,H}-H\cdots O$) are significantly stronger than those between water molecules.

In Fig. 5.6(b), the *continuous* and *intermittent* H-bond correlation functions, $S_{HB}(t)$ and $C_{HB}(t)$ for water dissolving the various As−V species as well as that for the pure water are shown. The corresponding characteristic decay constants τ_s and τ_c, fitting to a single exponential are presented in table 5.3. By and large, the characteristic time constants of H-bonds of water dissolving $H_2AsO_4^-$ and $HAsO_4^{2-}$ are closer to those of pure water, while for the solutions of H_3AsO_4 and AsO_4^{3-} the corresponding values are somewhat lower.

Table 5.2: Lifetimes (τ_s) of H-bonds computed from exponential fitting of $S_{HB}(t)$ graphs in Fig. 5.6(a). The total numbers of solvent sites are also listed, along with the statistically averaged number of different H-bonds, based on Fig. 5.5.

Species	H-bond type	τ_s (ps)	Net Number
H_3AsO_4	$O_{As,H}-H\cdots O$	6.23	2.93(3 sites)
	$O_{As,H}\cdots H-O$	0.24	1.72 (3 sites)
	$O_{As}\cdots H-O$	0.96	2.12 (1 site)
$H_2AsO_4^-$	$O_{As,H}-H\cdots O$	3.00	1.98 (2 sites)
	$O_{As,H}\cdots H-O$	0.43	1.60 (2 sites)
	$O_{As}\cdots H-O$	1.58	5.14 (2 sites)
$HAsO_4^{2-}$	$O_{As,H}-H\cdots O$	4.02	0.98 (1 site)
	$O_{As,H}\cdots H-O$	0.34	1.07 (1 site)
	$O_{As}\cdots H-O$	1.60	8.24 (3 sites)
AsO_4^{3-}	$O-H-O$	2.90	11.25 (4 sites)

Table 5.3: The estimated lifetimes and structural relaxation times of the H-bonds, τ_s and τ_c of the solvent water molecules, respectively from $S_{HB}(t)$ and $C_{HB}(t)$ in Fig. 5.6(b). The 4th column provides the orientational relaxation times, τ_2^{OH} of H_2O molecules.

Solute	τ_s(ps)	τ_c (ps)	τ_2^{OH}(ps)
H_3AsO_4	0.76	3.71	5.30
$H_2AsO_4^-$	1.00	6.04	7.53
$HAsO_4^{2-}$	0.92	5.51	5.56
AsO_4^{3-}	0.77	4.86	5.48
Pure H_2O	0.88	5.42	4.86

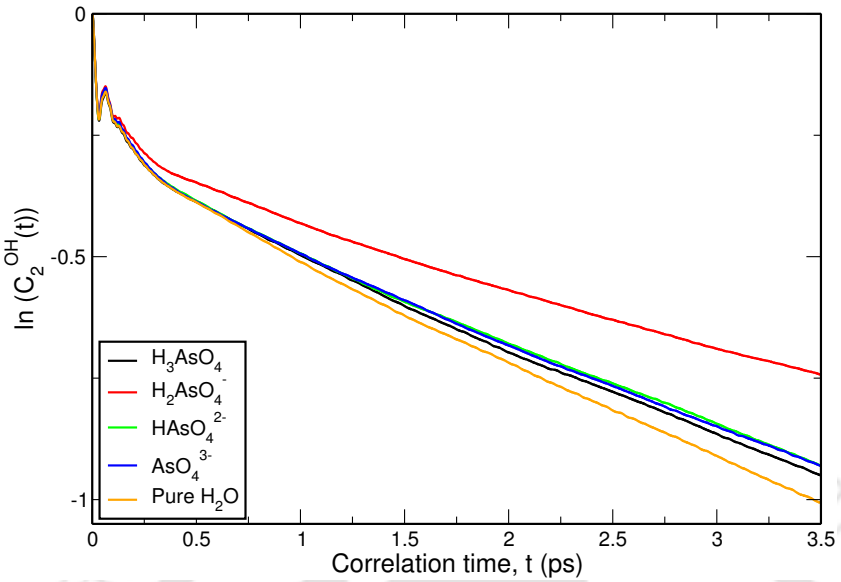

Figure 5.7: Orientational correlation functions, calculated for H_2O molecules along the vector OH

The orientational correlation functions for different solvent-water molecules, $C_2(t)$, discussed in chapter 2, with the vector $\vec{v}$ is chosen to be the $\vec{OH}$ vectors of H_2O molecules is shown in Fig. 5.7. As for the H-bond correlations, $C_{HB}(t)$, the characteristic decay constant are estimated by fitting to single exponentials over the region between 0.5-3.5 ps, for sake of simplicity. The relaxation times of solvent water molecules for the different As-V species are also tabulated in Table 5.3, as the 4^{th} column. The experimental values of H_2O orientational relaxation lies around $1.7-2.6$ ps [16–18] while MD simulations have generally over-estimated the values [17–23]. Previous literature suggests that these values are sensitive to the computational techniques adopted, such as the density functional employed, fitting procedure, statistics, etc [17, 18, 21–23].

Fig. 5.7 and Table 5.3 suggest that waters dissolving As – V species exhibit somewhat slower orientational relaxation compared to pure water, the slowest being noted for the case of $H_2AsO_4^-$. It has been noted earlier that this relaxation is sensitive to the presence of ions in the environment, particularly the dipole moment and polarizabilities of the solutes, in addition to external influences, such as temperature and pressure [21, 24, 25, 25–31]. Bursulaya et. al. [26–28] showed that the increase of dipole moment of the solutes slows down the orientational relaxation of solutes. The dipole moments for the various As – V species in gas phase, calculated in this study, are 2.95, 3.80, 2.90 and 0.04 D, respectively for H_3AsO_4, $H_2AsO_4^-$, $HAsO_4^{2-}$ and AsO_4^{3-}. In agreement with

Bursulaya et. al.[26], in the present case as well the orientational relaxation (not shown) of the solute molecules themselves (taking the vectors along $As-O_{As}$ and $As-O_{As,H}$ bonds) were slowest for $H_2AsO_4^-$ among all the As–V species. This could in turn slow down the dynamics of the solvents molecules. Thus factors such as, the higher dipole moment of $H_2AsO_4^-$ and its slightly overstructured solvent (noted earlier in the O–O rdf in Fig.5.4(c)), could be responsible for the slow orientational relaxation of water dissolving $H_2AsO_4^-$.

Table 5.4: Gas-phase frequencies of H_3AsO_4 along with a qualitative description of the normal modes.

Serial No.	Frequency (cm^{-1})	Description of the mode
1 - 8	97, 173, 204, 303, 317, 332, 336, 342	Various low frequency modes, eg., torsion,twisting, rocking, wagging, etc.
9 - 11	704, 724, 745	$As-O_{As,H}$ bond stretching modes.
12 -14	961, 968, 988	Various $As-O_{As,H}-H$ bending modes.
15	1048	Asymmetric stretching of $As-O_{As}$ bond w.r.t. the three $As-O_{As,H}$ bonds.
16	3682	Asymmetric stretching of $O_{As,H}-H$ bonds involving two of them.
17	3689	Asymmetric stretching of $O_{As,H}-H$ bonds, involving all three of them.
18	3695	Symmetric stretching of $O_{As,H}-H$ bonds, involving all three.

5.3.4 Vibrational Density of States

The vibrational density of states (VDOS) or power spectra, calculated as the Fourier transformation of the velocity auto-correlation function (VACF), are presented in Fig.5.8. The top panel of the figure shows the spectra for the hydrogens of H_3AsO_4 (black), $H_2AsO_4^-$ (red), $HAsO_4^{2-}$ (green) and of pure water (orange). Also shown, above the plots, are the gas phase normal modes frequencies of H_3AsO_4 (black), $H_2AsO_4^-$ (red), $HAsO_4^{2-}$ (green) and AsO_4^{3-} (blue) molecule. The normal mode frequencies are listed in table 5.4 along with a qualitative description of the modes. In the bottom panel, power spectra of O_{As} (as solid lines) and $O_{As,H}$ (as dotted lines) for the different As–V species, namely, H_3AsO_4 (black), $H_2AsO_4^-$ (red), $HAsO_4^{2-}$ (green) and AsO_4^{3-} (blue), are shown. The normal frequencies of gas phase H_3AsO_4, up to the range of 1400 cm^{-1} are reproduced also in the lower panel for ease of comparison. In aqueous environments,

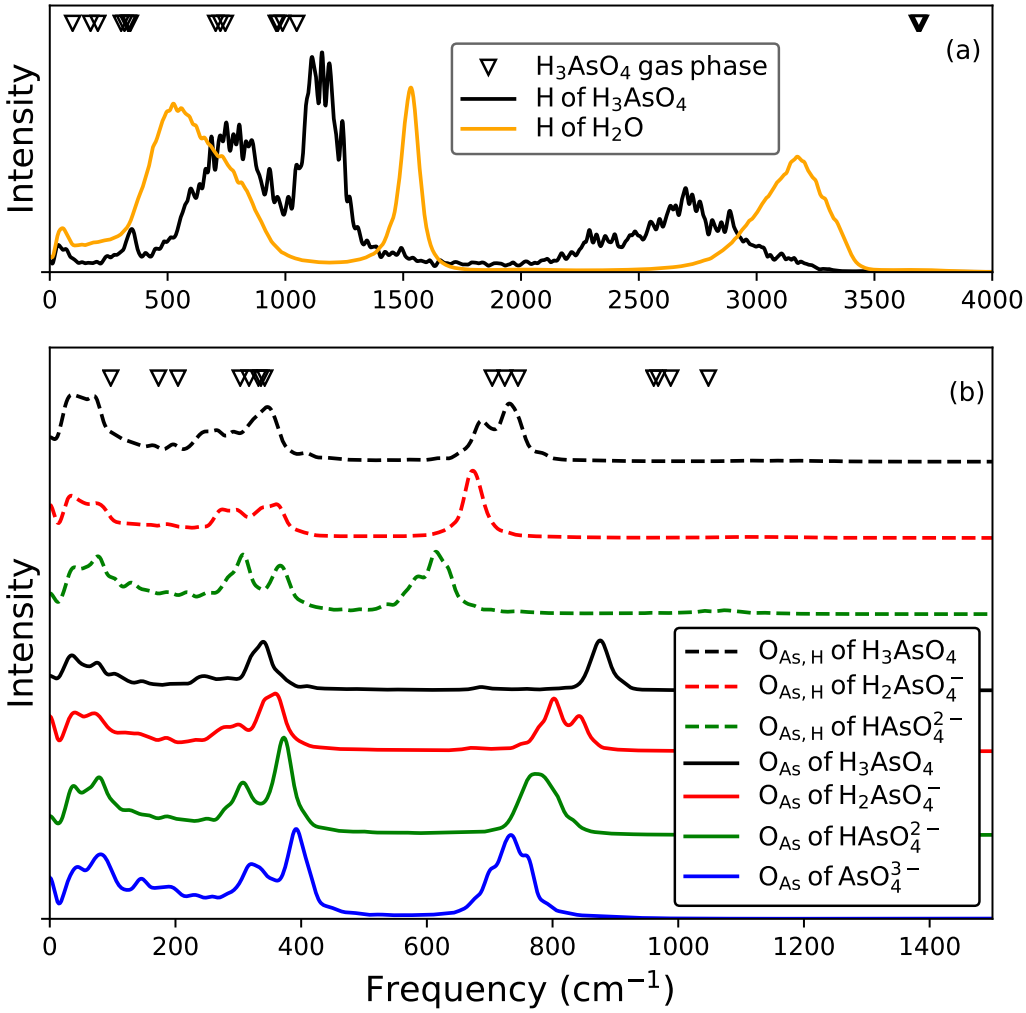

Figure 5.8: Vibrational density of states (VDOS) calculated from velocity autocorrelation function (VACF) for $O_{As,H}$ (dotted lines) and O_{As} (solid lines) of H_3AsO_4 (black), $H_2AsO_4^-$ (red), $HAsO_4^{2-}$ (green) and AsO_4^{3-} (blue) are shown. The triangles, with respective colors, represents the gas phase optimized harmonic modes of vibrations for the species. See table 5.4 for descriptions of these modes.

the $O_{As,H}-H$ and $O-H$ vibration modes (top panel of Fig.5.8) gets highly red-shifted owing to H-bonding. The $As-O_{As,H}-H$ bending modes observed in the range of 950 -1000 cm^{-1} (see Table 5.4) in the gas-phase appears to have blue-shifted to 1000-1300 cm^{-1} with significant dispersion (see H-spectra (red) on top-panel of Fig.5.8) in aqueous environment. It shall also be noted that the $As-O_{As,H}-H$ bending modes are significantly lower than the $H-O-H$ bending modes (shown in black on top-panel of Fig.5.8) that measures around 1550 cm^{-1}. The $As-O_{As}$ and $As-O_{As}$ stretching modes observed

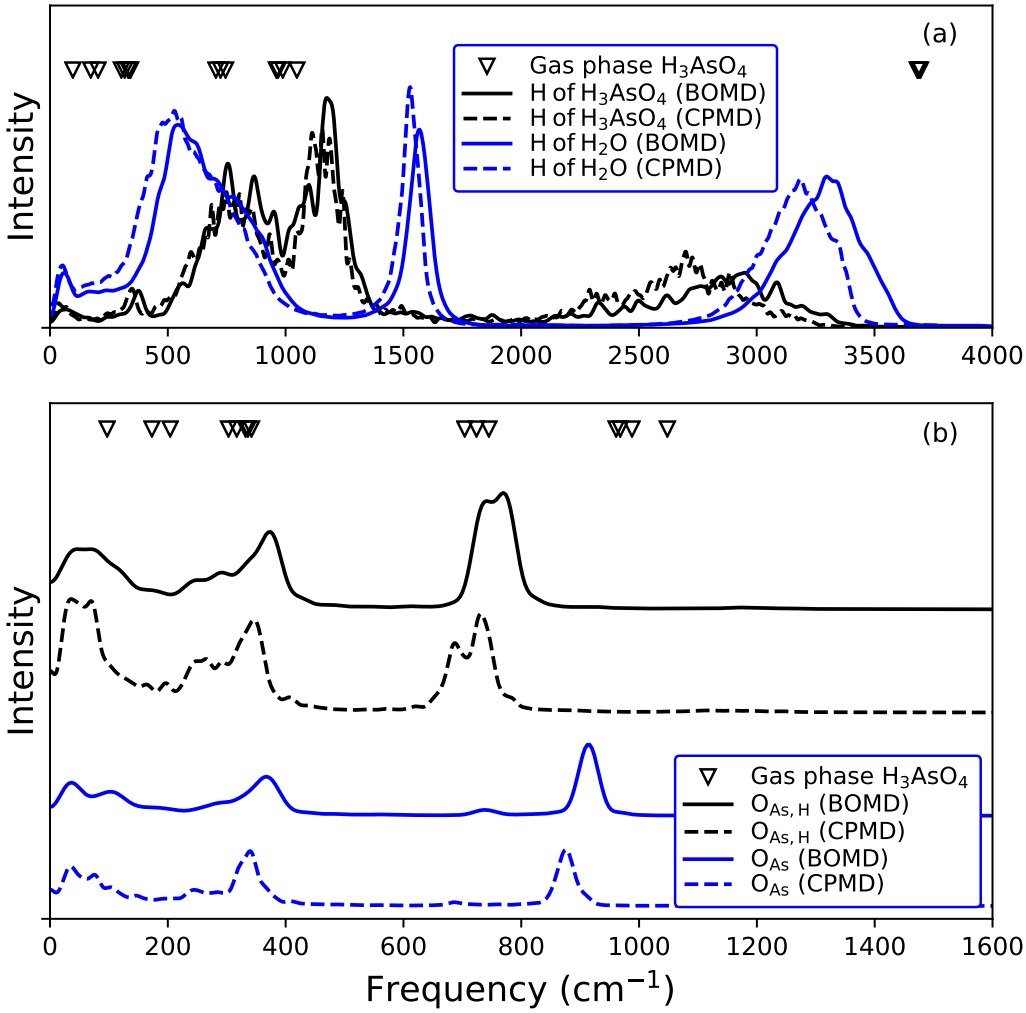

Figure 5.9: The vibrational density of states (VDOS) from CPMD (dotted lines) simulation is compared with Born-Oppenheimer (BO) MD (solid lines). Top panel (a): H of H_3AsO_4 (black) and H of H_2O (blue); Bottom panel (b): $O_{As,H}$ (black) and O_{As} (blue) atoms of H_3AsO_4. The gas phase vibrational frequencies are shown in both panels as triangles pointed-down. These calculations are performed at the same level of theory as the CPMD simulations, except that a larger time steps of 0.25 fs is used, and the total run is 6 ps long.

respectively at 1048 cm^{-1} and over 700-750 cm^{-1} for the gas-phase H_3AsO_4, shows systematic softening across the series, from H_3AsO_4 to $AsO_4{}^{3-}$, with the net effective charges of the species. This is consistent with the increase in the bond-lengths of $As-O_{As}$ and $As-O_{As}$ given in Table 5.4. Overall nature of the spectra is in agreement with previous experimental and simulation results in literature [16, 32–34].

We shall, however, note that the Car-Parrinello scheme employs heavy electronic

mass to propagate the electronic wave-functions efficiently, causing a “drag effect" on the nuclear degrees of freedom, thus resulting in an artificial red-shift in the vibration frequencies of the atomic species. In order to estimate this artifact we have carried out a short Born-Oppenheimer Molecular Dynamics (BOMD) simulation of H_3AsO_4 in water, at an identical theoretical level. In Fig. 5.9 the VDOS calculated from CPMD and BOMD simulations are shown for comparison. The shifts of CPMD spectra w.r.t. the BOMD ones are approx. 110 cm^{-1} for OH stretching modes of H_2O and approx. 240 cm^{-1} for those of H_3AsO_4 (intra-molecular), while for $As-O_{As}$ and $As-O_{As,H}$, those are approx. 40 cm^{-1}. Thus, it shall be noted that CPMD simulations over estimates the red-shift by about 25%. Thus a quantitative assessment of *frequency shifts* may account for this.

5.4 Conclusion

We have carried out extensive *ab initio* MD simulations on As – V species in aqueous environment to investigate the nature of hydration and H-bonding in details. H_3AsO_4, which is, in general, stable in acidic aqueous environments, found to accumulate the least ordered hydration shell, forming the least number of intermolecular H-bonds, as compared to $H_2AsO_4^-$, $HAsO_4^{2-}$ and AsO_4^{3-}. For the last three species, the effects of hydration are liable to extend beyond the first hydration shells.

It is seen that the total number of H-bonds increases in sequence from H_3AsO_4 to AsO_4^{3-}, thus aided by the increasing charge on the solute species. This leads to lengthening of the $As-O_{As}$ and $As-O_{As,H}$ bonds and strengthening of the H-bonds, resulting in sequential red-shifts in the vibrational density of states, in the same order as above. In all the cases, the donated H-bonds are found to be considerably longer lived compared to the accepted ones. AsO_4^{3-}, which is liable to be stable in basic aqueous medium, exhibits the most structured, well-defined and stable solvation shells of all, also forming the maximum number of H-bonds that exhibit considerably stronger and longer-lived H-bonds. $HAsO_4^{2-}$, although forms more number of H-bonds than compared to $H_2AsO_4^-$, exhibits comparable lifetimes of the H-bonds. This predicts that both these species might be stable under normal pH conditions, supported as well by the reported pK_a values. It is also inferred that water in presence of the $H_2AsO_4^-$ become relatively over-structured, and results in higher H-bond lifetimes, and slower structural and orientational relaxations of water molecules.

BIBLIOGRAPHY

[1] Johan Mähler, Ingmar Persson, and Roger B Herbert. Hydration of arsenic oxyacid species. *Dalton Trans.*, 42(5):1364–1377, 2013.

[2] Anirban Bhattacharjee, Thomas S Hofer, Andreas B Pribil, Bernhard R Randolf, and Bernd M Rode. Hydrolysis of as(iii): A femtosecond process. *Chem. Phys. Lett.*, 473(1):176–178, 2009.

[3] Axel D Becke. Density-functional exchange-energy approximation with correct asymptotic behavior. *Phys. Rev. A*, 38(6):3098, 1988.

[4] Chengteh Lee, Weitao Yang, and Robert G Parr. Development of the colle-salvetti correlation-energy formula into a functional of the electron density. *Phys. Rev. B*, 37(2):785, 1988.

[5] Dominik Marx and Jürg Hutter. *Ab initio molecular dynamics: basic theory and advanced methods*. Cambridge University Press, 2009.

[6] Shūichi Nosé. A molecular dynamics method for simulations in the canonical ensemble. *Mol. Phys.*, 52(2):255–268, 1984.

[7] Shuichi Nosé. A unified formulation of the constant temperature molecular dynamics methods. *J. Chem. Phys.*, 81(1):511–519, 1984.

[8] William G Hoover. Canonical dynamics: equilibrium phase-space distributions. *Phys. Rev. A*, 31(3):1695, 1985.

[9] I-Feng W Kuo and Christopher J Mundy. An ab initio molecular dynamics study of the aqueous liquid-vapor interface. *Science*, 303(5658):658–660, 2004.

[10] P Padma Kumar, Andrey G Kalinichev, and R James Kirkpatrick. Dissociation of carbonic acid: Gas phase energetics and mechanism from ab initio metadynamics simulations. *J. Chem. Phys.*, 126(20):204315, 2007.

[11] Glenn J Martyna and Mark E Tuckerman. A reciprocal space based method for treating long range interactions in ab initio and force-field-based calculations in clusters. *J. Chem. Phys.*, 110(6):2810–2821, 1999.

[12] M E Tuckerman. Ab initio molecular dynamics: basic concepts, current trends and novel applications. *J. Phys. Condens. Matter.*, 14(50):R1297–R1355, 2002.

[13] CPMD. General program to perform ab initio molecular dynamics simulations. *CPMD developers group under the terms of the GNU General Public License, http://www.cpmd.org*.

[14] Martin Brehm and Barbara Kirchner. Travis-a free analyzer and visualizer for monte carlo and molecular dynamics trajectories. *J. Chem. Inf. Model.*, 51(3):2007–2023, 2011.

[15] ML Antipova and VE Petrenko. Hydrogen bond lifetime for water in classic and quantum molecular dynamics. *Russ. J. Phys. Chem. A*, 87(7):1170–1174, 2013.

[16] FK Vansant, BJ Van Der Veken, and HO Desseyn. Vibrational analysis of arsenic acid and its anions: I. description of the raman spectra. *J. Mol. Structure*, 15(3):425–437, 1973.

[17] Michiel Sprik, Jürg Hutter, and Michele Parrinello. Ab initio molecular dynamics simulation of liquid water: Comparison of three gradient-corrected density functionals. *J. Chem. Phys.*, 105(3):1142–1152, 1996.

[18] David E Smith and Liem X Dang. Computer simulations of nacl association in polarizable water. *J. Chem. Phys.*, 100(5):3757–3766, 1994.

[19] Bhabani S Mallik, A Semparithi, and Amalendu Chandra. Vibrational spectral diffusion and hydrogen bond dynamics in heavy water from first principles. *J.Phys. Chem. A*, 112(23):5104–5112, 2008.

[20] Ashu Choudhary and Amalendu Chandra. Anisotropic structure and dynamics of the solvation shell of a benzene solute in liquid water from ab initio molecular dynamics simulations. *Phys. Chem. Chem. Phys.*, 18(8):6132–6145, 2016.

[21] Amalendu Chandra. Effects of ion atmosphere on hydrogen-bond dynamics in aqueous electrolyte solutions. *Phys Rev Lett*, 85(4):768, 2000.

[22] Damien Laage and James T Hynes. A molecular jump mechanism of water reorientation. *Science*, 311(5762):832–835, 2006.

[23] Jean Boisson, Guillaume Stirnemann, Damien Laage, and James T Hynes. Water reorientation dynamics in the first hydration shells of f- and i-. *Phys. Chem. Chem. Phys.*, 13(44):19895–19901, 2011.

[24] Henry S Frank and Wen-Yang Wen. Ion-solvent interaction. structural aspects of ion-solvent interaction in aqueous solutions: a suggested picture of water structure. *Discuss. Faraday Soc.*, 24:133–140, 1957.

[25] Yizhak Marcus. Effect of ions on the structure of water: structure making and breaking. *Chem. Rev.*, 109(3):1346–1370, 2009.

[26] Badry D Bursulaya, Dominic A Zichi, and Hyung J Kim. Molecular dynamics simulation study of polarizable solute solvation in water. 1. equilibrium solvent structure and solute rotational dynamics. *J. Phys. Chem.*, 100(4):1392–1405, 1996.

[27] Badry D Bursulaya, Dominic A Zichi, and Hyung J Kim. Role of solute electronic polarizability in solvation dynamics. *J. Phys. Chem.*, 99(25):10069–10074, 1995.

[28] Badry D Bursulaya, Jonggu Jeon, Dominic A Zichi, and Hyung J Kim. Generalized molecular mechanics including quantum electronic structure variation of polar solvents. ii. a molecular dynamics simulation study of water. *J. Chem. Phys.*, 108(8):3286–3295, 1998.

[29] Albert J Cross and John D Simon. Rotational dynamics of a solvated dipole: A molecular dynamics study of dielectric friction. *J. Chem. Phys.*, 86(12):7079–7083, 1987.

[30] A Geiger. Molecular dynamics simulation study of the negative hydration effect in aqueous electrolyte solutions. *Ber. Bunsenges. Phys. Chem.*, 85(1):52–63, 1981.

[31] Zhonghua Ma and Mark E Tuckerman. On the connection between proton transport, structural diffusion, and reorientation of the hydrated hydroxide ion as a function of temperature. *Chem. Phys. Lett.*, 511(4):177–182, 2011.

[32] Sabyasachi Bagchi, Indranil Bhattacharyya, Bhaskar Mondal, and Abhijit K Das. Structure, stability

and energetics of ionic arsenic–water complexes. *Mol. Phys.*, 109(6):933–941, 2011.

[33] Anirban Bhattacharjee, Thomas S Hofer, Andreas B Pribil, Bernhard R Randolf, and Bernd M Rode. Hydrolytic conversion of aso43- to haso42-: a qmcf md study. *Phys. Chem. Chem. Phys.*, 12(23):6244–6246, 2010.

[34] Satish CB Myneni, Samuel J Traina, Glenn A Waychunas, and Terry J Logan. Experimental and theoretical vibrational spectroscopic evaluation of arsenate coordination in aqueous solutions, solids, and at mineral-water interfaces. *Geochim. Cosmochim. Acta*, 62(19):3285–3300, 1998.

CHAPTER 6

AIMD Study of Waterborne As–III Species

6.1 Introduction

In addition to As–V species, the other form of arsenic that is highly soluble in aqueous conditions is As–III species. The parent form of the As–III is known as arsenous acid (H_3AsO_3), which is a very weak acid with experimentally reported pK_{a1} value of 9.25 [1]. Its deprotonated forms namely $H_2AsO_3^-$ and $HAsO_3^{2-}$ are reported to have pK_{a2} = 12.13 and pK_{a2} = 13.40 [1].

$$H_3AsO_3 \xrightarrow[9.25]{pK_{a1}} H_2AsO_3^- \xrightarrow[12.13]{pK_{a2}} HAsO_3^{2-} \xrightarrow[13.40]{pK_{a3}} AsO_3^{3-} \tag{6.1}$$

Thus, H_3AsO_3 is stable in aqueous environments at normal pH conditions. The hydration and spectroscopic aspects of hydrated H_3AsO_3 species have been recently probed experimentally employing large angle X-ray scattering (LAXS), EXAFS and double difference infrared (DDIR) spectroscopy by Mähler et al [1].

Reportedly, As–III species are more toxic, soluble and mobile compared to those of As–V [2, 3]. As–III species have been found to show higher affinity towards certain groups and minerals [4, 5]. As far as water remediation is concerned, As–V species have been found to be easily removed as compared to As–III ones [6].

Publication based on this chapter: Sangkha Borah and P. Padma Kumar (manuscript under preparation)

In this chapter, we are presenting AIMD studies on waterborne As – III species. Detailed microscopic insights on hydration and nature of hydrogen-bonding (H-bonding), structural and vibrational properties have been summarized.

6.2 Methods

CPMD simulations have been carried out on various As – III species viz., (i) H_3AsO_3, (ii) $H_2AsO_3^-$, and (iii) $HAsO_3^{2-}$, all being solvated in 60 H_2O molecules, in a cubic box of length 12.42 Å, that correspond to an overall density about 1.05 g/cc. The initial systems are prepared from the final structures of H_2SeO_3 discussed in chapter 3, further optimized and equilibrated for 30 – 50 ps, after which production runs of over 60 ps have been carried out.

All simulations have been performed with gradient-corrected, norm-conserving BLYP [7, 8] pseudo-potentials with Kohn-Sham orbitals [9, 10] expanded up to 85 Ry., and Nose-Hoover thermostats [11–13] controlling the temperature of the ions at 315 K. A fictitious mass of 600 au is employed for maintaining a good conversation of energy and adiabaticity [14, 15]. The time step of integration is 0.1 fs and the trajectories are printed at every 5 MD steps for production runs which are subjected to detailed analysis discussed below. Further, normal-mode analysis of H_3AsO_3 molecule is carried out in gas-phase [16–18].

As in the previous chapter, we shall use the label O_{As} for oxygens of As species not bonded to hydrogen and $O_{As,H}$ for those bonded to hydrogen.

6.3 Results and Discussions

6.3.1 Proton Transfer

The As – III species show very weak acidic character unlike the case As – V species, discussed in chapter 5. Within the time-scales of simulations, we have found both H_3AsO_3 and $H_2AsO_3^-$ existing as stable species. However, $HAsO_3^{2-}$, within a few pico-second of runs (during the equilibration phase itself), found to capture one of the hydrogens in its solvation shell becoming $H_2AsO_3^-$ that remained stable for the rest of the simulation runs. Similarly, AsO_3^{3-}, within a few femto-seconds of simulations, captures one H from a nearby H_2O molecule becoming $HAsO_3^{2-}$, which remained stable. AsO_3^{3-} even

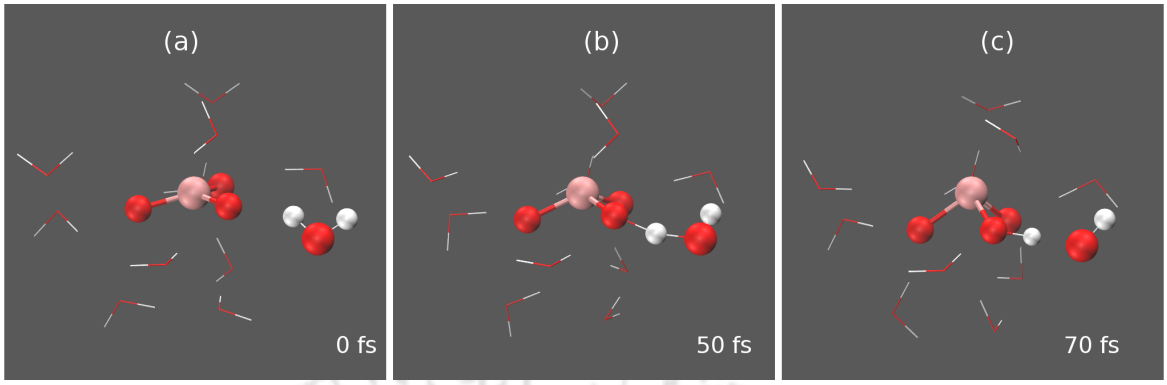

Figure 6.1: Proton transfer leading to the conformational change of planar-AsO_3^{3-} to the *tripodal*- structure of $HAsO_3^{2-}$.

not found to be stable in a basic medium containing one OH^- ion in $60\,H_2O + 1\,OH^-$ environment, at least over 30 ps of production runs. This is due to the high basic nature of AsO_3^{3-}. It is also noted that AsO_3^{3-}, which has a planar structure, changes its structure to *tripodal* structure of $HAsO_3^{2-}$ by capturing one of H of its solvation shell. These structural changes are noted to occur within a timescale of ~ 100 femto-seconds of simulations, as can be seen from Fig. 6.1.

6.3.2 Molecular Structure

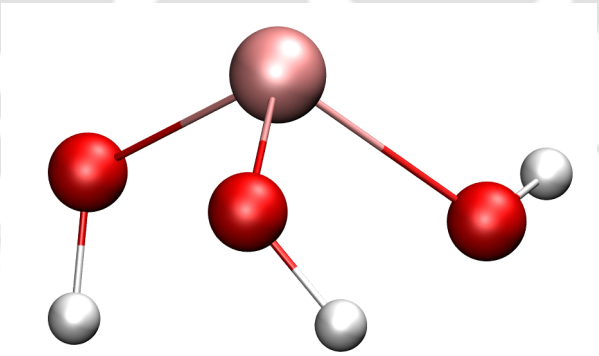

Figure 6.2: Gas phase geometry optimized structure of H_3AsO_3.

Arsenous acid, H_3AsO_3 has a pyramidal structure (if the orientation of the H atoms are ignored), with the three hydroxyl groups (OH^-) bonded to the As atom at the apex through single bonds. In Fig. 6.2, the gas-phase optimized structure of H_3AsO_3 is shown. Table 6.1 contains a detailed description of the various $As-O_{As}$ and $As-O_{As,H}$ bond-

Table 6.1: Comparison of $As-O_{As}$ and $As-O_{As,H}$ bond lengths for the As – III species, obtained from aqueous and gas phase calculations. 6-31G* SCF level of DFT-optimized results taken from [19] are included in the last column of the table. The solution phase results for AsO_3^{3-} is not included for poor statistics.

Species	Type	Solution (Å)	Gas (Å)	Ref. [19] (Å)
H_3AsO_3	$As-O_{As-H}$	1.76	1.76	1.75
$H_2AsO_3^-$	$As-O_{As-H}$	1.81	1.85	1.81
	$As-O_{As}$	1.67	1.64	1.65
$HAsO_3^{2-}$	$As-O_{As-H}$	1.88	1.88	1.82
	$As-O_{As}$	1.71	1.71	1.67
AsO_3^{3-}	$As-O_{As}$	···	1.61	1.75

lengths, both in gas phase as well as in the solution phase, for each of the cases, viz., H_3AsO_3, $H_2AsO_3^-$, $HAsO_3^{2-}$ and AsO_3^{3-}, except for the last species, where the solution phase values are not included. The same sets of functional (BLYP) have been employed for both gas and solution phase calculations. The results are found to be comparable with the previous results, included in the 4^{th} column of the table [19].

The deprotonated forms of H_3AsO_3 are found to be sensitive to the effective charge on the species. The $As-O_{As}$ and $As-O_{As,H}$ bond-lengths are found to increase from H_3AsO_3 to AsO_3^{3-} in series. On the other hand, from H_3AsO_3 to AsO_3^{3-}, the three $O_{As}-As-O_{As}$ angles increase gradually starting from an average value of $\sim 98°$, thereby decreasing the height of the pyramid, which becomes completely planar ($\theta = 120°$) for AsO_3^{3-} in gas phases.

6.3.3 Hydration Structure

Fig. 6.3(a), (b) and (c) show typical snapshots of the simulated systems, with H_3AsO_3, $H_2AsO_3^-$ and $HAsO_3^{2-}$ been solvated by 60 H_2O molecules, obtained from CPMD simulations at 315 K temperature. The solvation shells around these species, calculated employing the H-bonding criterion as mentioned in chapter 2, are shown respectively in Fig. 6.3(d), (e) and (f). The instantaneous H-bonds are shown with brown colored dotted lines. The local hydration structures of the solutes are best visualized by spatial density distributions (SDD), shown in Fig. 6.4(a)-(c). These are produced by transforming the coordinates of H-bonded water molecules to a selected choice of body fixed axes of the solute species. These transformed coordinates are then mapped on to a fine 3-dimensional grid and averaged over the length of the simulation. The red and white

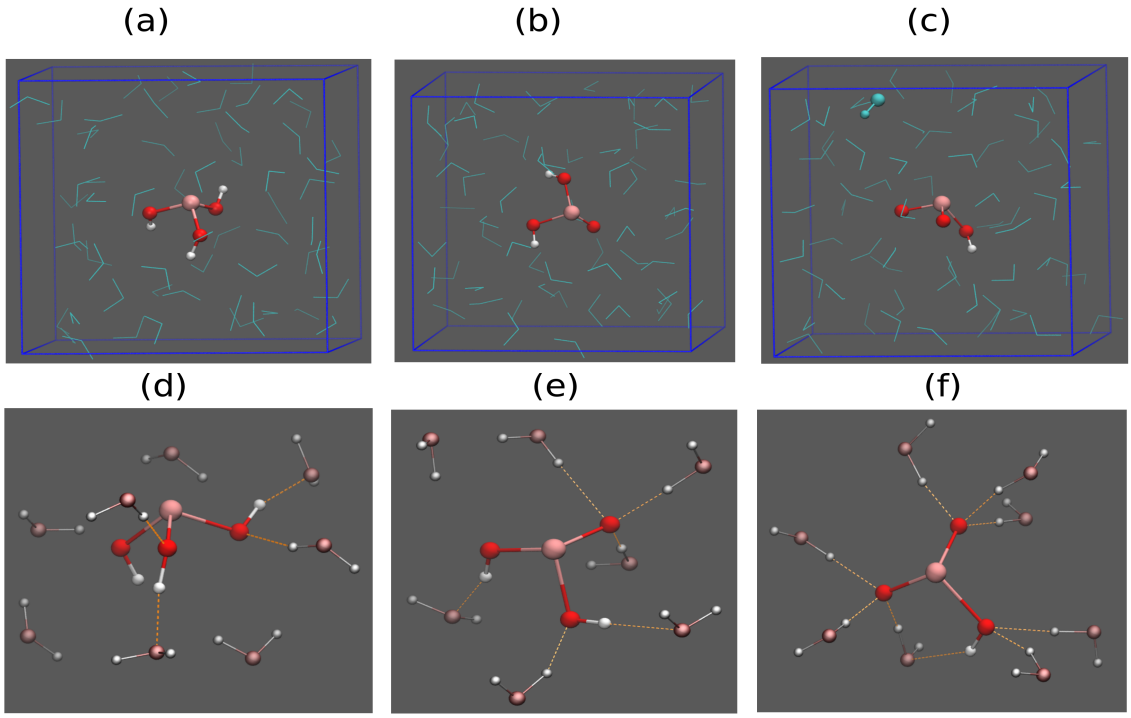

Figure 6.3: Snapshots of (a) H_3AsO_3, (b) $H_2AsO_3^-$ and (c) $HAsO_3^{2-}$, solvated in H_2O molecules from CPMD simulations at 315 are shown. The water molecules are shown as sticks of color cyan. In Fig. (c) the solvated hydroxide (OH^-) ion is shown in ball and stick representation in color cyan. Fig. (d), (e) and (f) show H_2O molecules lying within the H-bonding criterion (i) (see chapter 2), along with the instantaneous H-bonding structures for (a) H_3AsO_3, (b) $H_2AsO_3^-$ and (c) $HAsO_3^{2-}$.

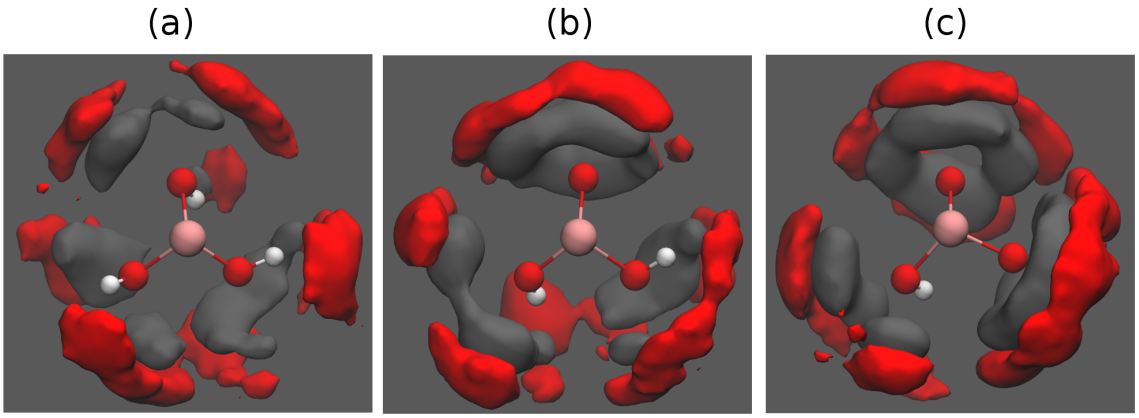

Figure 6.4: The spatial density distributions (SDD) of hydrogens (gray) and oxygens (red) of H-bonded H_2O molecules, around (a) H_3AsO_3, (b) $H_2AsO_3^-$ and (c) $HAsO_3^{2-}$ species are shown. A uniform threshold number density (isovalue) of 0.04 $Å^{-3}$ is chosen for the isosurface in all the spatial density distribution plots.

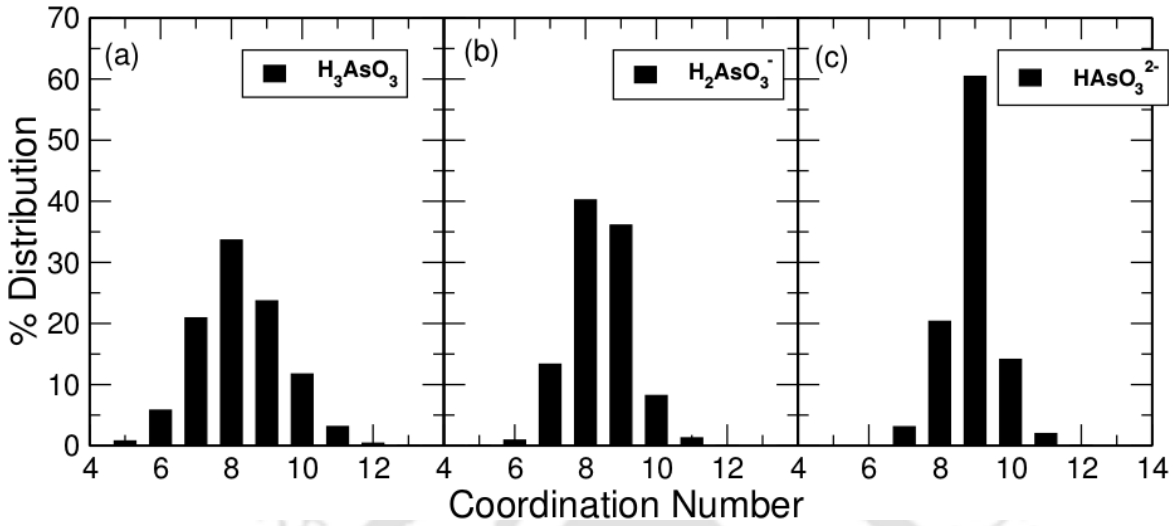

Figure 6.5: The coordination number distribution (in percentage) of H_2O molecules around the (a) H_3AsO_3, (b) $H_2AsO_3^-$ and (c) $HAsO_3^{2-}$ lying within H-bonding criterion (i) (given in chapter 2) are shown.

surfaces in these plots represent the O and H of H_2O molecules respectively, lying within the H-bonding criteria discussed in chapter 2, all shown for a uniform iso-value of 0.04 $Å^{-3}$. It is observed that there is an increase in ordering in the first the hydration shell from H_3AsO_3 to $HAsO_3^{2-}$.

Fig. 6.5(a) and 6.5(b) show the coordination number distribution (in percentage) of the solvents within 3.5 Å of oxygens of the solutes (H_3AsO_3, $H_2AsO_3^-$ and SeO_4^{2-}) respectively. These plots, in addition, gives the measure of the fluctuations in first hydration shell of the solutes. It can be observed from these plots that $HAsO_3^{2-}$ has a much more compact water distribution around it than those of $H_2AsO_3^-$ and H_3AsO_3, consistent with the SDD plots shown in Fig. 6.4.

6.3.4 Hydrogen-bonding

The geometric distributions of H_2O molecules around the solute species can be described from O_{As} – O and O_{As} – H RDFs, shown in Fig. 6.6(a) and (b). It shall be noted that in this context no distinction between O_{As} and $O_{As,H}$ is made. Similarly, in Fig 6.6(b) the intra-molecular H of As – III species have not been distinguished from H of bulk water molecules, and hence the first peaks around 1 Å signifies the intermolecular hydrogen atoms. In these plots, the corresponding RDFs for pure waters have also been included for the sake of comparison. It is apparent from these plots that there is a gradual increase

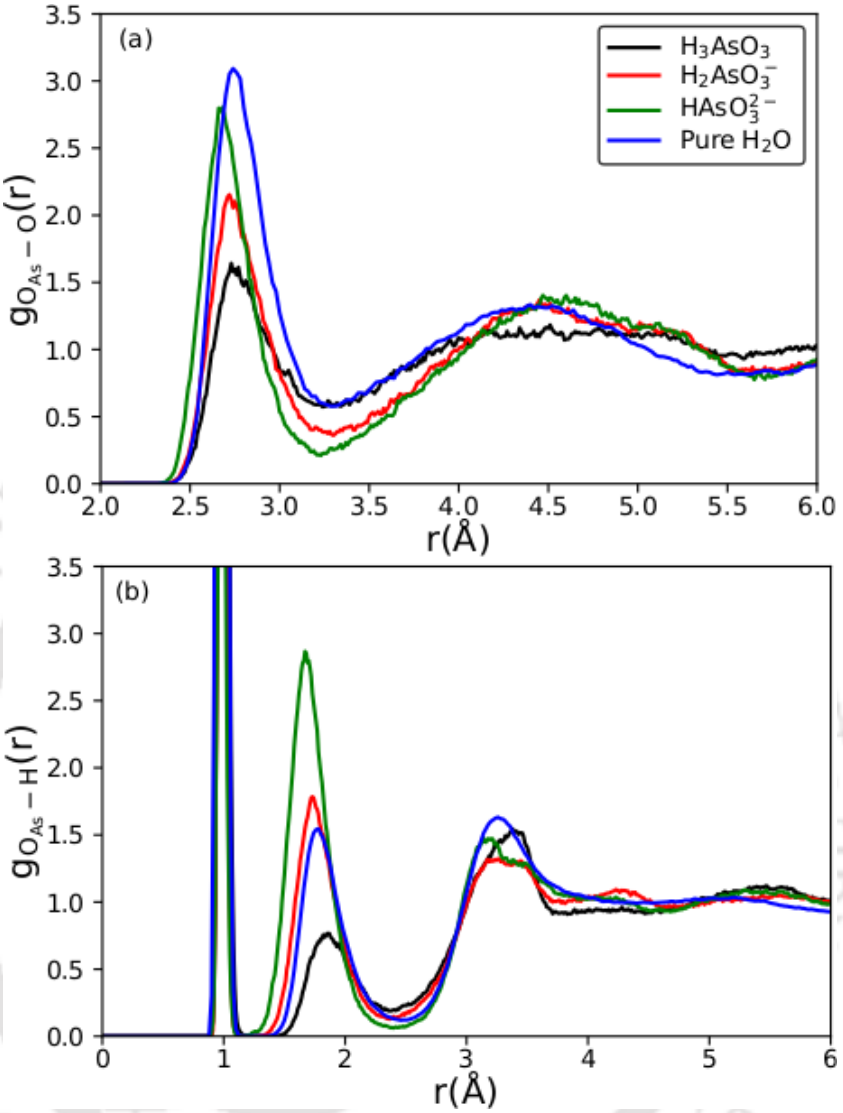

Figure 6.6: Atomic radial distribution functions (RDF), $g(r)$, of (a) $O_{As}-O$ and (b) $O_{As}-H$ pairs for H_3AsO_3(black), $H_2AsO_3{}^-$(red) and $HAsO_3{}^{2-}$. In these plots O_{As} includes both O_{As} as well as $O_{As,H}$ types of atoms. In Fig. (b), the 1^{st} peaks around 1 Å are due to the intra-molecular $H_{As,H}$ atoms. Pure H_2O RDFs are included for comparison (in blue lines)

in water structure around the solutes starting from H_3AsO_3 to $HAsO_3{}^{2-}$ in series. This observation is in conformity with the SDD and CN-plots shown in Fig. 6.4 and 6.5 respectively. Fig. 6.6(b) reveals the strong affinity of $HAsO_3{}^{2-}$ towards the H of solvent molecules, which is why we have obtained a well-structured and compact solvation shell around $HAsO_3{}^{2-}$, shown in Fig. 6.4.

The H-bonds formed by the As-species in water can be of three types - (a) donated by $O_{As,H}$ (represented as $O_{As,H}-H\cdots O$), (b) accepted by $O_{As,H}$ ($O_{As,H}\cdots H-O$) and (c)

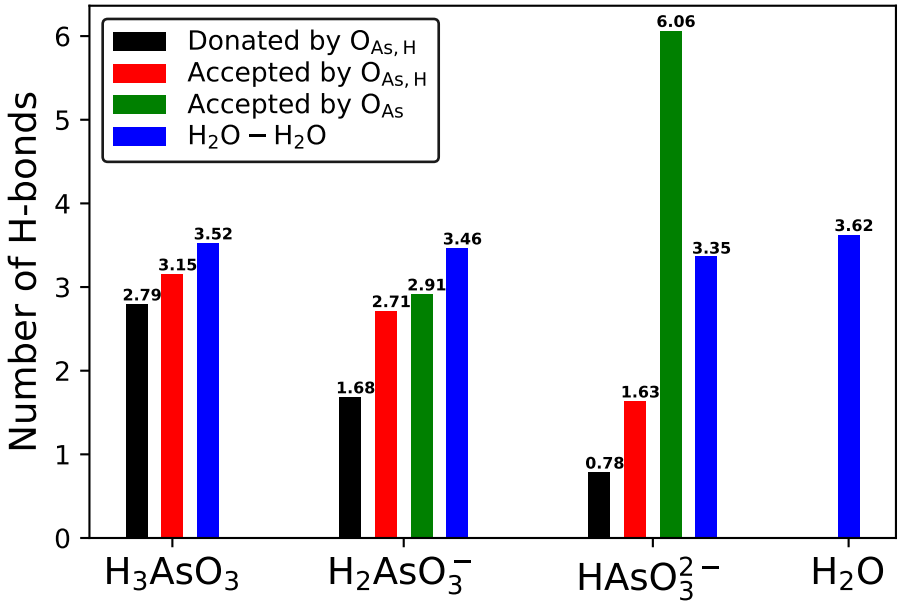

Figure 6.7: Number of H-bonds of different types (i. donated by $O_{As,H}$ (black bars), ii. accepted by $O_{As,H}$ (red), iii. accepted by O_{As} (green) and iv. bulk and pure H_2Os (blue bars)), calculated based on H-bonding criteria for H_3AsO_3, $H_2AsO_3^-$, $HAsO_3^{2-}$ and pure H_2O systems.

accepted by O_{As} ($O_{As}\cdots H-O$). The number of H-bonds, calculated based on the H-bonding criteria discussed chapter 2, is presented in Fig. 6.7. The number of H-bonds accepted by the O_{As} sites of these species increases with the increasing charges of the solutes, across the series from H_3AsO_3 to $HAsO_3^{2-}$, while the number donated by $O_{As,H}$ per site follows the opposite trend. Overall, the numbers of H-bonds formed with waters, both as donor and acceptor, add up to 6.0, 7.3 and 8.5 respectively. These are in quantitative agreement with the coordination number (Fig. 6.5) and spatial distribution (Fig. 6.4) around the solutes and stability of the shells. Shown with blue bars in Fig.6.7 are the water-watter H-bonds, which suggests that at the expense of water-water H-bonds, the number of solute-water H-bond have increased.

In Fig. 6.8, we have presented various types of solute-solvent H-bond correlation plots (in logarithmic scales for the sake of clarity in visualization). The donated H-bonds are shown in solid lines, while the accepted ones are with dotted lines of the respective colors (black: H_3AsO_3, red: $H_2AsO_3^-$ and blue: $HAsO_3^{2-}$). These plots are sensitive to intermittent breaking of H-bonds and are known as *continuous* H-bond correlation functions. These plots decays rapidly at the beginning for a few hundreds of femto-seconds owing to the making of short lasting *peripheral* H-bonds, beyond which these can

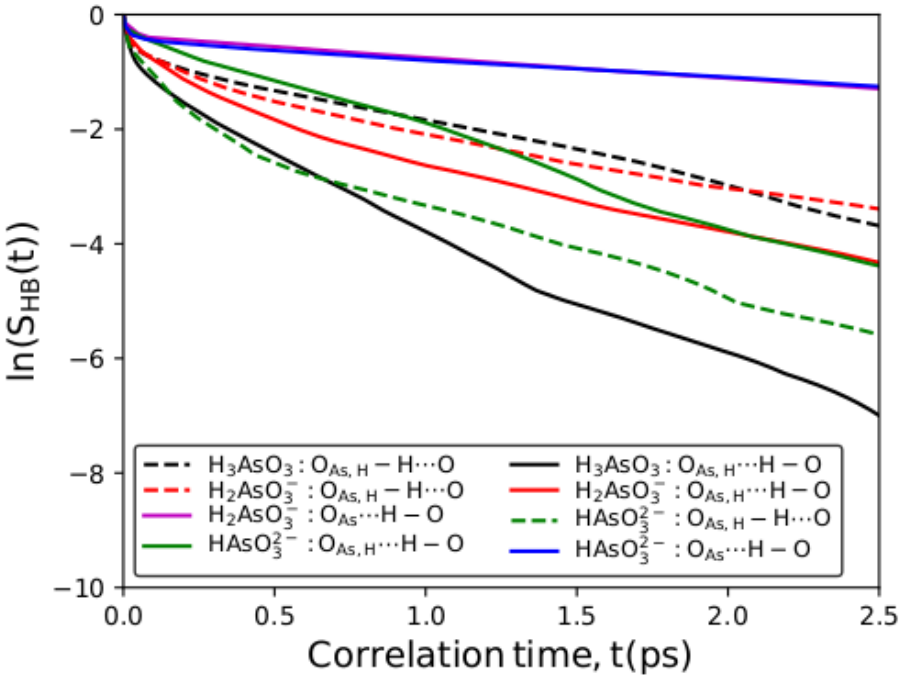

Figure 6.8: Comparison of $S_{HB}(t)$ for all the types of H-bonds formed by the solute species with bulk waters. Donated ones are shown as solid lines, while the accepted ones are shown as dotted lines of respective colors (black: H_3AsO_3, red: $H_2AsO_3^-$ and blue: $HAsO_3^{2-}$). The characteristic decay constants, τ_s, for all the cases, can be obtained in table 6.2.

Table 6.2: Characteristic decay constants of τ_s of different types of H-bonds present in the systems dissolving H_3AsO_3, $H_2AsO_3^-$ and $HAsO_3^{2-}$ in comparison to pure H_2O, obtained from exponential fitting of $S_{HB}(t)$ in Fig.6.8.

Species	Types	τ_s (ps)
H_3AsO_3	$O_{As,H} - H \cdots O$	0.88
	$O_{As,H} \cdots H - O$	0.37
$H_2AsO_3^-$	$O_{As,H} - H \cdots O$	0.91
	$O_{As,H} \cdots H - O$	0.75
	$O_{As} \cdots H - O$	2.53
$HAsO_3^{2-}$	$O_{As,H} - H \cdots O$	0.68
	$O_{As,H} \cdots H - O$	0.60
	$O_{As} \cdots H - O$	3.64

be treated as an *exponential* decay, and thus can be fitted with an exponential function [20]. We have adopted the naive way of fitting with single exponential functions, for the sake of simplicity and comparison to previous works. However, these results might

vary somewhat quantitatively depending on the methods of choice, which is discussed in the article by Antipova and Petrenko [20]. The characteristic decay constants, τ_s, providing an estimate of the lifetime of the H-bond concerned, obtained as mentioned above are included in table 6.2. It is worthy to note that these values are liable to hold large statistical errors, and thus serves just as "indicators" of the qualitative nature for comparative interpretations. From Fig. 6.8 and Table. 6.2, it is observed that the lifetimes of H-bonds accepted by O_{As} are very strong in nature for both the cases of $H_2AsO_3^-$ and $HAsO_3^{2-}$. The lifetimes of the H-bonds donated by H_3AsO_3 are comparable to those for bulk water H-bonds, while those accepted by it are weaker. The lifetimes of the accepted H-bonds are found to increase exceptionally for the deprotonated states ($H_2AsO_3^-$ and $HAsO_3^{2-}$) in comparison to those of H_3AsO_3. The lifetimes of the H-bonds formed among the solvent waters dissolving various As – III species are found to be very similar to that of pure waters and have not been shown in the plots.

6.3.5 Vibrational Density of States

Table 6.3: Gas phase normal mode frequencies of H_3AsO_3 along with a qualitative description of vibrational modes, recognized from visualization.

Serial No.	Frequency (cm^{-1})	Description of the mode
1 - 6	118, 219, 278, 305, 326, 375	Various bending modes
7	617	Antisymmetric bending of $As-O_{As,H}$ bonds involving all three
8	652	Antisymmetric bending involving two $As-O_{As,H}$ bonds
9	678	Symmetric bending of $As-O_{As,H}$ bonds involving all three
10	886	Out of phase $As-O_{As,H}-H$ bending involving two of them
11	906	In phase $As-O_{As,H}-H$ bending involving two of them
12	937	$As-O_{As,H}-H$ bending involving all three of them, two are in phase
13	3649	Stretching of $O_{As,H}-H$ bond involving only one of them
14	3660	Symmetric stretching of $O_{As,H}-H$ bonds
15	3703	Antisymmetric stretching of $O_{As,H}-H$ bonds

Fig. 6.9 shows the vibrational density of states (VDOS), calculated by taking the Fourier transformation of the velocity autocorrelation function (VACF) of the individual atomic species. The spectra for bulk H_2O dissolving the solutes are qualitatively very similar to that of bulk waters. We have also shown as down-triangles, the normal modes of atomic

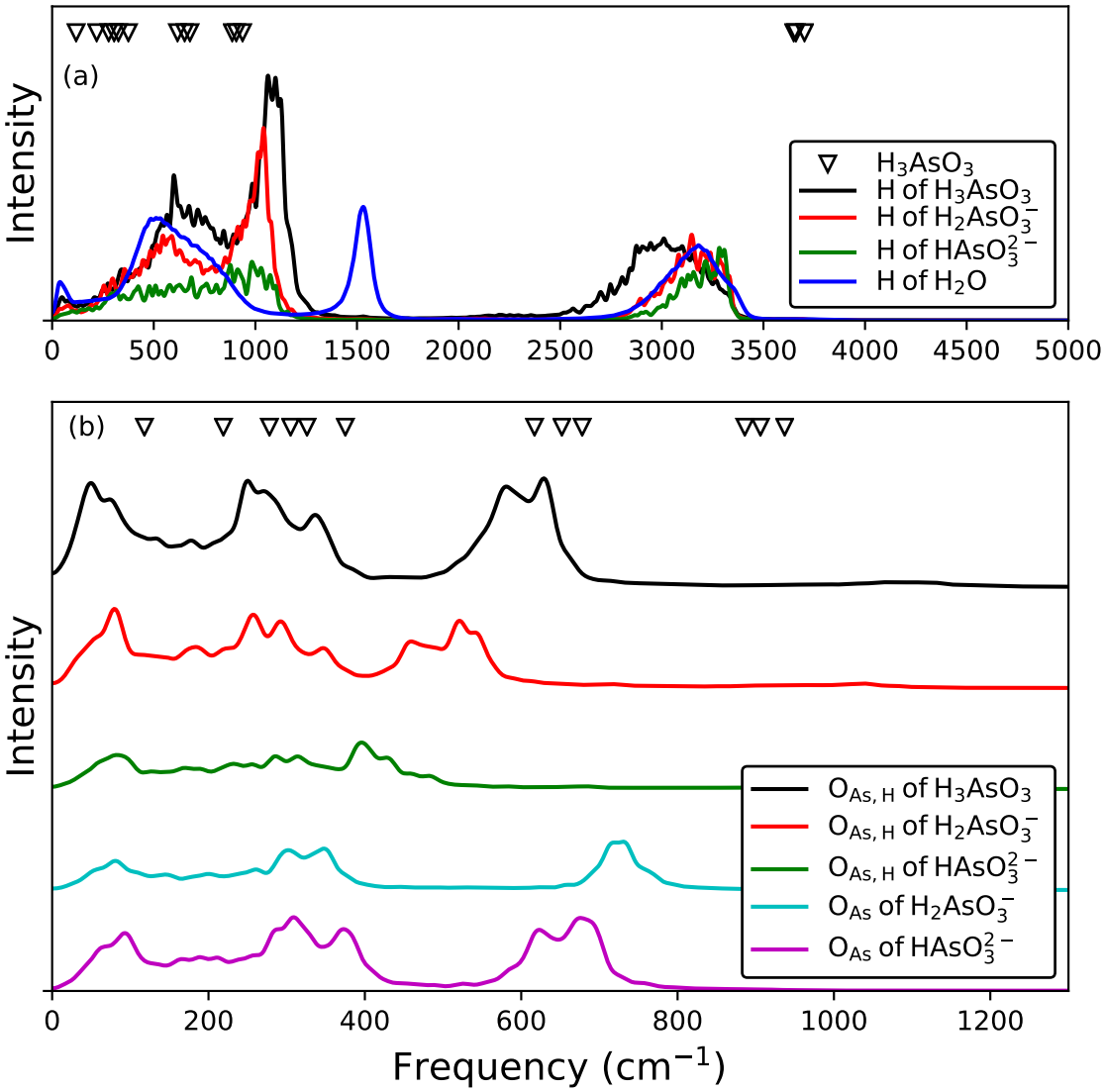

Figure 6.9: Vibrational density of states (VDOS) of (a) H of As−III species and bulk waters, and (b) $O_{As,H}$ and O_{As} atoms of the solutes. The gas phase vibrational modes of H_3AsO_3 molecule are shown as triangles, printed down, with the description of the modes included in table 6.3.

vibrations of harmonic atomic motions in the gas phase for H_3AsO_3. The qualitative descriptions of all the modes are presented in table 6.3.

The $O_{As,H}$−H and O−H stretching modes are red-shifted to a range of ~ 2500 − 3500 cm^{-1}, i.e., by an amount of ~ 400 cm^{-1} in comparison to the gas phases. It should be noted these red-shifts are far less than those of As−V species discussed in chapter 5. In the previous cases, each intra-molecular H atom of the solute molecules has been observed to donate strong H-bonds to waters, which is not the case for As−III species

here. The experimentally reported pK_a values suggest that As – III species are weak acids, and probably why the red-shifts are significantly lower. 6.9 (a). Moreover, it is observed that the amounts of red-shifts in these modes follow the order seen in the H-bond correlation plots in Fig. 6.8 and table 6.2.

In Fig. 6.9(b), the vibrational density of states for O_{As} and $O_{As,H}$ have been shown for all the cases. The gas phase values in the range of $0 - 1200$ for H_3AsO_3 are also included. As expected, a sequential red-shift in the bond stretching modes is observed for double bonded O_{As} atoms, with those of $HAsO_3^{2-}$ exhibiting higher red-shifts as compared to the case of $H_2AsO_3^-$. Similar trend is perceived in cases of the $O_{As,H}$ atoms as well. These observations are consistent with the H-bond correlation functions shown in Fig. 6.8. The obtained spectra have been found to be in qualitative agreement with experimental results available [19].

6.4 Conclusion

In conclusion, we have carried out a detailed *ab initio* molecular dynamics investigation of waterborne As – III species, viz. H_3AsO_3, $H_2AsO_3^{2-}$ and $HAsO_3^{2-}$, and analyzed the nature of hydration and H-bonding.

Under normal conditions, both H_3AsO_3 and $H_2AsO_3^-$ are found to be stable during simulation runs extending over 50 ps, while $HAsO_3^{2-}$ and AsO_3^{3-} readily protonate forming $H_2AsO_3^-$ and $HAsO_3^{2-}$ respectively. This is because of the pK_a of the species. AsO_3^{3-} was found to capture one of the solvent hydrogens, readily making a conformational change from planar to tripodal, forming $HAsO_3^{2-}$. An analysis of the hydration structure reveals that $HAsO_3^{2-}$ accumulates a stronger or compact hydration shell around it, as compared to H_3AsO_3 and $H_2AsO_3^-$. The different types of H-bonds formed by the solutes forms H-bonds that dependent on the structure of the solutes and the net charge of the species. The lifetimes of the H-bonds accepted by the bare oxygens of the species are generally very strong that too increases with the effective charge of the species; while the other H-bonds are somewhat weaker in comparison to those of bulk waters. Overall, the presence of different As – III species is found to only slightly alter the dynamics of solvents as compared to pure water. Since the As – III species are very weak acids, they do not show tendency of being deprotonated, which makes these species to exhibit much lesser red-shifts in solute O – H stretching modes, in comparison to As – V species discussed in the previous chapter.

BIBLIOGRAPHY

[1] Johan Mähler, Ingmar Persson, and Roger B Herbert. Hydration of arsenic oxyacid species. *Dalton Trans.*, 42(5):1364–1377, 2013.

[2] Badal Kumar Mandal and Kazuo T Suzuki. Arsenic round the world: a review. *Talanta*, 58(1):201–235, 2002.

[3] Masato Tanaka, Yoshio Takahashi, Noriko Yamaguchi, Kyoung-Woong Kim, Guodong Zheng, and Mika Sakamitsu. The difference of diffusion coefficients in water for arsenic compounds at various ph and its dominant factors implied by molecular simulations. *Geochim. Cosmochim. Acta*, 105:360–371, 2013.

[4] Satinder Ahuja. *Arsenic contamination of groundwater: mechanism, analysis, and remediation*. John Wiley & Sons, 2008.

[5] Yuka Yokoyama, Kazuya Tanaka, and Yoshio Takahashi. Differences in the immobilization of arsenite and arsenate by calcite. *Geochim. Cosmochim. Acta*, 91:202–219, 2012.

[6] Junlian Qiao, Zheng Jiang, Bo Sun, Yuankui Sun, Qi Wang, and Xiaohong Guan. Arsenate and arsenite removal by fecl 3: effects of ph, as/fe ratio, initial as concentration and co-existing solutes. *Sep. Purif. Technol.*, 92:106–114, 2012.

[7] Axel D Becke. Density-functional exchange-energy approximation with correct asymptotic behavior. *Phys. Rev. A*, 38(6):3098, 1988.

[8] Chengteh Lee, Weitao Yang, and Robert G Parr. Development of the colle-salvetti correlation-energy formula into a functional of the electron density. *Phys. Rev. B*, 37(2):785, 1988.

[9] Walter Kohn and Lu Jeu Sham. Self-consistent equations including exchange and correlation effects. *Phys. Rev.*, 140(4A):A1133, 1965.

[10] Pierre Hohenberg and Walter Kohn. Inhomogeneous electron gas. *Phys. Rev.*, 136(3B):B864, 1964.

[11] Shūichi Nosé. A molecular dynamics method for simulations in the canonical ensemble. *Mol. Phys.*, 52(2):255–268, 1984.

[12] Shuichi Nosé. A unified formulation of the constant temperature molecular dynamics methods. *J. Chem. Phys.*, 81(1):511–519, 1984.

[13] William G Hoover. Canonical dynamics: equilibrium phase-space distributions. *Phys. Rev. A*, 31(3):1695, 1985.

[14] Dominik Marx and Jürg Hutter. *Ab initio molecular dynamics: basic theory and advanced methods*. Cambridge University Press, 2009.

[15] I-Feng W Kuo and Christopher J Mundy. An ab initio molecular dynamics study of the aqueous liquid-vapor interface. *Science*, 303(5658):658–660, 2004.

[16] Glenn J Martyna and Mark E Tuckerman. A reciprocal space based method for treating long range interactions in ab initio and force-field-based calculations in clusters. *J. Chem. Phys.*, 110(6):2810–2821, 1999.

[17] M E Tuckerman. Ab initio molecular dynamics: basic concepts, current trends and novel applications. *J. Phys. Condens. Matter.*, 14(50):R1297–R1355, 2002.

[18] CPMD. General program to perform ab initio molecular dynamics simulations. *CPMD developers group under the terms of the GNU General Public License, http://www.cpmd.org*.

[19] JA Tossell. Theoretical studies on arsenic oxide and hydroxide species in minerals and in aqueous solution. *Geochim. Cosmochim. Acta*, 61(8):1613–1623, 1997.

[20] ML Antipova and VE Petrenko. Hydrogen bond lifetime for water in classic and quantum molecular dynamics. *Russ. J. Phys. Chem. A*, 87(7):1170–1174, 2013.

CHAPTER 7

CONCLUSIONS

We have carried out a comprehensive *ab initio* molecular dynamics studies on various selenium and arsenic species in aqueous environments. These constitute a set of fundamental virtual experiments on various structural, dynamical and spectroscopic aspects of these hydrated species which are important for both ecological and biological processes relevant to humanity.

Chapter 3 of the thesis discussed the waterborne selenium species with valence states of six (Se–VI). The parent form of it is called selenic acid (H_2SeO_4), which is a very strong acid and readily deprotonates forming $HSeO_4^-$ that establishes a dynamic equilibrium with SeO_4^{2-} in the aqueous environment of 60 H_2O molecules. Under normal pH conditions, SeO_4^{2-} is found to be stable, while $HSeO_4^-$ deprotonates to SeO_4^{2-} in a short span during the simulations. The hydration shell of the SeO_4^{2-} has been found to be more robust and well-structured than that of $HSeO_4^-$. SeO_4^{2-} also forms more H-bonds than $HSeO_4^-$ on an average. Although, the accepted H-bonds of $HSeO_4^-$ are weaker than those of SeO_4^{2-}, the hydrogen of $HSeO_4^-$ is found to form a stronger H-bond to a neighboring water molecule. This leads to a higher red-shift of the stretching mode of the hydrogen spectra in comparison to gas normal modes. This behavior is also perceived for the cases of the oxygen spectra of the solutes.

Chapter 4 of the thesis discussed the waterborne selenium species with valence states of four (Se–IV). The parent form of it is called selenous acid (H_2SeO_3), which is an acid of somewhat weaker strength compared to H_2SeO_4. During the simulations in aqueous

environment, H_2SeO_3 establishes a dynamic equilibrium with $HSeO_3^-$, consistent with the experimental pK_a values. Under normal pH conditions, $HSeO_3^-$ is found to be stable. However, SeO_3^{2-} is found to be stable only in basic environment, which is achieved by introducing a hydroxyl ion (OH^-) in the environment. The strength of hydration shell around the solutes is found to increase in series from H_2SeO_3 to SeO_3^{2-}. H_2SeO_3 is found to donate two strong H-bonds to two of the water molecules in its hydration shell because of its tendency to get deprotonated to $HSeO_3^-$. However, the other H-bonds that it forms are weaker leading to an overall diffused hydration shell. This, in turn, is found to influence the overall structural and dynamical aspects of the bulk water. For instance, the solvent in this case is more over-structured, forming more H-bonds among themselves which are also of considerably higher lifetimes. The bulk water in presence of H_2SeO_3 is also found to be structurally and orientationally relaxed.

In SeO_4^{2-}, each of the O_{Se} sites accepts about 2.3 H-bonds amounting to a total of 9.2 per species. This is slightly larger than the total H-bonds formed by SeO_3^{2-} in basic solution. The lifetime of H-bonds formed by SeO_3^{2-} is somewhat longer (1.52 ps) than that of SeO_4^{2-} (1.10 ps). On the other hand, $HSeO_4^-$ forms a total of 6.82 H-bonds (including the one it nearly always donates). This is quite similar to $HSeO_3^-$. However, the donated H-bond of $HSeO_4^-$ is found to be very long-lived, reflecting its tendency for proton transfer with surrounding water forming SeO_4^{2-}. This behavior is also seen for the hydrogens of H_2SeO_3, but not for $HSeO_3^-$.

Chapter 5 of the thesis discussed the waterborne arsenic species with valence states of five (As–V). It is found that the compactness of the hydration shells as well as the total number of H-bonds formed with water increases across the series, from H_3AsO_4 to AsO_4^{3-}, with the net effective charge of the solute. This results in lengthening of the As–O bond and strengthening of the H-bonds, and also causes a systematic red-shifts in the vibrational density of states. The H-bonds donated by the As–V species are found to be considerably long lived compared to those accepted by the species, also those of pure water, and follow an overall systematic behavior across the series. Moreover, the nature of the solvent-water itself is found to be sensitive to the solute, impacting the H-bond lifetimes as well as structural and orientational relaxation times of the solvent-water molecules. It is observed that the dipole moments of the solute could responsible for slower orientational relaxation of the surrounding water molecules, which is seen for the case of $H_2AsO_4^-$.

Chapter 6 of the thesis discussed the waterborne arsenic species with valence states

of 3 (As−III). Under normal conditions, both H_3AsO_3 and $H_2AsO_3^-$ are found to be stable during the simulations extending over 50 ps, while $HAsO_3^{2-}$ and AsO_3^{3-} readily protonate forming $H_2AsO_3^-$ and $HAsO_3^{2-}$ respectively, because of the high pK_a of the species. AsO_3^{3-} was found to capture one H of its solvent water, readily making a conformational transformation from planar to tripodal, forming $HAsO_3^{2-}$. An analysis of the hydration structure reveals that $HAsO_3^{2-}$ forms a stronger and compact hydration shell around it, as compared to H_3AsO_3 and $H_2AsO_3^-$. The different types of sites of the solutes forms H-bonds that dependent on the structure of the solutes as well as their oxidation states. The lifetimes of the H-bonds accepted by the bare oxygens of the species are generally very strong. This behavior is more pronounced with the deprotonation of the species, while the other H-bonds are weaker even comparison to those of bulk water. Overall, the presence of different As−III species is found to only slightly alter the dynamics of bulk waters as compared to pure waters. Since the As−III species are very weak acids, they do not show tendency of being deprotonated, which makes these species to exhibit much lesser red-shifts in solute O−H stretching modes, in comparison to As−V ones.

In AsO_4^{3-}, each of the O_{As} sites accepts about 2.8 H-bonds amounting to a total of 11.2 per species. The total number of H-bonds formed by $HAsO_3^-$ is 8.5 per species and 2.8 per oxygen site (with O_{As} and $O_{As,H}$ taken together), although each O_{As} site accepts 3.0 H-bonds, higher than that of AsO_4^{3-}. The total number of H-bonds formed by H_3AsO_3 is 5.9 per species (1.9 per oxygen site) which is lower than H_3AsO_4 and $H_2AsO_4^-$. The H-bond accepted from O_{As} sites of $H_2AsO_3^-$ and $HAsO_3^{2-}$ are stronger than those of As−V species; however, those donated by $O_{As,H}$ sites are much weaker.

We believe that these studies would be helpful in better understanding the global cycle of selenium and arsenic in the ecosystem as well as, in their identification and characterization in aqueous and various confined environments. Being of great importance in the solution chemistry and biology, these studies would help chemists and biologists for developing strategies for water remediation and drug design. Development of classical force field models, based on these results would be of special interest. This would facilitate long MD simulations required for the study of mobility and remediation of potable water. For instance, adsorption of selenium and arsenic on clays, activated alumina grains or oxide surfaces, such as manganese, aluminum, and iron, etc. are of practical interest. We hope that the current studies would prompt more theoretical and experimental studies on selenium and arsenic in natural environments.

APPENDIX A

VERLET AND VELOCITY VERLET ALGORITHMS

Verlet and velocity Verlet algorithms are the most popular and widely used numerical integrator schemes in the field of molecular simulations. These can be derived employing simple Taylor expansions. First, consider the Taylor expansion of position vector in time,

$$\begin{aligned}\vec{r}(t+\delta t) =& \vec{r}(t) + \frac{d\vec{r}}{dt}\delta t + \frac{d^2\vec{r}}{dt^2}\frac{\delta t^2}{2} + \frac{d^3\vec{r}}{dt^3}\frac{\delta t^3}{6} + \mathcal{O}(\delta t^4) \\ =& \vec{r}(t) + \vec{v}(t)\delta t + \frac{\vec{F}(t)}{m}\frac{\delta t^2}{2} + \frac{d^3\vec{r}}{dt^3}\frac{\delta t^3}{6} + \mathcal{O}(\delta t^4). \end{aligned} \tag{A.1}$$

Similarly,

$$\vec{r}(t-\delta t) = \vec{r}(t) - \vec{v}(t)\delta t + \frac{\vec{F}(t)}{m}\frac{\delta t^2}{2} - \frac{d^3\vec{r}}{dt^3}\frac{\delta t^3}{6} + \mathcal{O}(\delta t^4). \tag{A.2}$$

Adding Eq. (A.1) and (A.2), we get what forms the basis of the Verlet algorithm,

$$\vec{r}(t+\delta t) = 2\vec{r}(t) - \vec{r}(t-\delta t) + \frac{\vec{F}(t)}{m}\delta t^2 + \mathcal{O}(\delta t^4). \tag{A.3}$$

Thus, the positions of the current and previous steps are needed in order to compute the position at the next simulation step. Forces at time t can be computed from $\vec{F} = -\vec{\nabla}V(\vec{r})$. This algorithm does not explicitly involve velocities, however, can be computed employing the following relation (can be derived by subtracting Eq. (A.2) from Eq. (A.1)):

$$\vec{v}(t) = \frac{\vec{r}(t+\delta t) - \vec{r}(t-\delta t)}{2\delta t} + \mathcal{O}(\delta t^3) \tag{A.4}$$

The main disadvantage of the Verlet algorithm is that it requires to store two sets of positions at current and previous steps in memory in order to compute the positions at the next time step. Moreover, it does not involve velocities explicitly in computations. An alternative scheme that is used is called velocity Verlet algorithm, which is nothing but a reformulation of the Verlet algorithm by manipulating the expansions that uses the velocity directly. In order to derive it, we need to compute the Taylor expansions about $\vec{r}(t+\delta t)$, $\vec{v}(t+\delta t)$, and $\dot{\vec{v}}(t+\delta t)$.

$$\vec{r}(t+\delta t) = \vec{r}(t) + \vec{v}(t)\delta t + \frac{\vec{F}(t)}{m}\frac{\delta t^2}{2} + \mathcal{O}(\delta t^3) \tag{A.5}$$

$$\vec{v}(t+\delta t) = \vec{v}(t) + \frac{\vec{F}}{m}\delta t + \ddot{\vec{v}}(t)\frac{\delta t^2}{2} + \mathcal{O}(\delta t^3) \tag{A.6}$$

$$\frac{\vec{F}(t+\delta t)}{m} = \frac{\vec{F}(t)}{m} + \ddot{\vec{v}}(t)\delta t + \mathcal{O}(\delta t^2). \tag{A.7}$$

Substituting $\ddot{\vec{v}}(t)$ from Eq. (A.7) into Eq. (A.6), we get, along with Eq. (A.5) the working formulae for velocity Verlet algorithm:

$$\vec{r}(t+\delta t) = \vec{r}(t) + \vec{v}(t)\delta t + \frac{1}{2m}\vec{F}(t)\delta t^2 \tag{A.8}$$

$$\vec{v}(t+\delta t) = \vec{v}(t) + \frac{1}{2m}\left(\vec{F}(t) + \vec{F}(t+\delta t)\right) \tag{A.9}$$

This algorithm has the advantage of using coordinates and velocities at the same instant t. The flowchart of this algorithm is presented in Fig. A.1.

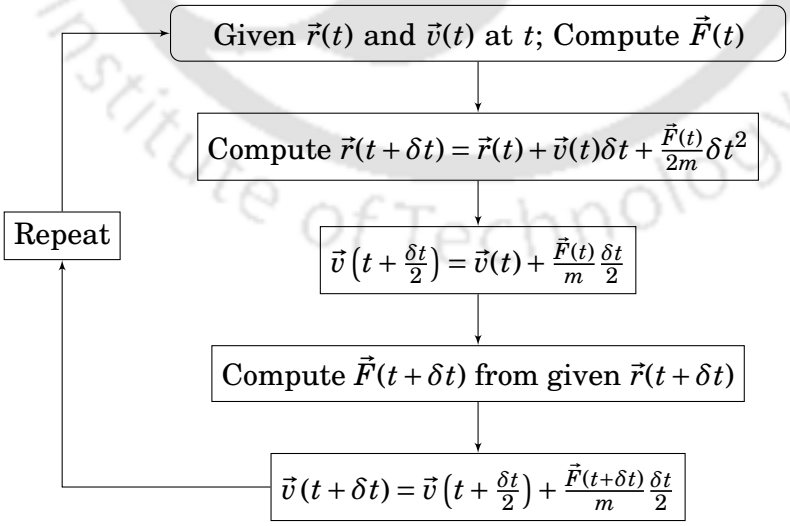

Figure A.1: A basic flowchart of velocity Verlet scheme.

APPENDIX B

PERIODIC BOUNDARY CONDITIONS

Typical size of the simulation cells employed for molecular dynamics studies is of the order of nano-meters. The surface atoms of such nano-systems are very different from that of the bulk (experimental) conditions. In other words, such a simulation cell is far from being reality. One way to mimic the bulk conditions in such nano-systems is through the concept of *periodic boundary conditions* (PBC) that realize an infinite number of copies of the simulation box, as shown in Fig. B.1 For orthorhombic cells ($\alpha = \beta = \gamma = 90°$),

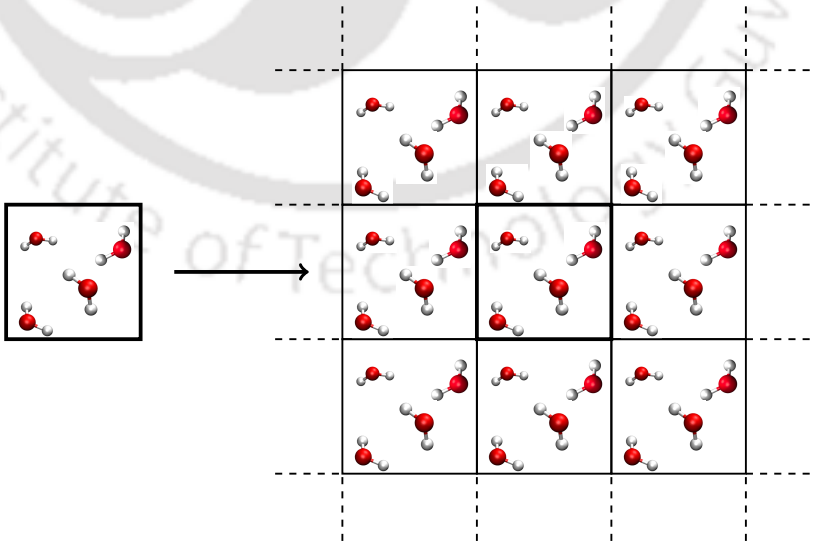

Figure B.1: The concept of periodic boundary condition.

PBC can be implemented with the three lines of codes:

$$x = x - a * \text{ANINT}\left(\frac{dx}{a}\right), \tag{B.1a}$$

$$y = y - b * \text{ANINT}\left(\frac{dy}{b}\right), \tag{B.1b}$$

$$z = z - c * \text{ANINT}\left(\frac{dz}{c}\right), \tag{B.1c}$$

where $[a,b,c]$ is the dimension of the simulation box, and ANINT function rounds its argument to the nearest whole number.

While in most of cases the simulation cell is taken as orthorhombic, in certain cases, especially for the cases of non-orthorhombic crystals, one might have to consider non-orthorhombic simulation cells. In these cases, one has to convert the non-orthorhombic cell to scaled coordinates (a cell of dimensions $[1,1,1]$ with unit volume) and apply the periodic boundary conditions for orthorhombic cells as given in Eqs. B.1a-1c. For this, one has to construct what is known as the H-matrix and it's inverse. The H-matrix elements are given by,

$$\text{H11} = a, \tag{B.2a}$$

$$\text{H21} = 0, \tag{B.2b}$$

$$\text{H31} = 0, \tag{B.2c}$$

$$\text{H12} = b\cos\gamma \tag{B.2d}$$

$$\text{H22} = b\sin\gamma, \tag{B.2e}$$

$$\text{H23} = 0, \tag{B.2f}$$

$$\text{H13} = c\cos\beta, \tag{B.2g}$$

$$\text{H23} = \frac{c(\cos\alpha - \cos\beta\cos\gamma)}{\sin\gamma}, \tag{B.2h}$$

$$\text{H33} = \frac{c\sqrt{1 + 2\cos\alpha\cos\beta\cos\gamma - \cos^2\alpha - \cos^2\beta - cos^2\gamma}}{\sin\gamma}. \tag{B.2i}$$

Under PBC, the linear momentum of the system is conserved, but angular momentum is not conserved.

APPENDIX C

THERMOSTATS IN MOLECULAR DYNAMICS

In order to carry out simulations in *NVT* ensembles, we have to select a thermostat. There are three popular thermostats, discussed below.

Anderson Thermostat: This is based on stochastic collisions between randomly selected particles with the fictitious particles (heat baths) that result in a new velocity distribution with the desired temperature. The steps that are followed are,

1. Integrate the equations of motions for time Δt.
2. Number of atoms that undergo collision during Δt is $\nu \Delta t$, selected randomly. Here ν is the coupling constant.
3. Assign new velocities to the selected atoms using Maxwell-Boltzmann distribution at the desired temperature T_0.

Although this thermostat leads to the desired temperature and canonical distribution, random collisions affect the atomic dynamics, e.g. diffusion coefficient and other dynamic properties.

Berensden Thermostat: In this approach the equation of motion is modified as follows,

$$\dot{\vec{P}}_i(t) = \vec{F}_i - \gamma(t)\vec{P}_i, \tag{C.1}$$

where,

$$\gamma(t) \propto \frac{T(t) - T_0}{T(t)} \tag{C.2}$$

controls the direction of heat flow. This is a direct feedback approach in the sense that if temperature is more energy is taken away, and added if less than the desired temperature T_0. This thermostat is useful in thermalizing the system to desired temperature during equilibration. However, it does not lead to correct canonical distribution and energy fluctuations.

Nosé-Hoover Thermostat: The basic difference of Nosé-Hoover thermostat with the Berensden thermostat is the fact that it is an integral feedback approach rather than direct feedback in Berensden thermostat,

$$\dot{\gamma}(t) \propto \frac{T(t) - T_0}{T_0}. \tag{C.3}$$

This simple modification leads to proper correct canonical distribution and energy fluctuations. However, if not selected with proper controlling parameters, being an integral feedback, it might lead to high oscillations around the mean temperature and non-canonical distributions. Nosé-Hoover thermostat is the most widely employed thermostats for molecular dynamics simulations, especially employing on-the-fly methods.

List of Publications

1. Sangkha Borah and P. Padma Kumar, "Ab initio molecular dynamics investigation of structural, dynamic and spectroscopic aspects of Se (VI) species in the aqueous environment," *Phys. Chem. Chem. Phys.*, **18**, 14561-14568, 2016.

2. Sangkha Borah and P. Padma Kumar, "Ab initio molecular dynamics study of Se (IV) species in aqueous environment,"*Phys. Chem. Chem. Phys.*, **18**, 26755-26763, 2016.

3. Sangkha Borah and P. Padma Kumar, "First principle molecular dynamics investigation of waterborne As – V species." *J. Phys. Chem. B* **122**(12), 2018, 3153-3162.

4. Sangkha Borah and P. Padma Kumar, "Dynamics of As – III species in water." (*manuscript under preparation*)

Conferences/Schools/Workshops attended

- DST-SERC School on "Density Functional Theory and Beyond: Computational Material Science and Material Design", Nov. 24 - Dec. 13, 2014. The Maharaja Sayajirao University of Boroda, Vadodara - 390002, India. [Participant & Oral (CPMD Basics)]

- XXVII IUPAP Conference on Computational Physics, Dec. 2-5, 2015, IIT Guwahati. [Poster presentation]

- National Workshop on Atomistic Simulation Technique, Dec. 21-24, 2015, IIT Guwahati. [Instructor: hands-on-session]

- 5^{th} Symposium on Advanced Biological Inorganic Chemistry (SABIC-2017), organized by IACS, Kolkata and TIFR, Mumbai held in Kolkata, during Jan. 7-11, 2017. [Poster presentation]

- Atomistic Computer Simulation Techniques (workshop), Oct. 31- Nov. 1, Assam University, Silchar. [Instructor: hands-on-session]

- Recent Advances in Modelling Rare Events, Dec. 7-10, 2017, Agra, India, Jointly organized by University of Maryland, USA, Columbia University, USA and IIT Kanpur, India. [Poster presentation]